

The PLATO Mission

Heike Rauer^{1,2}, Conny Aerts³, Juan Cabrera¹, Magali Deleuil⁴,
 Anders Erikson¹, Laurent Gizon⁵, Mariejo Goupil⁶, Ana Heras⁷,
 Jose Lorenzo-Alvarez⁷, Filippo Marliani⁷, César Martin-Garcia^{1,8},
 J. Miguel Mas-Hesse⁹, Laurence O'Rourke⁸, Hugh Osborn¹⁰,
 Isabella Pagano¹¹, Giampaolo Piotto¹², Don Pollacco¹³,
 Roberto Ragazzoni¹⁴, Gavin Ramsay¹⁵, Stéphane Udry¹⁶,
 Thierry Appourchaux¹⁷, Willy Benz¹⁰, Alexis Brandeker¹⁸,
 Manuel Güdel¹⁹, Eduardo Janot-Pacheco²⁰, Petr Kabath²¹,
 Hans Kjeldsen²², Michiel Min²³, Nuno Santos^{24,25}, Alan Smith²⁶,
 Juan-Carlos Suarez²⁷, Stephanie C. Werner²⁸, Alessio Aboudan²⁹,
 Manuel Abreu³⁰, Lorena Acuña³¹, Moritz Adams³²,
 Vardan Adibekyan²⁴, Laura Affer³³, François Agneray⁴,
 Craig Agnor³⁴, Victor Aguirre Børsen-Koch³⁵, Saad Ahmed³⁶,
 Suzanne Aigrain³⁷, Ashraf Al-Bahlawan²⁶,
 M^a de los Angeles Alcacera Gil³⁸, Eleonora Alei^{14,152},
 Silvia Alencar⁴⁰, Richard Alexander⁴¹, Julia Alfonso-Garzón⁹,
 Yann Alibert¹⁰, Carlos Allende Prieto^{42,43}, Leonardo Almeida⁴⁴,
 Roi Alonso Sobrino^{42,43}, Giuseppe Altavilla⁴⁵, Christian Althaus¹,
 Luis Alonso Alvarez Trujillo³⁸, Anish Amarsi⁴⁶,
 Matthias Ammler-von Eiff⁵, Eduardo Amôres⁴⁷,
 Laerte Andrade⁴⁸, Alexandros Antoniadis-Karnavas²⁴,
 Carlos António⁴⁹, Beatriz Aparicio del Moral⁵⁰,
 Matteo Appolloni⁷, Claudio Arena¹¹, David Armstrong¹³,
 Jose Aroca Aliaga⁷, Martin Asplund⁵¹, Jeroen Audenaert^{3,52},
 Natalia Auricchio⁵³, Pedro Avelino^{24,25}, Ann Baeke⁵⁴,
 Kevin Baillié⁵⁵, Ana Balado³⁸, Andrea Balestra¹⁴,
 Warrick Ball⁵⁶, Herve Ballans¹⁷, Jerome Ballot⁵⁷,
 Caroline Barban⁶, Gaële Barbary⁶, Mauro Barbieri⁵⁸,
 Sebastià Barceló Forteza⁹, Adrian Barker⁵⁹, Paul Barklem⁴⁶,
 Sydney Barnes⁶⁰, David Barrado Navascues⁹, Oscar Barragan³⁷,
 Clément Baruteau⁵⁷, Sarbani Basu⁶¹, Frederic Baudin¹⁷,

Philipp Baumeister¹, Daniel Bayliss¹³, Michael Bazot⁶²,
 Paul G. Beck^{63,42,43}, Tim Bedding⁶⁴, Kevin Belkacem⁶,
 Earl Bellinger⁶⁵, Serena Benatti³³, Othman Benomar^{66,67},
 Diane Bérard⁵⁵, Maria Bergemann³¹, Maria Bergomi⁶⁸,
 Pierre Bernardo⁴, Katia Biazzo¹¹, Andrea Bignamini⁶⁹,
 Lionel Bigot⁷⁰, Nicolas Billot¹⁶, Martin Binet¹³, David Biondi⁷¹,
 Federico Biondi⁶⁸, Aaron C. Birch⁵, Bertram Bitsch³¹,
 Paz Victoria Bluhm Ceballos², Attila Bódi^{72,73},
 Zsófia Bognár^{74,73}, Isabelle Boisse⁴, Emeline Bolmont⁷⁵,
 Alfio Bonanno¹¹, Mariangela Bonavita⁷⁶, Andrea Bonfanti⁷⁷,
 Xavier Bonfils⁷⁸, Rosaria Bonito³³, Aldo Stefano Bonomo⁷⁹,
 Anko Börner⁸⁰, Sudeshna Boro Saikia¹⁹,
 Elisa Borreguero Martín³⁸, Francesco Borsa⁸¹, Luca Borsato¹²,
 Diego Bossini²⁴, Francois Bouchy⁷⁵, Gwenaél Boué⁵⁵,
 Rodrigo Bouffleur⁸², Patrick Boumier¹⁷, Vincent Bourrier⁷⁵,
 Dominic M. Bowman^{83,3}, Enrico Bozzo¹⁶, Louisa Bradley²⁶,
 John Bray⁸⁴, Alessandro Bressan⁸⁵, Sylvain Breton¹¹,
 Daniele Brienza⁷¹, Ana Brito^{86,223}, Matteo Brogi⁸⁷,
 Beverly Brown⁷, David Brown¹³, Allan Sacha Brun⁸⁸,
 Giovanni Bruno¹¹, Michael Bruns⁵, Lars A. Buchhave⁸⁹,
 Lisa Bugnet⁹⁰, Gaël Buldgen⁷⁵, Patrick Burgess³⁶,
 Andrea Busatta¹¹, Giorgia Busso³⁶, Derek Buzasi⁹¹,
 José A. Caballero⁹, Alexandre Cabral³⁰, Flavia Calderone¹¹,
 Robert Cameron⁵, Andrew Cameron⁹², Tiago Campante²⁴,
 Bruno Leonardo Canto Martins⁴⁴, Christophe Cara⁸⁸,
 Ludmila Carone⁷⁷, Josep Manel Carrasco^{93,39,94},
 Luca Casagrande⁵¹, Sarah L. Casewell⁴¹, Santi Cassisi^{95,96},
 Marco Castellani⁶⁸, Matthieu Castro⁴⁴, Claude Catala⁶,
 Irene Catalán Fernández³⁸, Márcio Catelan^{97,98}, Heather Cegla¹³,
 Chiara Cerruti³⁸, Virginie Cessa¹⁰, Merieme Chadid⁷⁰,
 William Chaplin⁵⁶, Stephane Charpinet⁵⁷, Cristina Chiappini⁶⁰,
 Simone Chiarucci⁹⁹, Andrea Chiavassa⁷⁰, Simonetta Chinellato⁶⁸,
 Giovanni Chirulli⁷, Jørgen Christensen-Dalsgaard¹⁰⁰,
 Ross Church¹⁰¹, Antonio Claret⁵⁰, Cathie Clarke³⁶,
 Riccardo Claudi¹⁴, Lionel Clermont⁵⁴, Hugo Coelho⁴⁴,
 Joao Coelho³⁰, Fabrizio Cogato^{102,53}, Josep Colomé^{103,94},
 Mathieu Condamin¹⁰⁴, Simon Conseil⁴, Thierry Corbard⁷⁰,
 Alexandre C. M. Correia¹⁰⁵, Enrico Corsaro¹¹,

Rosario Cosentino¹⁰⁶, Jean Costes⁴, Andrea Cottinelli¹⁴,
 Giovanni Covone¹⁰⁷, Orlagh L. Creevey⁷⁰, Aurelien Crida⁷⁰,
 Szilard Csizmadia¹, Margarida Cunha²⁴, Patrick Curry²⁶,
 Jefferson da Costa⁴⁴, Francys da Silva⁴⁴, Shweta Dalal¹⁰⁸,
 Mario Damasso⁷⁹, Cilia Damiani⁵, Francesco Damiani³³,
 Maria Liduina das Chagas¹⁰⁹, Melvyn Davies¹¹⁰, Guy Davies⁵⁶,
 Ben Davies¹¹¹, Gary Davison²⁶, Leandro de Almeida^{44,112},
 Francesca de Angeli³⁶, Susana Cristina Cabral de Barros²⁴,
 Izan de Castro Leão⁴⁴, Daniel Brito de Freitas¹¹³,
 Marcia Cristina de Freitas⁴⁰, Domitilla De Martino¹¹⁴,
 José Renan de Medeiros⁴⁴, Luiz Alberto de Paula²⁰,
 Jelle de Plaa²³, Joris De Ridder³, Morgan Deal¹¹⁵, Leen Decin³,
 Hans Deeg^{42,43}, Scilla Degl'Innocenti¹¹⁶, Sebastien Deheuveld⁵⁷,
 Carlos del Burgo^{117,43}, Fabio Del Sordo¹¹, Elisa Delgado-Mena²⁴,
 Olivier Demangeon²⁴, Tilmann Denk¹, Aliz Derekas¹¹⁸,
 Silvano Desidera¹⁴, Marc Dexet¹⁷, Marcella Di Criscienzo⁶⁸,
 Anna Maria Di Giorgio⁷¹, Maria Pia Di Mauro⁷¹,
 Federico Jose Diaz Rial¹¹⁹, José-Javier Díaz-García⁴²,
 Marco Dima⁶⁸, Giacomo Dinuzzi⁷¹, Odysseas Dionatos¹⁹,
 Elisa Distefano⁶⁸, Jose-Dias do Nascimento Jr.⁴⁴,
 Albert Domingo⁹, Valentina D'Orazi¹⁴, Caroline Dorn¹²⁰,
 Lauren Doyle¹³, Elena Duarte³⁰, Florent Ducellier⁶,
 Luc Dumaye⁸⁸, Xavier Dumusque⁷⁵, Marc-Antoine Dupret⁵⁴,
 Patrick Eggenberger⁷⁵, David Ehrenreich⁷⁵, Philipp Eigmüller¹,
 Johannes Eising⁸⁰, Marcelo Emilio⁴⁸, Kjell Eriksson⁴⁶,
 Marco Ermocida⁷, Riano Isidoro Escate Giribaldi¹²¹,
 Yoshi Eschen¹³, Inês Estrela⁴⁹, Dafydd Wyn Evans³⁶,
 Damian Fabbian¹²², Michele Fabrizio⁴⁵, João Pedro Faria²⁴,
 Maria Farina⁷¹, Jacopo Farinato⁶⁸, Dax Feliz¹²³,
 Sofia Feltzing¹⁰¹, Thomas Fenouillet⁴, Lorenza Ferrari²³,
 Sylvio Ferraz-Mello²⁰, Fabio Fialho¹²⁴, Agnes Fienga⁷⁰,
 Pedro Figueira¹²⁵, Laura Fiori⁸⁰, Ettore Flaccomio³³,
 Mauro Focardi⁹⁹, Steve Foley¹²⁶, Jean Fontignie⁸⁸,
 Dominic Ford³⁶, Karin Fornazier²⁰, Thierry Forveille⁷⁸,
 Luca Fossati⁷⁷, Rodrigo de Marca Franca¹²⁷,
 Lucas Franco da Silva¹²⁴, Antonio Frasca¹¹,
 Malcolm Fridlund¹²⁸, Marco Furlan¹²⁷, Sarah-Maria Gabler⁵,
 Marco Gaido⁷, Andrew Gallagher³¹, Emanuele Galli⁷¹,

Rafael A. García⁸⁸, Antonio García Hernández²⁷,
 Antonio Garcia Munoz⁸⁸, Hugo García-Vázquez⁴²,
 Rafael Garrido Haba⁵⁰, Patrick Gaulme^{129,5}, Nicolas Gauthier⁶,
 Charlotte Gehan⁵, Matthew Gent¹³⁰, Iskra Georgieva¹²⁸,
 Mauro Ghigo⁶⁸, Edoardo Giana⁷, Samuel Gill¹³, Leo Girardi⁶⁸,
 Silvia Giuliatti Winter¹³¹, Giovanni Giusi⁷¹,
 João Gomes da Silva²⁴, Luis Jorge Gómez Zazo³⁸,
 Juan Manuel Gomez-Lopez⁵⁰, Jonay Isai González Hernández^{42,43},
 Kevin Gonzalez Murillo⁵⁵, Nicolas Gorius¹¹,
 Pierre-Vincent Gouel⁶, Duncan Goulty⁷, Valentina Granata^{132,14},
 John Lee Grenfell¹, Denis Griekbach⁸⁰, Emmanuel Grolleau⁶,
 Salomé Grouffal⁴, Sascha Grziwa¹³³, Mario Giuseppe Guarcello³³,
 Loïc Gueguen⁶, Eike Wolf Guenther¹²⁹, Terrasa Guilhem⁵⁴,
 Lucas Guillerot¹⁷, Pierre Guiot¹⁷, Pascal Guterman⁴,
 Antonio Gutiérrez⁴⁹, Fernando Gutiérrez-Canales⁶,
 Janis Hagelberg¹⁶, Jonas Haldemann¹⁰, Cassandra Hall¹³⁴,
 Rasmus Handberg²², Ian Harrison⁷, Diana L. Harrison^{36,135},
 Johann Hasiba⁷⁷, Carole A. Haswell⁷⁶, Petra Hatalova²⁸,
 Artie Hatzes¹²⁹, Raphaelle Haywood¹⁰⁸, Guillaume Hébrard¹³⁶,
 Frank Heckes⁵, Ulrike Heiter⁴⁶, Saskia Hekker⁶², René Heller⁵,
 Christiane Helling⁷⁷, Krzysztof Helminiak¹³⁷, Simon Hemsley²⁶,
 Kevin Heng¹⁰, Aline Hermans⁵⁴, JJ Hermes¹³⁸,
 Nadia Hidalgo Torres⁷, Natalie Hinkel¹³⁹, David Hobbs¹⁰¹,
 Simon Hodgkin³⁶, Karl Hofmann⁷⁷, Saeed Hojjatpanah⁴,
 Günter Houdek²², Daniel Huber¹⁴⁰, Joseph Huesler⁷,
 Alain Hui-Bon-Hoa⁵⁷, Rik Huygen³, Duc-Dat Huynh⁸⁸,
 Nicolas Iro¹⁹, Jonathan Irwin³⁶, Mike Irwin³⁶,
 André Izidoro^{141,131}, Sophie Jacquinod⁶,
 Nicholas Emborg Jannsen³, Markus Janson¹⁸,
 Harald Jeszenszky⁷⁷, Chen Jiang⁵,
 Antonio José Jimenez Mancebo^{42,43}, Paula Jofre¹⁴²,
 Anders Johansen¹⁰¹, Cole Johnston³, Geraint Jones²⁶,
 Thomas Kallinger¹⁹, Szilárd Kálmán^{118,74,143,144},
 Thomas Kanitz⁷, Marie Karjalainen²¹, Raine Karjalainen²¹,
 Christoffer Karoff^{145,22}, Steven Kawaler¹⁴⁶, Daisuke Kawata²⁶,
 Arnoud Keereman⁷, David Keiderling⁵, Tom Kennedy²⁶,
 Matthew Kenworthy¹⁴⁷, Franz Kerschbaum¹⁹, Mark Kidger⁸,
 Flavien Kiefer⁶, Christian Kintziger⁵⁴, Kristina Kislyakova¹⁹,

László Kiss⁷⁴, Peter Klagyivik², Hubert Klahr¹³⁰,
 Jonas Klevas¹⁴⁸, Oleg Kochukhov⁴⁶, Ulrich Köhler¹,
 Ulrich Kolb⁷⁶, Alexander Koncz¹, Judith Korth¹⁴⁹,
 Nadiia Kostogryz⁵, Gábor Kovács⁷⁴, József Kovács¹¹⁸,
 Oleg Kozhura⁷⁶, Natalie Krivova⁵, Arūnas Kučinskas¹⁴⁸,
 Ilyas Kuhlemann⁵, Friedrich Kupka¹⁵⁰, Wouter Laauwen¹⁵¹,
 Alvaro Labiano⁸, Nadege Lagarde¹⁵², Philippe Laget⁷,
 Gunter Laky⁷⁷, Kristine Wai Fun Lam¹, Michiel Lambrechts¹⁰¹,
 Helmut Lammer⁷⁷, Antonino Francesco Lanza¹¹,
 Alessandro Lanzafame¹⁵³, Mariel Lares Martiz⁵⁰,
 Jacques Laskar⁵⁵, Henrik Latter¹⁵⁴, Tony Lavanant⁸⁸,
 Alastair Lawrenson²⁶, Cecilia Lazzoni¹⁴, Agnes Lebre¹¹⁵,
 Yveline Lebreton^{6,155}, Alain Lecavelier des Etangs¹³⁶,
 Zoe Leinhardt¹⁵⁶, Adrien Leleu⁷⁵, Monika Lendl⁷⁵,
 Giuseppe Leto¹¹, Yves Levillain⁷, Anne-Sophie Libert¹⁵⁷,
 Tim Lichtenberg¹⁵⁸, Roxanne Ligi⁷⁰, Francois Lignieres⁵⁷,
 Jorge Lillo-Box⁹, Jeffrey Linsky¹⁵⁹, John Scige Liu⁷¹,
 Dominik Loidolt¹⁹, Yuying Longval¹⁷, Ilídio Lopes⁸⁶,
 Andrea Lorenzani⁹⁹, Hans-Guenter Ludwig¹⁶⁰, Mikkel Lund²²,
 Mia Sloth Lundkvist²², Xavier Luri^{93,39,94}, Carla Maceroni⁷¹,
 Sean Madden⁷, Nikku Madhusudhan³⁶, Antonio Maggio³³,
 Christian Magliano¹⁰⁷, Demetrio Magrin¹⁴, Laurent Mahy¹⁶¹,
 Olaf Maibaum¹⁶², LeeRoy Malac-Allain⁶,
 Jean-Christophe Malapert¹⁶³, Luca Malavolta¹²,
 Jesus Maldonado³³, Elena Mamonova²⁸, Louis Manchon⁵,
 Andrew Mann¹⁶⁴, Giacomo Mantovan¹², Luca Marafatto⁶⁸,
 Marcella Marconi¹¹⁴, Rosemary Mardling¹⁶⁵, Paola Marigo¹²,
 Silvia Marinoni⁴⁵, Érico Marques¹²⁷, Joao Pedro Marques¹⁷,
 Paola Maria Marrese⁴⁵, Douglas Marshall¹⁶⁶,
 Silvia Martínez Perales³⁸, David Mary⁷⁰, Francesco Marzari¹²,
 Eduard Masana^{93,39,94}, Andrina Mascher⁸⁰, Stéphane Mathis⁸⁸,
 Savita Mathur^{42,43}, Ana Carolina Mattiuci Figueiredo⁴⁴,
 Pierre F. L. Maxted¹⁶⁷, Tsevi Mazeh¹⁶⁸, Stephane Mazevet¹⁶⁹,
 Francesco Mazzei⁷¹, James McCormac¹³, Paul McMillan¹⁰¹,
 Lucas Menou⁴, Thibault Merle^{121,161}, Farzana Meru¹³,
 Dino Mesa⁶⁸, Sergio Messina¹¹, Szabolcs Mészáros^{118,170},
 Nadége Meunier⁷⁸, Jean-Charles Meunier⁴, Giuseppina Micela³³,
 Harald Michaelis¹, Eric Michel⁶, Mathias Michielsen³,

Tatiana Michtchenko²⁰, Andrea Miglio¹⁰², Yamila Miguel¹⁴⁷,
 David Milligan¹²⁶, Giovanni Mirouh¹⁷¹, Morgan Mitchell¹³,
 Nuno Moedas²⁴, Francesca Molendini⁷, László Molnár⁷⁴,
 Joey Mombarg³, Josefina Montalban¹⁰², Marco Montalto¹²,
 Mário J. P. F. G. Monteiro²⁴, Juan Carlos Morales^{103,94},
 Maria Morales-Calderon⁹, Alessandro Morbidelli⁷⁰,
 Christoph Mordasini¹⁷², Chrystel Moreau⁴, Thierry Morel⁵⁴,
 Guisepe Morello^{173,43}, Julien Morin¹¹⁵, Annelies Mortier⁵⁶,
 Benoît Mosser⁶, Denis Mourard⁷⁰, Olivier Mousis⁴,
 Claire Moutou⁵⁷, Nami Mowlavi⁷⁵, Andrés Moya¹⁷⁴,
 Prisca Muehlmann⁷, Philip Muirhead¹³⁸, Matteo Munari¹¹,
 Ilaria Musella¹¹⁴, Alexander James Mustill¹⁴⁹,
 Nicolas Nardetto⁷⁰, Domenico Nardiello¹⁴, Norio Narita^{175,42,176},
 Valerio Nascimbeni¹⁴, Anna Nash²⁶, Coralie Neiner⁶,
 Richard P. Nelson³⁴, Nadine Nettelmann¹,
 Gianalfredo Nicolini⁷⁹, Martin Nielsen⁵⁶, Sami-Matias Niemi⁷,
 Lena Noack¹⁷⁷, Arlette Noels-Grotsch⁵⁴, Anthony Noll⁶²,
 Azib Norazman¹³, Andrew J. Norton⁷⁶, Benard Nsamba⁶⁵,
 Aviv Ofir¹⁷⁸, Gordon Ogilvie¹⁵⁴, Terese Olander⁴⁶,
 Christian Olivetto¹⁰⁴, Göran Olofsson¹⁸, Joel Ong¹⁴⁰,
 Sergio Ortolani¹², Mahmoudreza Oshagh¹²², Harald Ottacher⁷⁷,
 Roland Ottensamer¹⁹, Rhita-Maria Ouazzani⁶,
 Sijme-Jan Paardekooper¹⁷⁹, Emanuele Pace¹⁸⁰, Miriam Pajas³⁸,
 Ana Palacios¹¹⁵, Gaëlle Palandri⁶, Enric Palle^{42,43},
 Carsten Paproth⁸⁰, Vanderlei Parro¹²⁷, Hannu Parviainen^{42,43},
 Javier Pascual Granado⁵⁰, Vera Maria Passegger^{181,42,43},
 Carmen Pastor-Morales⁵⁰, Martin Pätzold¹³³,
 May Gade Pedersen⁶⁴, David Pena Hidalgo⁷, Francesco Pepe¹⁶,
 Filipe Pereira²⁴, Carina M. Persson¹²⁸, Martin Pertenais⁸⁰,
 Gisbert Peter⁸⁰, Antoine C. Petit⁷⁰, Pascal Petit⁵⁷,
 Stefano Pezzuto⁷¹, Gabriele Pichierri⁷⁰, Adriano Pietrinferni⁶⁸,
 Fernando Pinheiro¹⁸², Marc Pinsonneault¹⁸³,
 Emese Plachy^{74,73,184}, Philippe Plasson⁶, Bertrand Plez¹¹⁵,
 Katja Poppenhaeger^{60,185}, Ennio Poretti⁸¹, Elisa Portaluri¹⁴,
 Jordi Portell^{93,39,94}, Gustavo Frederico Porto de Mello¹⁸⁶,
 Julien Poyatos^{93,39,94}, Francisco J. Pozuelos⁵⁰,
 Pier Giorgio Prada Moroni¹¹⁶, Dumitru Pricopi¹⁸⁷,
 Loredana Prisinzano³³, Matthias Quade⁵,

Andreas Quirrenbach¹⁶⁰, Julio Arturo Rabanal Reina⁶,
 Maria Cristina Rabello Soares⁴⁰, Gabriella Raimondo⁹⁵,
 Monica Rainer⁹⁹, Jose Ramón Rodón⁵⁰,
 Alejandro Ramón-Ballesta⁵⁰, Gonzalo Ramos Zapata³⁸,
 Stefanie Rätz¹⁸⁸, Christoph Rauterberg⁵, Bob Redman²⁶,
 Ronald Redmer¹⁸⁹, Daniel Reese⁶, Sara Regibo³,
 Ansgar Reiners¹²², Timo Reinhold⁵, Christian Renie⁶,
 Ignasi Ribas^{103,94}, Sergio Ribeiro¹²⁷, Thiago Pereira Ricciardi¹²⁷,
 Ken Rice¹⁹⁰, Olivier Richard¹¹⁵, Marco Riello³⁶,
 Michel Rieutord⁵⁷, Vincenzo Ripepi¹¹⁴, Guy Rixon³⁶,
 Steve Rockstein⁸⁰, María Teresa Rodrigo Rodríguez³⁸,
 Luisa Fernanda Rodríguez Díaz²²,
 Juan Pablo Rodríguez García⁷, Julio Rodríguez-Gomez⁵⁰,
 Yannick Roehly⁴, Fernando Roig¹⁹¹, Bárbara Rojas-Ayala¹⁹²,
 Tobias Rolf²⁸, Jakob Lysgaard Rørsted²², Hugo Rosado⁴⁹,
 Giovanni Rosotti¹⁴⁷, Olivier Roth⁶, Markus Roth¹²⁹,
 Alex Rousseau²⁶, Ian Roxburgh³⁴, Fabrice Roy⁶, Pierre Royer³,
 Kirk Ruane²⁶, Sergio Rufini Mastropasqua¹,
 Claudia Ruiz de Galarreta¹⁷, Andrea Russi⁷¹, Steven Saar¹⁹³,
 Melaine Saillenfest⁵⁵, Maurizio Salaris¹¹¹, Sebastien Salmon⁵⁴,
 Ippocratis Saltas¹⁹⁴, Réza Samadi⁶, Aunia Samadi⁵,
 Dominic Samra⁷⁷, Tiago Sanches da Silva¹²⁷,
 Miguel Andrés Sánchez Carrasco⁵⁰, Alexandre Santerne⁴,
 Francesco Santoli⁷¹, Ângela R. G. Santos²⁴, Rosario Sanz Mesa⁵⁰,
 Luis Manuel Sarro¹⁹⁵, Gaetano Scandariato¹¹, Martin Schäfer⁵,
 Edward Schlafly¹⁹⁶, François-Xavier Schmider⁷⁰,
 Jean Schneider¹⁹⁷, Jesper Schou⁵, Hannah Schunker¹⁹⁸,
 Gabriel Jörg Schwarzkopf⁸⁰, Aldo Serenelli^{103,94}, Dries Seynaeve³,
 Yutong Shan²⁸, Alexander Shapiro⁵, Russel Shipman¹⁵¹,
 Daniela Sicilia¹¹, Maria Angeles Sierra sanmartin³⁸,
 Axelle Sigot⁴, Kyle Silliman²⁶, Roberto Silvotti⁷⁹,
 Attila E. Simon¹⁰, Ricardo Simoyama Napoli¹²⁷,
 Marek Skarka^{21,199}, Barry Smalley²⁰⁰, Rodolfo Smiljanic²⁰¹,
 Samuel Smit²⁶, Alexis Smith¹, Leigh Smith³⁶, Ignas Snellen¹⁴⁷,
 Ádám Sódor⁷⁴, Frank Sohl¹, Sami K. Solanki⁵,
 Francesca Sortino⁵³, Sérgio Sousa²⁴, John Southworth¹⁶⁷,
 Diogo Souto²⁰², Alessandro Sozzetti⁷⁹, Dimitris Stamatellos²⁰³,
 Keivan Stassun¹²³, Manfred Steller⁷⁷, Dennis Stello²⁰⁴,

Beate Stelzer¹⁸⁸, Ulrike Stiebeler¹, Amalie Stokholm⁵⁶,
 Trude Storelvmo²⁸, Klaus Strassmeier⁶⁰, Paul Anthony Strøm¹³,
 Antoine Strugarek⁸⁸, Sophia Sulis⁴, Michal Švanda^{205,21},
 László Szabados^{74,73,184}, Róbert Szabó^{74,73}, Gyula M. Szabó^{118,143},
 Ewa Szuszkiewicz²⁰⁶, Geert Jan Talens³⁷, Daniele Teti⁷,
 Tom Theisen³², Frédéric Thévenin⁷⁰, Anne Thoul⁵⁴,
 Didier Tiphene⁶, Ruth Titz-Weider¹, Andrew Tkachenko³,
 Daniel Tomecki¹, Jorge Tonfat⁷⁷, Nicola Tosi¹,
 Regner Trampedach²⁰⁷, Gregor Traven¹⁰¹, Amaury Triaud⁵⁶,
 Reidar Trønnes²⁸, Maria Tsantaki⁹⁹, Matthias Tschentscher¹,
 Arnaud Turin⁴, Adam Tvaruzka⁷, Bernd Ulmer⁸⁰,
 Solène Ulmer-Moll¹⁶, Ceren Ulusoy²⁰⁸, Gabriele Umbriaco¹⁴,
 Diana Valencia²⁰⁹, Marica Valentini⁶⁰, Adriana Valio²¹⁰,
 Ángel Luis Valverde Guijarro³⁸, Vincent Van Eylen²⁶,
 Valerie Van Grootel⁵⁴, Tim A. van Kempen²³,
 Timothy Van Reeth³, Iris Van Zelst¹, Bart Vandenbussche³,
 Konstantinos Vasiliou¹, Valeriy Vasilyev⁵,
 David Vaz de Mascarenhas⁶, Allona Vazan²¹¹,
 Marina Vela Nunez⁹⁹, Eduardo Nunes Velloso⁴⁴, Rita Ventura¹¹,
 Paolo Ventura⁶⁸, Julia Venturini¹⁶, Isabel Vera Trallero³⁸,
 Dimitri Veras^{13,212,213}, Eva Verdugo⁸, Kuldeep Verma²¹⁴,
 Didier Vibert⁴, Tobias Vicanek Martinez¹⁸⁸, Krisztián Vida^{74,215},
 Arthur Vigan⁴, Antonio Villacorta⁸, Eva Villaver^{42,43},
 Marcos Villaverde Aparicio⁵⁰, Valentina Viotto¹⁴,
 Eduard Vorobyov¹⁹, Sergey Vorontsov³⁴, Frank W. Wagner²¹⁶,
 Thomas Walloschek⁷, Nicholas Walton³⁶, Dave Walton²⁶,
 Haiyang Wang^{120,217}, Rens Waters²³, Christopher Watson²¹⁸,
 Sven Wedemeyer²¹⁹, Angharad Weeks²⁶, Jörg Weingrill⁶⁰,
 Annita Weiss⁵, Belinda Wendler¹, Richard West¹³,
 Karsten Westerdorff⁸⁰, Pierre-Amaury Westphal¹⁰⁴,
 Peter Wheatley¹³, Tim White⁵¹, Amadou Whittaker⁷,
 Kai Wickhusen¹, Thomas Wilson¹³, James Windsor⁷,
 Othon Winter¹³¹, Mark Lykke Winther²², Alistair Winton⁷,
 Ulrike Witteck⁸⁰, Veronika Witzke⁵, Peter Woitke⁷⁷,
 David Wolter¹, Günther Wuchterl²²⁰, Mark Wyatt³⁶,
 Dan Yang⁵, Jie Yu⁵, Ricardo Zanmar Sanchez⁶⁸,
 María Rosa Zapatero Osorio⁹, Mathias Zechmeister²²¹,
 Yixiao Zhou¹⁰⁰, Claas Ziemke⁸⁰, Konstanze Zwintz²²².

- ¹Institute of Planetary Research, German Aerospace Center, Berlin, Germany.
- ²Free University of Berlin, Berlin, Germany.
- ³Institute of Astronomy, KU Leuven, Leuven, Belgium.
- ⁴CNRS, CNES, LAM, Aix Marseille University, Marseille, France.
- ⁵Max Planck Institute for Solar System Research, Göttingen, Germany.
- ⁶LESIA, Paris Observatory, PSL University, Sorbonne University, Paris Cité University, CNRS, Meudon, France.
- ⁷ESTEC, European Space Agency, Noordwijk, The Netherlands.
- ⁸ESAC, European Space Agency, Madrid, Spain.
- ⁹Centro de Astrobiología, CSIC-INTA, Campus ESAC, Madrid, Spain.
- ¹⁰Center for Space and Habitability, University of Bern, Bern, Switzerland.
- ¹¹INAF - Osservatorio Astrofisico di Catania, Catania, Italy.
- ¹²Department of Physics and Astronomy, University of Padua, Padua, Italy.
- ¹³Department of Physics, University of Warwick, Coventry, United Kingdom.
- ¹⁴Astronomical Observatory of Padova, INAF - Italian National Institute for Astrophysics, Padua, Italy.
- ¹⁵Armagh Observatory and Planetarium, College Hill, Armagh, United Kingdom.
- ¹⁶Geneve Observatory, University of Geneve, Geneve, Switzerland.
- ¹⁷IAS, University of Paris-Saclay, Orsay, France.
- ¹⁸AlbaNove University Centre, Stockholm University, Stockholm, Sweden.
- ¹⁹Department of Astrophysics, University of Vienna, Vienna, Austria.
- ²⁰Department of Astronomy, University of Sao Paulo, Sao Paulo, Brazil.
- ²¹Astronomical Institute of the Czech Academy of Sciences, Ondřejov, Czech Republic.
- ²²Department of Physics and Astronomy, Aarhus University, Aarhus, Denmark.
- ²³Institute for Space Research, SRON, Leiden, The Netherlands.
- ²⁴Instituto de Astrofísica e Ciências do Espaço, CAUP, Universidade do Porto, Porto, Portugal.
- ²⁵Departamento de Física e Astronomia, Faculdade da Ciências, Universidade do Porto, Porto, Portugal.
- ²⁶Mullard Space Science Laboratory, University College London, Holmbury Saint Mary, United Kingdom.
- ²⁷Dept. Theoretical Physics and the Cosmos, University of Granada, Granada, Spain.

- ²⁸Centre for Planetary Habitability, Centre for Earth Evolution and Dynamics, Department of Geosciences, University of Oslo, Oslo, Norway.
- ²⁹CISAS G. Colombo University of Padua, Padua, Italy.
- ³⁰Faculty of Sciences, University of Lisbon, Lisbon, Portugal.
- ³¹Max-Planck-Institute for Astronomy, Heidelberg, Germany.
- ³²University of Applied Sciences Aachen, Aachen, Germany.
- ³³Palermo Astronomical Observatory, INAF - Italian National Institute for Astrophysics, Palermo, Italy.
- ³⁴Department of Physics & Astronomy, Queen Mary University of London, London, United Kingdom.
- ³⁵DARK, Niels Bohr Institute, University of Copenhagen, Copenhagen, Denmark.
- ³⁶Institute of Astronomy, University of Cambridge, Cambridge, United Kingdom.
- ³⁷University of Oxford, Oxford, United Kingdom.
- ³⁸INTA - National Institute of Aerospace Technology, Madrid, Spain.
- ³⁹Departament de Física Quàntica i Astrofísica (FQA), Universitat de Barcelona (UB), Barcelona, Spain.
- ⁴⁰Department of Physics, University of Minas Gerais, Minas Gerais, Brazil.
- ⁴¹School of Physics & Astronomy, University of Leicester, Leicester, United Kingdom.
- ⁴²IAC - Canary Islands Institute of Astrophysics, Tenerife, Spain.
- ⁴³Departamento de Astrofísica, Universidad de La Laguna, Tenerife, Spain.
- ⁴⁴Department of Physics, University Rio Grande do Norte, Rio Grande do Norte, Brazil.
- ⁴⁵ASI Headquarters, ASI - Space Science Data Center, Rome, Italy.
- ⁴⁶Department of Physics and Astronomy, Uppsala University, Uppsala, Sweden.
- ⁴⁷Department of Physics, State University of Feira de Santana, Feira de Santana, Brazil.
- ⁴⁸Astronomical Observatory, University of Ponta Grossa, Ponta Grossa, Brazil.
- ⁴⁹Deimos Engenharia, Lisbon, Portugal.
- ⁵⁰IAA - Institute of Astrophysics of Andalusia, CSIC - Spanish National Research Council, Granada, Spain.
- ⁵¹Research School of Astronomy and Astrophysics, Australian National University, Canberra, Australia.

- ⁵²Kavli Institute for Astrophysics and Space Research,Massachusetts
Institute of Technology, Cambridge, United States.
- ⁵³Astrophysics and Space Science Observatory of Bologna,INAF - Italian
National Institute for Astrophysics, Bologna, Italy.
- ⁵⁴Space sciences, Technologies and Astrophysics Research (STAR)
Institute,Université de Liège, Liège, Belgium.
- ⁵⁵IMCCE,Observatory of Paris, Paris, France.
- ⁵⁶School of Physics & Astronomy,University of Birmingham,
Birmingham, United Kingdom.
- ⁵⁷IRAP - Institute for Research in Astrophysics and Planetology,
Toulouse, France.
- ⁵⁸University of Atacama, Copiapó, Chile.
- ⁵⁹School of Mathematics,University of Leeds, Leeds , United Kingdom.
- ⁶⁰Leibniz Institute for Astrophysics Potsdam , Potsdam, Germany.
- ⁶¹Astronomy Department,Yale University, New Haven, United States.
- ⁶²Heidelberg Institute for Theoretical Studies, Heidelberg, Germany.
- ⁶³Institute for Physics,University of Graz, Graz, Austria.
- ⁶⁴School of Physics,University of Sydney, Sydney, Australia.
- ⁶⁵Max Planck Institute for Astrophysics, Garching, Germany.
- ⁶⁶Solar Science Observatory,National Astronomical Observatory of
Japan, Mitaka, Tokyo, Japan.
- ⁶⁷Center for Space Science,New York University Abu Dhabi, Abu Dhabi,
United Arab Emirates.
- ⁶⁸Astronomical Observatory of Rome,INAF - Italian National Institute
for Astrophysics, Rome, Italy.
- ⁶⁹Astronomical Observatory of Trieste,INAF - Italian National Institute
for Astrophysics, Trieste, Italy.
- ⁷⁰Observatoire de la Côte d'Azur, CNRS, Laboratoire
Lagrange,Université Côte d'Azur, Nice, France.
- ⁷¹IAPS,INAF - Italian National Institute for Astrophysics, Rome, Italy.
- ⁷²Konkoly Observatory,Research Centre for Astronomy and Earth
Sciences, ELKH, MTA Centre of Excellence, Konkoly, Budapest,
Hungary.
- ⁷³Near-Field Cosmology Research Group,MTA CSFK Lendület ,
Budapest, Hungary.
- ⁷⁴,Konkoly Observatory, CSFK, MTA Centre of Excellence, Konkoly,
Budapest, Hungary.
- ⁷⁵Departement of Astronomy,University of Geneve , Geneve , Switzerland.
- ⁷⁶School of Physical Sciences,The Open University, Milton Keynes,
United Kingdom.

- ⁷⁷Space Research Institute,Austrian Academy of Science, Graz, Austria.
- ⁷⁸IPAG,University of Grenoble Alpes, Grenoble, France.
- ⁷⁹Turin Astrophysical Observatory,INAF - Italian National Institute for Astrophysics, Turin, Italy.
- ⁸⁰Institute of Optical Sensor Systems ,German Aerospace Center, Berlin, Germany.
- ⁸¹Brera Astronomical Observatory,INAF - Italian National Institute for Astrophysics, Merate , Italy.
- ⁸²National Observatory,LIneA - International Laboratory of Astronomy, Rio de Janeiro, Brazil.
- ⁸³School of Mathematics, Statistics and Physics,Newcastle University, Newcastle upon Tyne, United Kingdom.
- ⁸⁴University of Auckland , Auckland , New Zealand.
- ⁸⁵SISSA,International School for Advanced Studies, Trieste, Italy.
- ⁸⁶Centro de Astrofísica e Gravitação (CENTRA), Departamento de Física, Instituto Superior Técnico - IST,Universidade de Lisboa, Lisboa, Portugal.
- ⁸⁷Department of Physics,University of Turin , Turin, Italy.
- ⁸⁸CEA, CNRS, AIM,Université Paris-Saclay, Université Paris Cité, Gif-sur-Yvette, France.
- ⁸⁹DTU Space,Technical University of Denmark, Copenhagen, Denmark.
- ⁹⁰Institute of Science & Technology, Klosterneuburg, Austria.
- ⁹¹Dept, of Chemistry and Physics,Florida Gulf Coast University, Fort Myers, United States.
- ⁹²School of Physics and Astronomy,University of St Andrews , St Andrews , United Kingdom.
- ⁹³Institut de Ciències del Cosmos (ICCUB),Universitat de Barcelona (UB), Barcelona, Spain.
- ⁹⁴Institut d'Estudis Espacials de Catalunya (IEEC), Barcelona, Spain.
- ⁹⁵Astronomical Observatory of Abruzzo,INAF - Italian National Institute for Astrophysics, Teramo , Italy.
- ⁹⁶INFN - Sezione di Pisa, Pisa, Italy.
- ⁹⁷Instituto de Astrofísica,Pontificia Universidad Católica de Chile, Santiago, Chile.
- ⁹⁸Millennium Institute of Astrophysics, Santiago, Chile.
- ⁹⁹Arcetri Astrophysical Observatory,INAF - Italian National Institute for Astrophysics, Florence, Italy.
- ¹⁰⁰Stellar Astrophysics Centre, Department of Physics and Astronomy,Aarhus University, Aarhus, Denmark.
- ¹⁰¹Lund Observatory,Lund University, Lund, Sweden.

- ¹⁰²Department of Physics and Astronomy,University of Bologna,
Bologna, Italy.
- ¹⁰³Institut de Ciències de l’Espai (ICE, CSIC),Campus UAB, Barcelona,
Spain.
- ¹⁰⁴IAS,University of Paris-Saclay, Bures-sur-Yvette, France.
- ¹⁰⁵CFisUC, Physics Department,University of Coimbra, Coimbra,
Portugal.
- ¹⁰⁶FGG,INAF - Italian National Institute for Astrophysics, Brena Baja,
Spain.
- ¹⁰⁷University of Naples Federico II, Napoli, Italy.
- ¹⁰⁸College of Engineering, Mathematics and Physical Sciences,University
of Exeter, Exeter, United Kingdom.
- ¹⁰⁹Institute of Sciences,Federal University of Southern and Southeastern
Pará, Marabá, Brazil.
- ¹¹⁰Centre for Mathematical Sciences,Lund University, Lund, Sweden.
- ¹¹¹Astrophysics Research Institute,John Moores University, Liverpool,
United Kingdom.
- ¹¹²National Astrophysics Laboratory, Itajubá - MG, Brazil.
- ¹¹³Department of Physics,Federal University of Ceará, Ceará, Brazil.
- ¹¹⁴Capodimonte Astronomical Observatory,INAF - Italian National
Institute for Astrophysics, Napoli, Italy.
- ¹¹⁵Laboratoire Univers et Particules de Montpellier, CNRS,Université de
Montpellier, Montpellier, France.
- ¹¹⁶Department of Physics,Pisa University, Pisa, Italy.
- ¹¹⁷Instituto de Astrofísica de Canarias, Tenerife, Spain.
- ¹¹⁸Gothard Astrophysical Observatory,ELTE Eötvös Loránd University,
Szombathely, Hungary.
- ¹¹⁹Valencia Internacional University, Alicante, Spain.
- ¹²⁰Institute for Particle Physics and Astrophysics,ETH Zurich, Zurich,
Switzerland.
- ¹²¹Free University of Brussels, Brussels, Belgium.
- ¹²²Institute for Astrophysics and Geophysics,Georg-August-University of
Göttingen, Göttingen, Germany.
- ¹²³Department of Physics and Astronomy,Vanderbilt University,
Nashville, United States.
- ¹²⁴Polytechnic School,University of Sao Paulo, Sao Paulo, Brazil.
- ¹²⁵European Southern Observatory , Santiago, Chile.
- ¹²⁶ESOC,European Space Agency, European Space Agency, Germany.
- ¹²⁷Maua Institute of Technology ,IMT University, Sao Paulo, Brazil.

- ¹²⁸Department of Space Earth and Environment,Chalmers University of Technology, Onsala, Sweden.
- ¹²⁹Thüringer Landessternwarte Tautenburg, Tautenburg, Germany.
- ¹³⁰Max-Planck-Institute for Astronomy, Neckargemuend, Germany.
- ¹³¹Sao Paulo State University, Sao Paulo, Brazil.
- ¹³²Centro di Ateneo di Studi e Attività Spaziali "Giuseppe Colombo",Università di Padova, Padova, Italy.
- ¹³³RIU,University of Cologne, Köln, Germany.
- ¹³⁴Department of Physics & Astronomy,University of Georgia, Athens, United States.
- ¹³⁵Kavli Institute for Cosmology, Institute of Astronomy,University of Cambridge, Cambridge, United Kingdom.
- ¹³⁶IAP - Institute of Astrophysics , Paris, France.
- ¹³⁷Nicolaus Copernicus Astronomical Center,Polish Academy of Sciences, Torun, Poland.
- ¹³⁸Boston University, Boston, United States.
- ¹³⁹Southwest Research Institute,Arizona State University, Texas, United States.
- ¹⁴⁰University of Hawai'i, Honolulu , United States.
- ¹⁴¹Department of Earth, Environmental and Planetary Sciences, and Department of Physics and Astronomy,Rice University, Texas, United States.
- ¹⁴²Astronomy Nucleus,Diego Portales University, Santiago, Chile.
- ¹⁴³Exoplanet Research Group,MTA-ELTE, Szombathely, Hungary.
- ¹⁴⁴Doctoral School of Physics,ELTE Eötvös Loránd University, Budapest, Hungary.
- ¹⁴⁵Department of Geoscience,Aarhus University, Aarhus, Denmark.
- ¹⁴⁶Iowa State University, Ames, United States.
- ¹⁴⁷Leiden Observatory,Leiden University, Leiden, The Netherlands.
- ¹⁴⁸Institute of Theoretical Physics and Astronomy,Vilnius University, Vilnius, Lithuania.
- ¹⁴⁹Lund Observatory, Division of Astrophysics, Department of Physics,Lund University, Lund, Sweden.
- ¹⁵⁰Dept. Applied Mathematics & Physics,University of Applied Sciences Technikum Wien, Vienna, Austria.
- ¹⁵¹Institute for Space Research,SRON , Groningen, The Netherlands.
- ¹⁵²UTINAM Institute , Besançon, France.
- ¹⁵³Department of Physics and Astronomy,University of Catania, Catania, Italy.

- ¹⁵⁴Centre for Mathematical Sciences,University of Cambridge,
Cambridge, United Kingdom.
- ¹⁵⁵IPR,University of Rennes, Rennes, France.
- ¹⁵⁶H.H. Wills Physics Laboratory,University of Bristol, Bristol, United
Kingdom.
- ¹⁵⁷naXys Research Institute,University of Namur, Namur, Belgium.
- ¹⁵⁸Kapteyn Astronomical Institute,University of Groningen, Groningen,
The Netherlands.
- ¹⁵⁹University of Colorado, Boulder , United States.
- ¹⁶⁰Landessternwarte,Heidelberg University, Heidelberg, Germany.
- ¹⁶¹Royal Observatory of Belgium, Brussels, Belgium.
- ¹⁶²Institute for Software Technology,German Aerospace Center,
Braunschweig, Germany.
- ¹⁶³CNES - National Centre for Space Studies , Toulouse, France.
- ¹⁶⁴University of North Carolina at Chapel Hill, Chapel Hill, United
States.
- ¹⁶⁵School of Physics and Astronomy,Monash University, Melbourne,
Australia.
- ¹⁶⁶AIM-CEA,Paris Diderot University, Paris, France.
- ¹⁶⁷Astrophysics Group ,Keele University, Staffordshire, United Kingdom.
- ¹⁶⁸Tel Aviv University, Tel Aviv, Israel.
- ¹⁶⁹PSL University, Paris, France.
- ¹⁷⁰"Momentum" Milky Way Research Group,MTA-ELTE Lendület,
Szombathely, Hungary.
- ¹⁷¹University of Surrey, Guildford , United Kingdom.
- ¹⁷²Division of Space Research and Planetary Sciences,University of Bern,
Bern, Switzerland.
- ¹⁷³Department of Space, Earth and Environment,Chalmers University of
Technology, Gothenburg, Sweden.
- ¹⁷⁴University of Valencia, Valencia, Spain.
- ¹⁷⁵Komaba Institute for Science,University of Tokyo, Meguro, Tokyo,
Japan.
- ¹⁷⁶Astrobiology Center, Mitaka, Tokyo, Japan.
- ¹⁷⁷Institute of Geological Sciences,Free University of Berlin, Berlin,
Germany.
- ¹⁷⁸Weizmann Institute of Science, Rehovot , Israel.
- ¹⁷⁹Delft University of Technology , Delft, The Netherlands.
- ¹⁸⁰University of Florence , Florence, Italy.
- ¹⁸¹Hamburg Observatory,University of Hamburg , Hamburg, Germany.

- ¹⁸²Geophysical and Astronomical Observatory,University of Coimbra,
Coimbra, Portugal.
- ¹⁸³Institute for Astronomy,Ohio State University, Columbus, United
States.
- ¹⁸⁴Institute of Physics,ELTE Eötvös Loránd University, Budapest,
Hungary.
- ¹⁸⁵Institute for Physics and Astronomy,Potsdam University, Potsdam,
Germany.
- ¹⁸⁶Observatory of Valongo,Federal University of Rio de Janeiro , Rio de
Janeiro, Brazil.
- ¹⁸⁷Astronomical Institute ,Romanian Academy, Bucharest , Romania.
- ¹⁸⁸Institute for Astronomy and Astrophysics,University of Tuebingen,
Tübingen, Germany.
- ¹⁸⁹Institute of Physics,University of Rostock, Rostock, Germany.
- ¹⁹⁰Institute for Astronomy, The Royal Observatory,University of
Edinburgh, Edinburgh, United Kingdom.
- ¹⁹¹National Observatory Rio de Janeiro, Rio de Janeiro, Brazil.
- ¹⁹²Instituto de Alta Investigación,Universidad de Tarapacá, Arica, Chile.
- ¹⁹³Center for Astrophysics,Harvard & Smithsonian, Cambridge, United
States.
- ¹⁹⁴Institute of Physics,Czech Academy of Science, Praha, Czech Republic.
- ¹⁹⁵National Distance Education University, Madrid , Spain.
- ¹⁹⁶Lawrence Berkeley Laboratory,University of California, Berkeley,
United States.
- ¹⁹⁷LUTH, UMR 8102,Paris Observatory, Meudon, France.
- ¹⁹⁸The University of Newcastle, Newcastle, Australia.
- ¹⁹⁹Department of Theoretical Physics and Astrophysics,Masaryk
University, Brno, Czech Republic.
- ²⁰⁰Lennard-Jones Laboratory,Keele University, Staffordshire, United
Kingdom.
- ²⁰¹Nicolaus Copernicus Astronomical Center,Polish Academy of
Sciences, Warsaw, Poland.
- ²⁰²Federal University of Sergipe, Sao Cristovao, Brazil.
- ²⁰³Jeremiah Horrocks Institute,University of Central Lancashire,
Preston, United Kingdom.
- ²⁰⁴School of Physics,University of New South Wales, New South Wales,
Australia.
- ²⁰⁵Faculty of Mathematics and Physics,Charles University , Praha,
Czech Republic.
- ²⁰⁶Institute of Physics and CASA*,University of Szczecin, Szczecin,
Poland.

- ²⁰⁷Space Science Institute, Boulder, United States.
²⁰⁸Girne American University, Kyrenia, Cyprus.
²⁰⁹University of Toronto, Toronto, Canada.
²¹⁰Center for Radio Astronomy and Astrophysics, Mackenzie
Presbyterian University, Sao Paulo, Brazil.
²¹¹Natural Sciences Department, Open University of Israel, Israel.
²¹²Centre for Exoplanets and Habitability, University of Warwick,
Coventry, United Kingdom.
²¹³Centre for Space Domain Awareness, University of Warwick, Coventry,
United Kingdom.
²¹⁴Department of Physics, Indian Institute of Technology (BHU),
Varanasi-221005, India.
²¹⁵Department of Astronomy, ELTE Eötvös Loránd University, Budapest,
Hungary.
²¹⁶ Institute for Advanced Simulation, Forschungszentrum Jülich, Jülich,
Germany.
²¹⁷Institute of Geochemistry and Petrology, ETH Zurich, Zurich,
Switzerland.
²¹⁸Astrophysics Research Centre, School of Mathematics and
Physics, Queens University Belfast, Belfast, United Kingdom.
²¹⁹Rosseland Centre for Solar Physics, Institute of Theoretical
Astrophysics, University of Oslo, Oslo, Norway.
²²⁰Kuffner Observatory, Vienna, Austria.
²²¹Universität Göttingen, Göttingen, Germany.
²²²Institute for Astro- and Particle Physics, University of Innsbruck,
Innsbruck, Austria.
²²³Instituto Superior de Gestão, Lisbon, Portugal.

.

Version submitted to Experimental Astronomy .

Abstract

PLATO (PLANetary Transits and Oscillations of stars) is ESA's M3 mission designed to detect and characterise extrasolar planets and perform asteroseismic monitoring of a large number of stars. PLATO will detect small planets (down to $<2 R_{\text{Earth}}$) around bright stars (<11 mag), including terrestrial planets in the habitable zone of solar-like stars. With the complement of radial velocity observations from the ground, planets will be characterised for their radius, mass, and

age with high accuracy (5%, 10%, 10% for an Earth-Sun combination respectively). PLATO will provide us with a large-scale catalogue of well-characterised small planets up to intermediate orbital periods, relevant for a meaningful comparison to planet formation theories and to better understand planet evolution. It will make possible comparative exoplanetology to place our Solar System planets in a broader context. In parallel, PLATO will study (host) stars using asteroseismology, allowing us to determine the stellar properties with high accuracy, substantially enhancing our knowledge of stellar structure and evolution.

The payload instrument consists of 26 cameras with 12cm aperture each. For at least four years, the mission will perform high-precision photometric measurements. Here we review the science objectives, present PLATO’s target samples and fields, provide an overview of expected core science performance as well as a description of the instrument and the mission profile at the beginning of the serial production of the flight cameras. PLATO is scheduled for a launch date end 2026. This overview therefore provides a summary of the mission to the community in preparation of the upcoming operational phases.

Keywords: PLATO mission, exoplanets, asteroseismology

Contents

1	Introduction	20
2	Overview of PLATO Science Objectives	21
3	Exoplanet Science	24
3.1	Exoplanet Detection	24
3.1.1	State of the Art	24
3.1.2	Expected PLATO Planet Detection Yield	27
3.2	Planet Characterisation	36
3.2.1	Brief summary of state of the art	36
3.2.2	Expected planetary radius accuracy	39
3.3	Constraints on planetary atmospheres	42
3.4	Constraints on planet formation and evolution	43
4	Stellar Science	45
4.1	State of the art of seismic stellar characterisation	45
4.1.1	Ultra-precise photometric seismology: the space era	45
4.1.2	Ultra-precise seismic stellar characterisation with <i>Kepler</i>	47
4.2	Precision versus accuracy	51
4.3	Detecting solar-like oscillations with PLATO	54
4.3.1	Expected solar-like oscillations within the PLATO P1-P2 sample	54
4.3.2	Expected solar-like oscillations within PLATO P5 sample	57
4.4	PLATO seismic performance for stellar mass, radius, and age characterisation for the P1–P2 sample	58

4.5	Expectations for M dwarfs (P4 Sample)	61
4.6	Measurement of surface rotation period, stellar activity indices and flares	62
5	The PLATO Complementary Science programs	63
5.1	Background	63
5.2	Support for the community	64
5.3	Example 1: g-mode asteroseismology	65
5.4	Example 2: red giants and stellar ages	66
5.5	Example 3: transient studies	67
6	PLATO Stellar Target Samples	68
6.1	Stellar Samples Definition	68
6.1.1	The bright samples (P1 and P2)	68
6.1.2	The "M dwarf sample" (P4)	70
6.1.3	The "statistical sample" (Sample P5)	70
6.1.4	The "prime" sample	70
6.2	Light curves versus Imagettes	71
7	Target Fields and Observing Strategy	72
8	The PLATO Science Ground Segment: Data Products and Releases	74
8.1	Generation of the Data Products	74
8.2	Data Products	76
8.3	Data Releases	77
9	The Ground-based Observations Programme	78
10	The Guest Observer Programme	79
11	Expected Instrument Performance	80
12	PLATO spacecraft and mission configuration	83
12.1	PLATO spacecraft	83
12.2	Launch and operations	85
13	Payload design overview	86
13.1	General payload description	86
13.2	PLATO Cameras	87
13.3	PLATO Data Processing System	91
14	Synergies with other Missions	94
15	Appendix A	100

1 Introduction

The PLATO mission (PLANetary Transits and Oscillations of stars) is able to detect and characterise a large number of exoplanetary systems, including terrestrial exoplanets orbiting bright solar-type stars in their habitable zone. PLATO was selected as ESA’s M3 mission in the Cosmic Vision 2015-2025 Programme in 2014 (Rauer et al, 2014). PLATO satellite data will provide accurate and precise planetary radii and architectures of a large number of planetary systems via the photometric transit method. The light curve data will also enable accurate stellar parameters, including evolutionary ages, to be derived via asteroseismic analysis. In combination with high-precision spectroscopic ground-based follow-up observations, accurate planetary masses, and hence mean planetary densities, will be determined.

The overall scientific objectives that PLATO will investigate are:

- How do planets and planetary systems form and evolve?
- Is our Solar System special or are there other systems like ours?
- Are there potentially habitable planets?

The photometric precision and observing mode of PLATO will help determine the frequency of Earth-like planets. In general, analysis of PLATO data is expected to give new insights into the formation and evolution of planets and planetary systems as well as the evolution of stars.

Benchmark cases will be used to improve stellar models to further minimise the impact of poorly understood internal physics on stellar parameters. With these benchmark cases, classical methods for stellar modelling can also be improved. Furthermore, light curves are used to determine the magnetic variability and activity of planet host stars. The combined analysis of improved stellar physics and well-characterised host stars with high photometric precision light curves and follow-up data will provide accurate planetary parameters. Such parameters are key ingredients for the analysis of the planetary radius, mass, density, and age with important implications for models of interior structure and planetary evolution.

The PLATO satellite consists of an ESA-provided satellite platform and a payload including 26 cameras, on-board computers and power supply units jointly developed by ESA and the international PLATO Mission Consortium (PMC). Launch is foreseen for end 2026. The cameras will operate in white light and obtain high-precision photometric light curves of thousands of stars.

The initial PLATO mission layout and its science objectives are described in Rauer et al (2014), presenting the status just before mission selection. In the present paper we summarise the status of the consolidated mission design at the beginning of flight model production and show the mission in the context of current exoplanetary research. We provide an overview of the expected impact in exoplanet science including planet yields and performance for planet characterisation (Section 3). Section 4 discusses PLATO’s impact on stellar science, including a discussion on accuracy versus precision and the prospects for detecting solar-like oscillations in PLATO samples. The potential of PLATO concerning complementary sciences beyond its core programme is discussed in Section 5. Section 6 defines the PLATO P1 to P5 stellar samples

and presents options for the distribution of on-board processed light curves versus imagettes for detailed analysis on ground. The status of target field and observing mode selection is summarised in Section 7. The science ground segment, PLATO data products and data releases are presented in Section 8. The organised ground-based follow-up to determine masses for planets in PLATO’s prime sample is a key element of the mission (Section 9). In addition to its core science goals, PLATO will provide a wealth of complementary science data available via the Guest Observer programme, which will be part of the legacy of the mission, see Section 10. The expected instrument signal-to-noise levels as well as the mission and payload designs are highlighted in Sections 11, 12 and 13. Finally, the synergies with other missions are presented in 14.

2 Overview of PLATO Science Objectives

The scientific programme of PLATO addresses the following science goals in the fields of exoplanet and stellar sciences:

- *Determine the bulk properties (radius, mass, and mean density) of planets in a wide range of systems, including terrestrial planets in the habitable zone (HZ) of solar-like stars.*

Among the key goals of PLATO are high accuracy parameters for planets orbiting F5-K7 dwarf and sub-giant stars. Note that we use the term “accurate” planet parameters for those cases where stellar parameters can be derived with highest precision and stellar models are well constrained (see Section 4). For an Earth-sized planet (Earth radius: r_e) orbiting a 10 mag G0V star an accuracy of 3% in planetary radius (5% for a 11 mag star) and 10% in stellar age shall be derived. This configuration is used as the benchmark for the mission. Better precision is expected for larger planets or brighter host stars (see Section 3.2). In addition, PLATO will observe stars that are sufficiently bright to enable the determination of planetary masses (Earth mass: m_e) with an accuracy of 10% for a terrestrial planet (defined as $\leq 2 R_e$ and $\leq 10 M_e$) orbiting a G0V star via the radial velocity method from ground-based follow-up observations. The resulting planetary bulk properties allow us to explore the diversity of planets and identify typical planet populations, which in turn help better constrain planet formation models. Small planets with high mean densities in the HZ will be prime candidates for potentially habitable planets and allow an estimation of η_{Earth} , here defined as the fraction of Earth-like planets in the HZ per host star. Furthermore, precise measurements for close-in high-density planets will show how many have a Mercury-like interior structure which will allow a study of their refractory (e.g. Fe and Si) content and help test formation theories for this class of planets. Extending our knowledge towards longer orbital periods will show whether extreme-density small planets also exist on such orbits. Other questions which can be addressed with PLATO data (and combined with e.g. stellar properties) include, “What is a typical internal structure and composition of terrestrial and mini-gas planets? How does it evolve

due to stellar interactions (losses)? What is the core size of gaseous planets?”.

- *Study how planets and planetary systems evolve with age.*

The age of planetary systems is a key parameter to explore how planetary system properties evolve and provides observational constraints to formation models as well as to how gravitational instabilities deplete planetary systems over time (Veras et al, 2015). Furthermore, details of the evolutionary stages of planets are only known from one example so far, our Solar System. In particular for terrestrial planets and their complex evolution as well as for the new and poorly known class of mini-Neptunes better constraints can be provided once a sample of planets observed at different evolution stages becomes available. Open questions are, e.g., “When does the magma ocean phase for terrestrial planets end?” and “Are our model timescales for the evolution of gaseous planets correct?”. To further our understanding of these issues, homogeneous and precise age determination is required, an issue we are still facing today with the various age indicators. The seismic characterisation of a large sample of bright stars across the Hertzsprung-Russell (HR) diagram will lead to significantly improved stellar models, allowing for substantially more reliable age characterisation of stars in general.

- *Study the typical architectures of planetary systems.*

The architecture of planetary systems includes parameters such as the distribution of planet masses and types (terrestrial or gaseous) over orbital separation, the coplanarity of systems, and orbital parameters such as, e.g., orbital eccentricities (e.g. Van Eylen and Albrecht 2015; Van Eylen et al 2019) and inclinations. Key questions to address include, e.g., “What fraction of planetary systems have a structure similar to the Solar System? How many have multiple/no gas giants? Was migration caused by planet-planet interaction or disk migration?”. First analyses of *Kepler* mission results, but also comparisons with planet synthesis models (e.g. Borucki et al 2010; Lissauer et al 2011; Weiss et al 2018; Millholland et al 2017; Wang and Ji 2017; Mishra et al 2021) suggest adjacent planets having similar masses and sizes with a trend towards increasing masses for outer planets. Dynamical interactions between planet embryos can lead to typical spacing between planets with small planets being more densely packed than large/massive ones. Today, these apparent trends are based on only a few tens of well-characterised planetary systems in a limited parameter space (e.g., Mishra et al, 2021) and there are many exceptions to the trends. Furthermore, the dynamical evolution and development of, e.g., orbital resonances during early ages of planetary systems need to be better understood and linked to system properties. Nevertheless, the available early studies already show the large potential for well-characterised samples of planet system architectures to constrain planet formation theories. PLATO will significantly extend the number of well-characterised planetary systems, in particular for longer orbital periods longer than 80 days. These longer periods are underrepresented in past and ongoing mission data (see Section 3.1.2 for a comparison to the Transiting

Exoplanet Survey Satellite (TESS, [Ricker et al 2015](#)).

- *Analyse the correlation of planet properties and their frequencies with stellar parameters (e.g., stellar metallicity, stellar type).*

Occurrence rates for different types of planets around different types of stars have been provided by both transit and radial velocity surveys (e.g. [Howard et al 2012](#); [Fressin et al 2013](#); [Christiansen et al 2015](#); [Deleuil et al 2018](#); [Kunimoto et al 2022](#), see Section 3.1.2 for more). A proper estimate of an occurrence rate requires however a good estimate of some key parameters such as the survey detection sensitivity to estimate its completeness, the planet parameters, and a good knowledge of the underlying stellar population. The latter is a serious limitation that prevents direct comparisons of published occurrence rates and limits the reliability of the estimates. PLATO will benefit from the in-depth characterisation of the stellar fields the instrument will observe and an analysis with the most up-to-date stellar models. This will allow for the exploration of possible correlations of planet parameters with stellar properties. For example, the chemical element ratios of a stellar photosphere is thought to be a good first proxy of its planets' initial compositions alleviating the degeneracies that occur when deriving the planet's composition from its radius and mass only ([Dorn et al, 2015](#); [Brugger et al, 2017](#); [Acuña et al, 2021](#)). This hypothesis has been recently questioned by various studies ([Plotnykov and Valencia, 2020](#); [Schulze et al, 2021](#); [Adibekyan et al, 2021](#)) which highlight discrepancies between the actual planetary composition and what is expected from a primordial origin as reflected by the chemical ratios of the stars. In addition, stellar properties such as activity are key parameters for our understanding of potential planet habitability. In particular, stellar rotational evolution is a key ingredient to understand planetary migration through tidal and magnetic interaction (e.g. [Lai 2012](#); [Mathis et al 2018](#); [Strugarek et al 2018, 2019](#); [Damiani and Mathis 2018](#); [Ahuir et al 2021](#)).

- *Analyse the dependence of the frequency of terrestrial planets on the environment in which they formed.*

Planets form in different regions of our Galaxy, in clusters and around field stars. Correlations of planet occurrence frequency with their environment will provide constraints on planetary formation processes.

- *Study the internal structure of stars and how it evolves with age.*

Determining planet host star parameters requires improving today's stellar models and stellar evolution theory in general. PLATO light curve data will be used to measure the oscillation frequencies of stars, which will be interpreted via asteroseismic modelling (e.g., [García and Ballot, 2019](#); [Aerts, 2021](#), for recent reviews) to test evolution theory. Stellar models constrained by asteroseismology and cross-calibration

with classical methods of stellar modelling will be key in obtaining planet host star parameters to address the overall PLATO science goals.

In the absence of seismic age determination, measurements of rotation periods from the PLATO light curves will allow us to estimate the age of a given target through gyrochronology (Skumanich, 1972; Barnes, 2003, 2007) for stars like solar-type stars which are losing angular momentum through the stellar wind due to their magnetic activity. The PLATO rotation period catalogue will complete and extend the catalogues already available for *Kepler*/K2/TESS (e.g. Nielsen et al 2013; McQuillan et al 2014a; Santos et al 2019, 2021; Holcomb et al 2022). It is also expected to detect and characterise activity cycles which are shorter than the solar cycle, such as the Rieger-like cycle (Rieder and Kenworthy, 2016; Gurgenshvilili et al, 2021). For stars with planets it is furthermore important to understand how activity and rotation is affected by close-in planets, a task for which PLATO will expand our currently available data base.

- *Identify good targets for spectroscopic follow-up measurements to investigate planetary atmospheres.*

Planets identified around the brightest stars will likely be “Rosetta Stones” for spectroscopic follow-up to study their atmospheric structure and composition. Apart from the gaseous planets, those low-mass PLATO planets accessible to e.g. JWST (James-Web-Space-Telescope), or its successors, have the potential to provide new insights into the link between mantle composition, iron-to-silicate ratio, redox state and atmospheric compositions. They would allow, e.g., the identification of secondary atmospheres (water, CO₂) on such low-mass planets (e.g., Ortenzi et al 2020; Kabath et al 2007), which are barely distinguishable from just mass and radius modelling alone.

To reach these objectives, PLATO data will encompass a greater parameter space - well beyond those accessible by previous and ongoing exoplanet missions. In addition, PLATO will address a large number of complementary and legacy science topics, e.g., asteroseismology of young massive single and binary stars, of evolved stars nearing the end of their lives, and of compact objects. PLATO’s asteroseismic characterisation of stellar ensembles, binaries, clusters and populations will be a significant addition to the Gaia and *Kepler* data, to mention some examples of the huge legacy of PLATO.

The following chapters detail PLATO’s science objectives and provide analysis of the respective accuracy and precision that the instrument can achieve.

3 Exoplanet Science

3.1 Exoplanet Detection

3.1.1 State of the Art

The pioneering early discoveries made by ground-based telescopes (e.g. WASP (Pol-lacco et al, 2006), HATNet (Bakos et al, 2004)) and the CoRoT space mission (Baglin

et al, 2006; Deleuil et al, 2018) provided a first glimpse on the diversity of extrasolar giant and close-in planet properties. It was, however, the *Kepler* mission (Koch et al, 2010; Borucki et al, 2011) which enlarged the sample of small-sized planets and enabled the first studies on exoplanet population properties (Batalha, 2014). For ensemble properties to become apparent, a sufficiently large number of planets with well-known parameters are needed. Today, TESS data provide a wealth of information on the population of planets with orbital periods up to about 100 days (Guerrero et al, 2021).

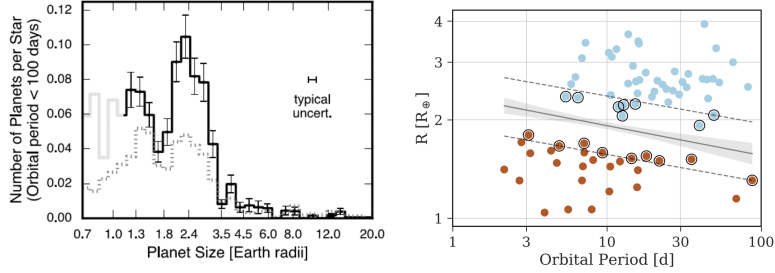


Fig. 1 Planetary populations found from the accurately characterised *Kepler* host stars. The left panel shows the bi-modal distribution found in planetary radii (Fulton et al (2017); Fulton and Petigura (2018), their Fig. 5 shown). The right panel shows the slope of the radii gap with increasing orbital period, derived using asteroseismology for improved stellar and planetary parameters (Van Eylen et al (2018), their Fig. 7 shown). The cause of the gap is not completely understood but is thought to represent a break point where larger planets can retain their primordial atmospheres while the smaller objects lose their atmospheres.

Analyses of the planets with the most accurately determined radii (i.e. those with the best characterised stars) reveal a non-homogeneous distribution in bulk planet properties. Whereas in our Solar System the distribution of planetary radii follow a power law, *Kepler* data show that there is structure in the distribution of exoplanet systems when evaluating the planet population at large. This is particularly interesting for small planets. While there are still questions over completeness at small radii, a deficit of planets at $\sim 1.8 R_e$ (Fig. 1) suggests physical processes (photo evaporation or core-powered mass loss) that separate the super-earth and sub-neptune populations - the so-called radius valley (Lundkvist et al, 2016; Fulton et al, 2017; Fulton and Petigura, 2018; Venturini et al, 2020; Izidoro et al, 2022; Ho and Van Eylen, 2023). The benefit of well-characterised host stars from asteroseismology when investigating the slope of the radius valley with increasing orbital distance was shown by Van Eylen et al (2018). However, although our current knowledge on exoplanet populations already provides exciting results challenging theories of planetary system formation and evolution, it is still heavily affected by observational biases. For example, the population of small planets represented in Figure 1 is dominated by planets with orbital periods of less than 80-100 days. There is a clear need to explore whether and how the radius valley extends to larger orbits. PLATO data will be excellent to analyze such trends at intermediate orbital distances.

Occurrence rates	Host stellar type	Reference
1% - 3%	Sun-like stars	Catanzarite and Shao (2011)
20% - 58% (34%)	FGK stars	Traub (2012)
31% - 64% (46%)	dwarf stars	Gaidos (2013)
7% - 15% (11%)	GK stars	Petigura et al (2013)
11% - 22%	GK stars	Batalha (2014)
0.8% - 2.5% (1.7%)	G stars	Foreman-Mackey et al (2014)
5.3% - 9.8% (6.4%)	FGK stars	Silburt et al (2015)
20% - 30%	Sun-like stars	Kopparapu et al (2018)
16% - 85% (37%)	Sun-like stars	Bryson et al (2021)
11% - 21% (14%)	FGK	Bergsten et al (2022)
<14.1%	FGK	Kunimoto and Matthews (2020)
28% - 95% (41%)	M dwarfs	Bonfils et al (2013)
9% - 28% (15%)	M dwarfs	Dressing and Charbonneau (2013)
24% - 60% (48%)	M dwarfs	Kopparapu et al (2013)

Table 1 Examples of published values for η_{Earth} occurrence rates from various radial velocity and transit surveys. The most likely value given in each respective publication is given in brackets.

To understand the complexity of processes affecting the evolution of planets further we need to assess planet (system) properties and correlate them to, e.g., stellar type, activity, and age, to name just a few of the relevant effects. The large number of correlations to investigate requires not only to increase the sample of planetary systems known, but also to determine their parameters with the best accuracy. As outlined above, it is essential thereby to close observational gaps, in particular for temperate and cool planets. It is the scope of PLATO to address these unknown population parameter ranges.

Figure 2 illustrates the anticipated detection range of PLATO with respect to the location of the HZ of solar-like and M dwarf host stars. Only planets with measured radii and masses are shown in the figure. A few characterised small planets in the HZ of cool M dwarf host stars are already known (e.g. the TRAPPIST-1 system ([Gillon et al 2017](#)) and more detections around cool stars are expected in the near future from NASA’s TESS mission. In addition, ESA’s CHEOPS (CHaracterising ExOPlanet Satellite) mission ([Benz et al, 2020](#)) can provide higher-precision radii for known exoplanets and therefore improve our knowledge of well-characterised bodies. However, these missions cover orbital distance ranges well below 1 AU.

Our current best knowledge on planet occurrence rates results from homogeneous re-analyses of *Kepler*/K2 data ([Kunimoto and Matthews, 2020](#); [Bryson et al, 2021](#)). Derived rates (number of planets per star) are in the range of a few to less than one percent, depending on size and orbital period. However, for small, long-period planets only upper limits can be given and uncertainties are large. Table 1 provides an overview of published values on the average number of Earth-like planets in the HZ. Uncertainties are large, whether they address solar-like or M dwarf host stars. For example, [Kunimoto and Matthews \(2020\)](#) provide upper limits from *Kepler* data reaching from few percent up to >40% for Earth-analogues (see their Figures 4 to 7). It is one of the prime goals of PLATO to derive an improved estimate of the occurrence rate of well-characterised small planets in the HZ of solar-like stars.

For cool host stars the exploration of orbital periods longer than 100 days allows us to characterise planets beyond the HZ and even beyond the respective ice lines in such systems. Access to these planets with well-known parameters will open a new door to comparative exo-planetology.

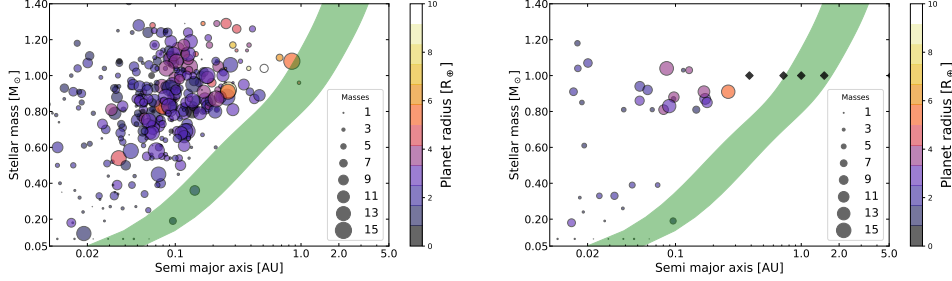


Fig. 2 Illustration of the PLATO objectives: populating the still quite empty HZ. Known small-low mass planets are shown in a stellar mass – orbital distance diagram, with symbol size and colour scaled with their masses and radii, respectively. The green band indicates the approximate position of the HZ, accounting for a potential early Mars or Venus in our Solar System. Left panel: planets $\leq 10R_{\text{Earth}}$ and $\leq 15M_{\text{Earth}}$; Right panel: same, but only showing planets with precision better than 5% and 10% in radius and mass, respectively. Black diamonds indicate Solar System telluric planets.

3.1.2 Expected PLATO Planet Detection Yield

To minimise the impact of biases on planet occurrence rates and derive precise analysis of planet population ensemble properties, we point out how important it is to use homogeneously analysed data sets. These data sets do not only concern planet parameters but also those of the underlying stellar populations. The PLATO Catalogue generated by the PLATO Consortium pipeline will provide such a data set for the community. The expected yield of new planets with characterised radii, masses, and ages is therefore a crucial objective for the mission.

Up to now, the expected yield of planet detections has been studied in the ESA Definition Study Report (hereafter called "Red Book", [ESA-SCI 2017](#)), by [Heller et al \(2022\)](#); [Matuszewski et al \(2023\)](#), and by forthcoming publications like [Cabrera et al. \(in prep.\)](#). We summarise these results here as the status at the current stage of the mission development and for comparison with future PLATO yield estimates by the community. For completion, there are also studies on the fraction of planets that will be impacted by background contaminants which are also valuable for properly determining the scope of follow-up efforts ([Santerne et al, 2013](#); [Bray et al, 2023](#)).

The detection efficiency of a transit survey like PLATO depends on several factors: the stellar target population observed and our good knowledge of it, the observing strategy, the actual planet occurrence rates, the geometrical transit probability, and the detection efficiency of the search methods implemented in the data analysis pipeline. In a second step, ground-based follow-up observations are essential, not only

for false positives filtering and confirmation of the detection, but also for the determination of planetary masses. For the purpose of PLATO detection yields presented here, we assume that all planets detected in the prime sample are suitable for radial velocity (RV) follow-up.

The target fields

For the Red Book estimates in 2017, simplifying assumptions had to be made regarding the stellar populations in PLATO target fields. At that time, studies to define optimised pointing directions for the mission were still ongoing and Gaia data were not yet available. A preliminary version of the PLATO Input Catalogue (hereafter PIC) was made, providing an initial check whether the required P1 and P5 stellar sample sizes could be met (see Section 6 for the requirements on P1-P5 samples, which are defined according to magnitude and signal-to-noise requirements). It was assumed that all stars in these samples were solar-like. Heller et al (2022) focused on PLATO's P1 sample, using as a stellar sample size both the requirement (15000) and the higher goal (20000) of target stars, again assuming all stars are solar-like. Today, we have significantly advanced the PIC based on Gaia data (Montalto et al, 2021). Studies on the best pointing directions have been completed (Nascimbeni et al, 2022) and the first pointing field is selected (see Section 7). Matuszewski et al (2023) and Cabrera et al. (in prep.) use the results of these most recent studies on PLATO's P1 and P5 samples.

Impact of observing strategy

The total planet detection yield depends on the number of target fields observed as well as the duration of continuous observations per field. The baseline for ESA operations of PLATO is an observing period with a total duration of 4 years. However, mission extensions are anticipated, subject to ESA review. The satellite is designed with consumables for 8.5 years of operations in total, permitting significant mission extensions. The goal to detect planets in the HZ of solar-like stars drives the observing strategy of PLATO and requires a minimum of two years continuous observation per field (with longer periods preferred). However, shorter periods have also been considered to estimate the full planet yield potential to study different kinds of systems. In the Red Book and in Heller et al (2022), a baseline observing scenario of two long instrument pointings of two years each ("2+2" scenario) is compared to a "3+1" scenario. The latter allows for one year with shorter observations of, e.g., 60 days duration each. Cabrera et al. consider also extended observation periods to study the benefits for long-period planet detection (see also below).

Assumed planet occurrence rates

This factor presents by far the largest uncertainty in planet yield estimates, in particular for small planets in the HZ. Even today the occurrence rate of terrestrial planets in the HZ of solar-like stars is poorly known, as discussed above. We have to wait for PLATO mission results before this parameter can be better constrained. For the purpose of predicting PLATO planet yields, occurrence rates are input parameters based either on observed data when available (e.g. for close-in planets) or on upper limits/estimates provided in the literature. Results from PLATO will confirm or reject these assumptions.

For the Red Book, planet occurrence rates were taken from [Fressin et al \(2013\)](#) based on *Kepler* data for all planets, except for small planets in the HZ which were not well constrained. To cover the wide range of uncertainty for HZ-planets (see [Table 1](#)), we assumed a planet occurrence rate of 40% as baseline, but also computed for extreme values such as 2% and 100%. [Heller et al \(2022\)](#) assumed planet occurrence rates spanning from 37% to 88% (from [Bryson et al, 2021](#)) for earths in the HZ. [Cabrera et al.](#) use the same assumptions as in the Red Book for consistency, but also study additional scenarios not shown here. [Matuszewski et al \(2023\)](#) use a very different approach. They address this unknown factor by using planet population models ([Emsenhuber et al, 2020, 2021](#)) to predict the number of planets formed up to the HZ.

Transit search algorithms

The efficiency of transit signal detection algorithms depends on several factors (see, e.g., [Christiansen et al, 2020](#)). It is relatively straightforward to quantify how the transit detection efficiency depends on the strength of the signal searched for. The signal depends on the astrophysical system (planet to star radius ratio, orbital parameters, etc.) and on the level of noise in the light curve (photon noise and systematic – red – noise). The noise budget is determined by the instrument design (e.g. aperture diameter, number of cameras observing the same target) and the target magnitude (see [Section 11](#)). In addition, variability in the light curves plays a crucial role, whether it is of instrumental origin (e.g. effects like random telegraphic pixels, tearing effect, non-stability of temperature or voltages, etc.) or resulting from the stellar properties (e.g. intrinsic variability, binarity). This variability can be partly corrected by light curve processing methods (e.g. for most systematic trends). The variability fraction that cannot be removed remains as residual noise budget in the processed light curves.

At the time of writing the Red Book, detailed instrument performance studies for PLATO as shown in [Section 11](#) were not available yet. The best existing analogy were *Kepler* data in combination with the available transit detection pipeline. It was therefore decided to account for all the above effects by choosing global detection efficiency factors based on the experience from *Kepler* ([Fressin et al, 2013](#)) and assuming that the PLATO mission noise requirements will be reached. Accordingly, for the P1 sample 100% detection efficiency was assumed for planets down to Earth size, based on the fact that targets are sufficiently bright and photon noise dominates over other noise sources for P1. This fraction (100%) was justified by i) estimating a signal-to-noise ratio of 13 (respectively 15) observing 2 (respectively 3) consecutive transits with depth 84 ppm (actually, with Sun-like limb darkening values, the transit depth of a planet with the size of the Earth is closer to 120 ppm, see e.g. [Heller 2019](#)) and ii) considering the detectability fraction originally in [Jenkins et al \(1996\)](#) that is discussed in [Fressin et al \(2013\)](#). Note that 34 ppm is the worst value of any P1 star, not the average noise. The median of the noise distribution (which was uncertain at that time) can be estimated around 20 ppm, producing a signal-to-noise ratio of 21. Note also that [Christiansen et al \(2016\)](#) would have revised the 100% fraction to 90%. However, this has a limited impact in the yield for Earth-sized planets in 1 year orbit when comparing to the uncertainty in the occurrence rate (ranging from 2% to 100%, see [Table 1](#)). Residual stellar intrinsic noise could still impact the detection efficiency for the smallest planets, but we anticipated that the well-chosen target stars in P1 would

not be dominated by this effect (by choosing quiet stars). For large planets (Neptune-sized planets and larger) in the fainter P5 sample, it is appropriate to assume 100% signal detection efficiency as well. Planets with 4 Earth radii produce a signal-to-noise ratio of 20 with just 1 transit around stars observed with 240 ppm, representing the worst of the P5 distribution (magnitude 13 observed at the edge of the field of view). Our assumed detection pipeline efficiency for P5 is reduced to 50% for planets with radii $< 2R_{Earth}$ in light curves with 80 ppm in 1 hour or better. Here the signal-to-noise ratio is 7 for 3 consecutive transits, which corresponds to 50% fraction as per [Jenkins et al \(1996\)](#), but see the discussion above. Again, here we took the worst noise as dimensioning case, which is conservative. For a P5 star with 50 ppm the signal-to-noise ratio with 2 transits is 9. Light curves with higher residual noise levels are not considered for our estimate of small planet yields, although larger planets would still be detectable.

[Heller et al \(2022\)](#) have improved this approach by applying their own transit signal detection algorithm (Transit Least Squares [Hippke and Heller, 2019](#)) to transits inserted into simulated PLATO light curves created by the PLATO Solar-like Light-curve Simulator (PSLS [Samadi et al, 2019](#)). This approach mimicked the response to the known instrumental noise sources of PLATO in a somewhat more realistic manner. [Matuszewski et al \(2023\)](#) and [Cabrera et al. \(in prep.\)](#) use an updated noise budget based on the currently known instrumental noise sources of PLATO and information from the recent PIC which was not yet available when the [Heller et al \(2022\)](#) study was performed.

Expected PLATO planet yields

Table 2 shows the resulting planetary transit event yields. For comparison, we summarise in column 2 the current knowledge of confirmed transiting planets in the literature. These planets result from ground-based detections as well as CoRoT, *Kepler*, TESS, and CHEOPS observations. Today, fewer than 1200 confirmed transiting planets around stars brighter than $V = 13$ mag are known, and none of them is a small planet in the HZ of a solar-like star. Fewer than 400 planets orbit stars brighter than $V = 11$ mag and are therefore suitable for effective RV follow-up.

PLATO is predicted to detect about 1200 transiting planets of all sizes in target stars with $V < 11$ mag, which would more than triple our current knowledge of well-characterised planets. These planets orbit stars which can be followed by RV ground-based spectroscopy to derive their masses. The number of planets followed will eventually be determined by the availability of telescope resources. For those planets included in the so-called “prime sample” (see Section 6), the PMC will provide sufficient ground-based resources by coordinating the follow-up community (Section 9). Planets detected in this sample will be the core of PLATO’s planetary systems catalogue. Other planets detected around bright stars will be followed-up by the community around the world and form a long-term legacy of PLATO.

For host stars of $V = 11$ to 13 mag the resulting planet properties from PLATO will be similar to the main part of the planet populations provided by the *Kepler* mission, hence masses will be available only for objects of special interest justifying dedicated follow-up campaigns (i.e. as for CoRoT-7b or Kepler-10b of $V = 11$ mag) or from Transit Time Variations (TTV) analysis. Nevertheless, these planets around

Samples	known transiting planets	2+2 scenario			
		Red Book	Heller	Cabrera	Matuszewski
all planets orbiting stars <13 mag in P1+P5 samples	1209	≈4600	n/a	6800-7100	4500-46000
all planets orbiting stars V<11 mag in P1+P5 samples	348	≈1200	n/a	1200-1350	1700-11000
planets <2 r _e in HZ orbiting P1+P5 stars <11 mag	0	6 - 280	11 - 34	0 - 95	≈45
Samples	known transiting planets	3+1 scenario			
		Red Book	Heller	Cabrera	Matuszewski
all planets orbiting stars <13 mag in P1+P5 samples	1209	≈11000	n/a	10100-10700	12000-68000
all planets orbiting stars V<11 mag in P1+P5 samples	348	≈2700	n/a	2200-2500	4000-42000
planets <2 r _e in HZ orbiting P1+P5 stars <11 mag	0	3-140	8-25	0 - 60	≈30

Table 2 Estimated PLATO planet yields. Red Book: ESA-SCI(2017)1; Heller: [Heller et al \(2022\)](#); Cabrera: Cabrera et al. in prep.; Matuszewski: [Matuszewski et al \(2023\)](#). 2+2 means 2 long pointings of 2 years duration; 3+1 means one 3-year observation followed by one year with six target fields for 60 days each, as in the Red Book. Known (confirmed) transiting planets are taken from the NASA exoplanet archive in Dec. 2022 for all planet radii and orbits.

fainter stars will be highly useful to study e.g. radius-orbit distributions, etc., just as for similar population analyses carried out with *Kepler* data. Accounting for an improved age calibration of stars from PLATO also for classical methods, we may be able to go beyond *Kepler* and study, e.g., the radius gap and orbital distance distributions as a function of stellar age also for this faint population. Considering planets of all sizes and all orbital periods, about 4600 planets (see Table 2) can be detected by PLATO around stars brighter than $V = 13$ mag by combining the P1 sample with the P5 sample. The PLATO planet yield in this magnitude range is therefore similar to the total planet yield in *Kepler*, but most *Kepler* planets orbit stars of $V > 14$ mag and are consequently difficult to characterise. Thus, at the bright end, where they are more suitable for further characterisation, the number of expected PLATO detections is higher than what has been achieved with *Kepler*. Indeed, although the somewhat smaller effective aperture of PLATO leads to higher noise levels at the same magnitude (see Section 11), this is compensated by the significantly wider field-of-view of PLATO. This is a consequence of PLATO’s modular camera approach and design.

The estimates by [Heller et al \(2022\)](#), as well as those by Cabrera et al. using more realistic stellar distributions and noise budget levels, are within the uncertainty ranges presented in the Red Book. The high end of numbers from [Matuszewski et al \(2023\)](#) stem from using a planet formation model for the assumed planet occurrence rate. The example shows the need for observational constraints to planet formation models.

The key planet sample of PLATO consists of small planets in the HZ of solar-like stars. The Red Book estimates a wide uncertainty range (6–280) for the yield of such planets around bright ($V < 11$ mag) stars, resulting from the large uncertainty in planet occurrence rates. These planets will mostly be suitable for RV follow-up, eventually depending on telescope time available, and form the main data product from PLATO for exoplanetary science. The study by [Heller et al \(2022\)](#) predicts a smaller number of

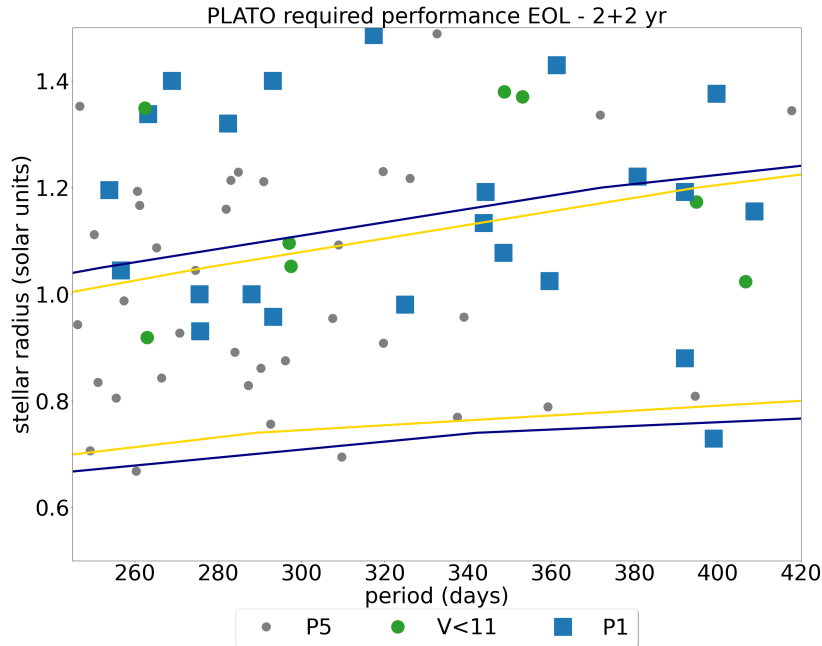


Fig. 3 Yield of planets with $<2 R_{\text{Earth}}$ in the HZ for the 2+2 scenario assuming 40% occurrence rate. We include two definitions for the HZ (the continuous lines): the optimistic (Kasting and Harman, 2013, blue) and the more conservative (Kopparapu et al, 2013, yellow). Symbols indicate the magnitude of host or target samples (P1 and P5) as indicated in the label.

planets in the HZ, but that is because these authors concentrated exclusively on Earth-sized planets ($< 1.5 R_{\text{Earth}}$) orbiting P1 stars, while the Red Book estimates consider planets of $< 2 R_{\text{Earth}}$ and stars with $V < 11$ mag in the P5 sample too. Cabrera et al. (in prep.) agree with previous results with a large uncertainty range, which is again associated with different assumptions for planet occurrence rates. Matuszewski et al (2023) use a planet synthesis model to estimate the expected planet occurrences. This approach results in much higher numbers of predicted planets, all other assumptions being the same. Figure 3 illustrates the expectations for PLATO for small planets in the HZ of solar-like stars for the 2+2 scenario addressed in the Red Book with current knowledge of the end-of-life (EOL) instrument performance of PLATO (see Section 11) using PIC version 1.1.0. The figure shows roughly 50 stars in the HZ which is in agreement with the prediction range of 0 to 95 in Table 2, performing simulations as described above.

In summary, at this point the predictions on the number of planets to be detected by PLATO are highly dependent on the respective assumed planet occurrence rates, in particular for temperate small planets. Hence, these predictions merely reflect our poor knowledge on planet formation efficiencies for small planets. Improving this situation with PLATO determined planet occurrence rates from a homogeneously analysed sample is a key science driver for PLATO.

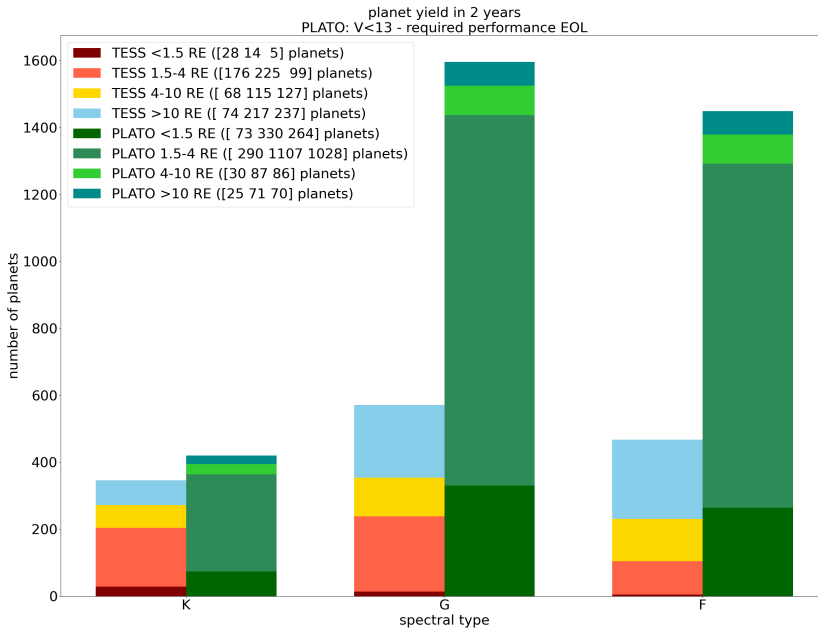
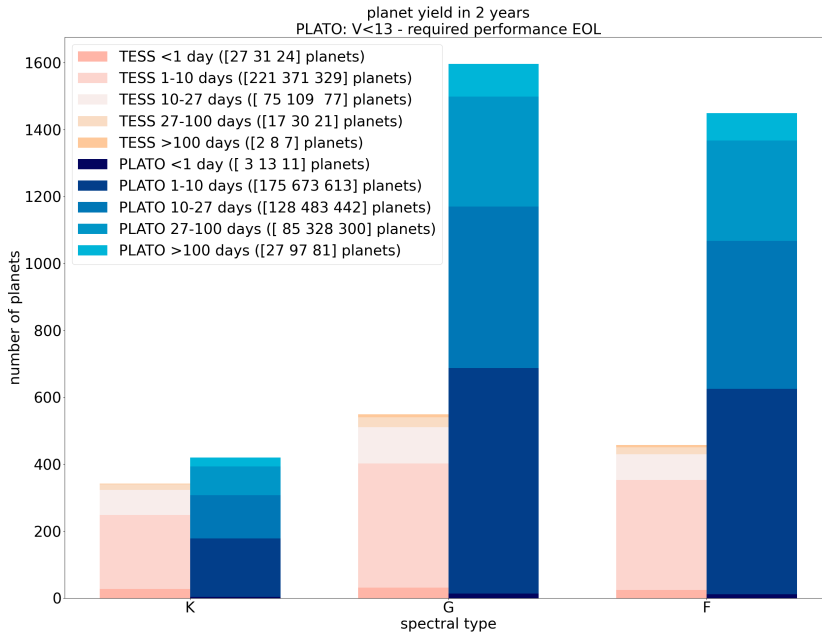


Fig. 4 Spectral type distribution for TESS Object of Interest (TOI) host stars compared with our expectations for PLATO. The number of planet detections for each spectral type (K, G, and F) is plotted as histogram. The values for TESS are taken from Guerrero et al (2021), their Fig. 7) and correspond to all magnitudes. False-positive TOIs have been removed. For PLATO we have taken the stellar population from the PIC (Montalto et al, 2021), which in its current version does not include M or A stars (hence we do not show any counts for these spectral types). We have considered the end-of-life (EOL) performance as per requirements, which is a conservative approach. We compare the nominal mission of TESS (2 years) with half of the nominal mission for PLATO (2 years). The PLATO results for the nominal mission (4 years) are about a factor of 2 higher (2+2 scenario in Table 2). Top: breakdown in orbital periods; Bottom: Breakdown in planetary sizes.

Comparison to TESS

To illustrate the expected impact from PLATO further, we compare PLATO with TESS choosing the validated TESS Objects of Interest (TOI) of the 2 year nominal mission (Guerrero et al, 2021). Figure 4 shows a comparison of TOIs orbiting FGK stars compared to PLATO expectations for a single field observed for 2 years. The predicted number of planets orbiting K stars detected by PLATO is only modestly increased compared to that expected from TESS. For G and F type stars, however, PLATO is expected to outnumber TESS results by factors 2-3 (G stars: 571/TESS and 1595/PLATO; F stars: 468/TESS and 1448/PLATO). It is interesting to compare the performance on temperate small planets of both missions for the same 2-year observing duration. Most TESS TOIs have orbits <10 days and only very few have orbits >27 days. PLATO planets will show a significantly larger fraction of longer periods from 27 days to >100 days. This is also the case for planets orbiting K stars, even though the total number of planets is comparable. Figure 4 shows how the PLATO efficiency to detect small planets around K, G, and F stars largely outnumbers TESS's performance when considering the same observing period.

In summary, comparing the TOI yield of TESS after 2 years of observations with the expectations for PLATO for the same time span, we clearly see the advantage of the PLATO mission design for detecting small and long-period planets. Note also that only a very small fraction of the TESS long-period planet discoveries will occur in the PLATO fields due to the different observing modes.

The expected planet yield for the TESS extended mission has been addressed in Kunimoto et al (2022), showing a factor 3 increased number of expected new detections for a total of 7 years of operations. This includes those to be discovered from analyses of the full-frame images, as well as the higher cadence of 2-minute TESS light curves. However, also for the TESS extended mission most planets are expected to have orbits up to about 30 days and will be larger than $4 R_{\text{Earth}}$ (their Fig. 6). Regarding small temperate planets in the HZ of solar-like stars (see Fig. 3) we compare PLATO's capacity with Fig. 5 in Kunimoto et al (2022): in their bin of $<2 R_{\text{Earth}}$ and orbital periods between 250 and 400 days, no planet detections are foreseen. This illustrates that we have to await the results from PLATO to fill this parameter range, which includes the range Earth would inhabit. It is the larger aperture (see also Section 11) and the observing strategy of PLATO that will allow breakthroughs in this parameter space.

Impact of extended observations

Recent studies addressed whether the detection efficiency of PLATO could be improved with adapted observing modes, e.g. by extending the duration of field pointings. As can be seen in Table 2, the total number of detected transits increases with increasing number of target fields observed, e.g. from about 4600 planets for 2+2 years of observations to about 11000 planets when observing one field for 3 years followed by 6 fields of 60 days each, as outlined in the Red Book. Obviously, most of the planets from the step-and-stare year are of short orbital period. At the same time, the number of small planets in the HZ decreases in the 3+1 scenario. There is a trade-off between observing fewer stars for longer versus more targets but with shorter-duration observations leading to fewer transits within a given observing time. Most interesting for

PLATO (after the success of TESS on short period planets) are scenarios with long observations of a target field to increase the chances for HZ planets. Clearly, the selection of the first target field and options to increase its observing duration will be part of choosing the optimal observing strategy for PLATO.

Figure 5 shows a prediction of the total number of planets discovered by PLATO as a function of the pointing duration. This prediction is done for a single pointing field (Cabrera et al. in prep.). Note that only planets with orbital periods up to 418 days were simulated (Fressin et al, 2013). Beyond this value we have no statistics, so longer-period planets will not add to the values in our analysis. Nevertheless, even if their transit probability is small, theoretical models predict that such long-period planets could be numerous (e.g. Matuszewski et al, 2023). Figure 5 shows that hot Jupiter detections saturate very quickly, within one year of observation duration. In this saturated regime, observing 2 independent fields for 2 years each would double the amount of planets detected, compared with the yield from one field targeted for 4 years. We note, however, that by the time of PLATO launch, the TESS mission already significantly increased our knowledge on these kind of hot gas giants and they may not be the main driver for selecting PLATO fields and their observing mode. The number of detected hot super earths saturates within 2 to 4 years of observations. Hence, once saturation is reached, additional detections can only be gained when changing the target field. In contrast to the hot planets, the number of temperate earths grows almost linearly with the pointing duration for up to 10 years. We clearly see the benefit in the detection yield of temperate planets when increasing the observing duration of a target field. This behaviour points towards increasing the observation of PLATO’s first target field beyond the nominal 2 years. However, before finally deciding on extended observing durations, we also have to consider the availability of resources for follow-up and the real in-flight instrument performance that might affect the expected detection efficiency. Once these factors are better known, a refined assessment on PLATO’s detection efficiencies as a function of target field observing duration can be made.

As outlined in Rauer et al (2014), we expect additional planet detections around, e.g., binary (multiple) stars (including circum-binary planets), subgiant and giant stars, as well as the potential for exo-comets, planetary moons, rings or Trojan planets. Estimates for the efficiency of PLATO detections on these targets are subject for future studies and beyond the scope of this review. This applies also for planet detections made via, e.g., Transiting Time Variations (TTV) analyses or reflected light observations. Here, we only recall these extra methods and targets as a reference for the many new discoveries expected from the PLATO mission.

In summary, although recent studies spent some effort to refine the expected transit detection efficiency in PLATO light curves, the largest unknown remains η_{Earth} , the unknown planet occurrence rate of small HZ planets. Current planet yields predict the detection of a few up to a bit more than a hundred small planets in the HZ of solar-like stars, depending on the value of η_{Earth} . These planets are suitable for radial-velocity follow-up (depending on telescopes availability) and will provide accurate radii, masses, and ages. PLATO data will therefore significantly improve our knowledge of planet statistics of well characterised planets, especially those small in size and with long orbital period - or - in the HZ of their solar-like host.

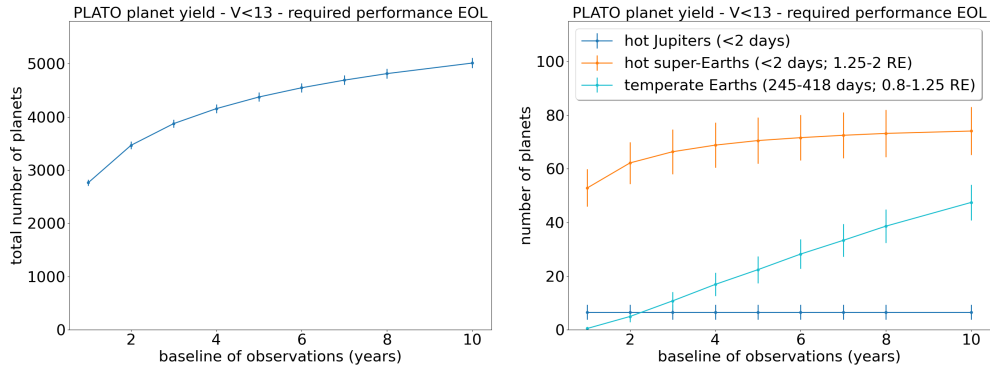


Fig. 5 The left figure shows a prediction of the total number of planets that could be discovered by PLATO as a function of the duration of the observation run. This is done for a single pointing field following Cabrera et al. in prep. The figure presents together planets of all sizes, all orbital periods, around stars brighter than magnitude 13. The right figure shows the same for hot Jupiter planets (defined as planets with 6 to $22 R_{\text{Earth}}$ and orbital period < 2 days), hot super-Earths (defined as planets with 1.25 to $2 R_{\text{Earth}}$ and orbital period < 2 days), and temperate Earths (defined as planets with 0.8 to $1.25 R_{\text{Earth}}$ and orbital period between 245 and 418 days). The vertical lines represent the expected uncertainty in the number of planets.

3.2 Planet Characterisation

3.2.1 Brief summary of state of the art

PLATO aims to assemble the properties of statistically-significant ensembles of planets, more so than to focus on individual planets. Clear trends and potential clustering in planetary properties will only become apparent once we manage to reduce error bars for the key parameters and can access a large and homogeneously analysed catalogue of planets, such as PLATO will provide.

Derived planetary mass-radius relationships and mean densities are important indicators of the nature of detected planets. To first order, the mean density-mass relationship can be used as an indicator for planet classification: [Hatzes and Rauer \(2015\)](#) use it to reveal the turnover from small terrestrial and Neptune-like planets to gas giant planets and further for the transition to brown dwarfs. More frequently mass-radius diagrams are used to obtain a first indication on the nature of planets (starting with, e.g., [Seager et al \(2007\)](#); [Adams et al \(2008\)](#); [Wagner et al \(2011\)](#), and many since). See [Otegi et al \(2020\)](#) for a recent study of transiting planets up to $120 M_{\text{Earth}}$. Even though a unique one-to-one mapping to particular planetary internal structures and compositions is difficult just based on radius and mass data alone due to the inherent degeneracy of the problem (see, e.g., [Valencia et al 2007](#); [Rogers and Seager 2010](#); [Dorn et al 2015](#)), these data do provide important constraints to formation models when ensemble properties become apparent.

The situation on deriving internal structure and composition of planets improves when simplifying assumptions can be made like elemental abundances taken from host stars (e.g. [Dorn et al 2017](#); [Brugger et al 2017](#)) or information from our knowledge of

planets in the Solar System. Although this greatly reduces the various degeneracies, it is clear that many assumptions currently made are over-simplified. For example, the host star photospheric composition today may not reflect that of its planets (Plotnykov and Valencia, 2020) as additional processes including devolatilization trends (Wang et al, 2019) or diverse impact scenarios can alter the planet’s composition, whereas material falling into the star might affect the measured stellar composition. Therefore, planet characterisation models should not rely only on stellar constraints, in view of large error bars that prevent a definite conclusion. While degeneracies can likely never be completely resolved, they can be reduced when the primary parameters are precisely measured (as done with PLATO) and when combined with additional data, in particular providing information on the planetary atmospheres (e.g. with JWST, ARIEL, ELT, LUVOIR/HABEX (now the Habitable World Observatory, HWO), LIFE). A key factor will be to increase the available statistical sample of well-characterised small planets.

A recent example of planet characterisation by combining density measurements with further atmospheric data are TRAPPIST-1 b and c. Emission photometry of planet b shows a bare rock surface with apparently no atmosphere (Greene et al, 2023), while planet c discards a thick CO₂ atmosphere (Zieba et al, 2023). Acuña et al (2023) use these measurements to constrain the Fe-to-Si ratio of TRAPPIST-1 b based only on the density of the planet, without making assumptions on the composition of the star, by performing a retrieval on the mass and radius using a two-layer interior structure model. PLATO will provide a wealth of data to further follow such approaches to planet characterisation.

The case is particularly challenging when considering planets in between predominantly gaseous or rocky nature, the so-called mini-neptunes (or ‘mini gas planets’, hence small gaseous planets) and earths to super-earths-like planets. If one assumes for simplicity that such planets would consist of four distinct layers (i.e. an iron core, a silicate layer, a water/ice layer and an atmosphere), several combinations of these layers of different inherent densities or mass fractions can result in the same mean planet density. Early studies of super-earths with little or no hydrogen atmosphere showed that planet radius measurements to better than 5% together with masses determined to better than 10%, such as PLATO will provide, would allow us to distinguish between an icy or rocky composition (e.g. Valencia et al 2007). Recent studies with more advanced interior models, allowing for additional phases and internal layers in the interior, confirmed these requirements on radius and mass precision when constraining the planets interior structure (Otegi et al, 2020; Dorn and Lichtenberg, 2021; Baumeister and Tosi, 2023).

Furthermore, depending on the internal energy and in turn on the age of a planet, large portions of the silicate layer may be molten, leading to water being dissolved in the magma ocean rather than a separation of the two layers, which would directly influence the planet’s observed density (Dorn and Lichtenberg, 2021). The internal energy further determines if the metallic core can efficiently separate from the mantle, which also influences the measured planet radius and hence density (Elkins-Tanton and Seager, 2008; Lichtenberg, 2021). The precise measurement of the age of the planets

will help to assess the likelihood of different endmember scenarios, since cooling and differentiation are strongly time-dependent processes.

The planetary bulk composition and evolving interior structure are also important for assessing the possible evolutionary pathways of such planets (especially for low-mass, rocky planets) and their surface processes. Studies focusing on Earth-like compositions have already shown that key processes such as plate tectonics, volcanic activity or magnetic field generation (all directly linked also to the atmospheric evolution) strongly depend on planetary mass, metallic core size and surface temperature (Wagner et al, 2011, 2012; Valencia et al, 2007; Kite et al, 2009; Ortenzi et al, 2020; Dorn et al, 2018; Bonati et al, 2021; Kislyakova and Noack, 2020; Baumeister and Tosi, 2023). The atmospheric evolution is further influenced by the orbital distance of the planets, another observable of PLATO, leading to a bifurcation in atmospheric evolution (Hamano et al, 2013) and erosion efficiency (Godolt et al, 2019; Moore and Cowan, 2020), which can furthermore influence the measured planetary radius.

Apart from precise mass and radius measurements alone, constraints on planet composition and internal structure will be improved significantly when combined with additional observables, e.g. atmospheres as discussed already above. However, there are also additional observables from PLATO data alone, such as the fluid Love number for giant planets near the Roche limit (Correia, 2014; Kellermann et al, 2018; Padovan et al, 2018; Akisanmi et al, 2019; Csizmadia et al, 2019; Hellard et al, 2019, 2020; Baumeister and Tosi, 2023), stellar parameters (e.g. heavy element content, activity), and especially age (e.g. to compare with timescales of atmospheric loss processes). In particular the correlation of planetary parameters with ages has the potential to provide significant new insights into the development of planets. For example, for warm Jupiters PLATO ages will help to break the degeneracy with respect to their heavy element component (Müller and Helled, 2023). How planetary properties correlate with age (e.g. due to contraction, atmosphere loss, tidal interaction, etc.) can be studied once ages are available in sufficient numbers and accuracy from PLATO. Correlating terrestrial planet properties with age is entering a new area of understanding planets similar to our own. PLATO ages will be an important element in the full characterisation of these planets with JWST as well as future HWO and LIFE type missions.

Unfortunately, our current knowledge on mass-radius and planetary densities is still significantly observationally biased. Concerning close-in planets, we expect many new ultra-short-period planets and hot gas giants to be detected using NASA’s TESS mission (see Section 3.1.2) and characterised with follow-up, including atmosphere studies by JWST and ARIEL. For those planets in the PLATO fields, additional data such as TTVs, albedos, phase curves, and high accuracy radii and ages from PLATO will complement TESS, JWST and ARIEL data.

How planet densities (hence planet nature) correlate with orbital distance (orbital period) will be among the key findings of PLATO. Fig. 6 shows our current knowledge of planets with known mean densities. Most of the planets with precise mass and radius, hence density, are in the gas giant regime (Fig. 6, left). When considering planets with orbital periods beyond 80 days, however, only few gas giants with precise densities are known to date (Fig. 6, right). The left branch of this diagram, where

terrestrial planets and mini-Neptunes are located, is empty to date for periods beyond 80 days, except for the planets in our Solar System. How small planets are distributed at intermediate orbital distances around solar like stars will be revealed by PLATO. These results will form a major legacy of the mission. Such observations will also show whether terrestrial planets are present beyond the ice line in M dwarf planetary systems, which forms another 'unknown' to be revealed by PLATO.

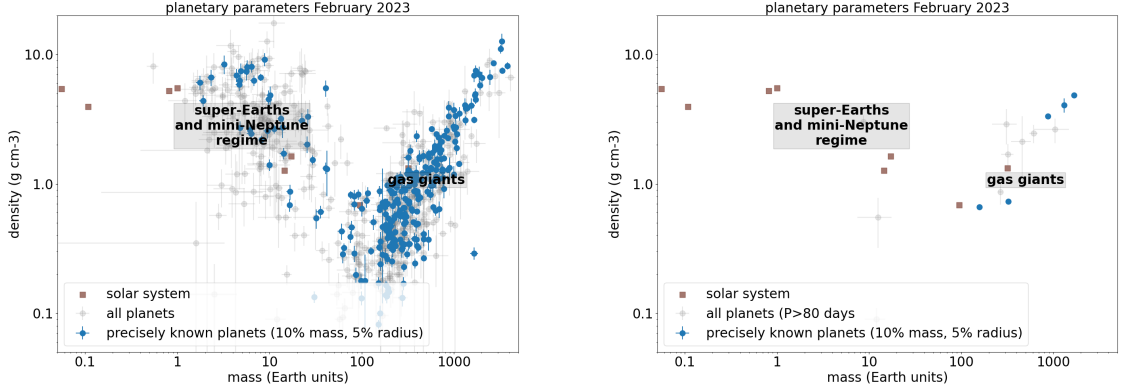


Fig. 6 Known planetary mean densities versus mass (status February 2023). Grey symbols indicate confirmed planets, blue symbols show planets with precisely known parameters. Brown squares indicate Solar System planets. Left: all planets; Right: only planets with orbital period >80 days.

Understanding the nature of exoplanets is a big puzzle to be resolved, requiring the combination of all available observational information. The role of PLATO in solving this puzzle is in the provision of exploring accurate planet parameters (including the ages) in a homogeneously processed sample of objects.

3.2.2 Expected planetary radius accuracy

PLATO requirements for planetary radius and mass are defined for a reference Earth-Sun scenario: an Earth-sized planet orbiting a G0V star as bright as $V = 11$ mag at 1 AU (see Section 8). The required planet radius accuracy is 5% for this reference case. For the brightest targets (≤ 10 mag) a radius with 3% accuracy should be achieved. This corresponds to an accuracy for R_{planet}/R_{star} of 2%. We note that these requirements are in many ways the most difficult case and larger planets and/or smaller host stars will provide even better precisions, depending on respective signal-to-noise levels and stellar models.

For now, we assume that the required stellar radius accuracy of 2% is reached (see Section 4.4 for a discussion on PLATO's capacity to deduce stellar parameters). Hence the precisions on planetary radii discussed here provide *accurate* radii in terms of our terminology. Planetary radii are then obtained by fitting the shape of observed transit events in the processed light curves. Residual noise sources (instrumental or stellar)

therefore could affect the achievable precision. In Section 11 we show that PLATO light curves will be dominated by white noise for stars between $V = 8$ and 12 mag. Hence, PLATO instrumental noise effects are minimal for the P1 sample and even for the bright end of the P5 sample. What remains is a potential impact by residual stellar variability in the light curves. In a first step we neglect such an impact. See the literature overview of detailed studies made at the end of this section, showing that such an assumption is justified for the bright samples.

Figure 7 (top left) shows that for a $V = 10$ mag Sun-like host star, a radius ratio precision of 2% can be reached for an Earth-sized planet with 3 transits. Better precision is reached for larger planets and brighter host stars, as expected. The top right shows that a planet radius precision of 3% can be obtained down to $V = 10.5$ mag and increasing to a radius error of 5% at $V = 11.6$ mag. These results were obtained analytically (15) and agree well with the detailed numerical models (Morris et al, 2020; Csizmadia et al, 2023). The results confirm that the PLATO design is in agreement with its respective science requirements. To give an estimate accounting for possible catastrophic events during the mission, the impact of the loss of two cameras has been studied. In such a case the radius precision would decrease by about 10% to 5.5% precision. In the bottom left the dependence on observing duration, hence the number of detected transits is shown. As expected the radius error decreases with more transits observed, e.g. due to longer target field observation but also for planets with short orbital periods. Hence, very precise radii are expected for hot terrestrial exoplanets around solar-like stars. The lower right of Figure 7 shows the expected precision for an Earth-sized planet orbiting different stellar types.

For a more detailed analysis of the expected resulting planet parameter precision additional effects need to be accounted for. These are, however, rather independent of the instrument design but instead depend on the quality of data reduction and analysis methods. At least three factors need to be considered: residual red noise effects, stellar limb darkening, and the knowledge of relevant orbital parameters.

The most challenging problem is caused by the detected baseline stellar flux which is rarely constant in time. It is changing because of instrumental effects, cosmic ray impacts, straylight changes, variable contaminating sources in the aperture (e.g. a variable star) and because of astrophysical reasons intrinsic to the star: stellar variability and activity, etc. All of these effects cause correlated, or so-called red, noise effects in the light curves. The issue of residual red noise in the stellar baseline and in-transit data points was investigated by, e.g. Barros et al (2020), Morris et al (2020), and Csizmadia et al (2023). Morris et al (2020) utilised SOHO solar images to simulate transits to be modelled. Barros et al (2020) tested the applicability of Gaussian Processes. Csizmadia et al (2023) assessed the performance of wavelets to model the stellar and instrumental noise. These authors used *Kepler* Q1 short cadence light curves with injected transits for different planetary and stellar parameters to mimic the red noise effects. They modelled the light curves with wavelets and analysed the results with retrieval methods. Their findings show that above a certain signal-to-noise

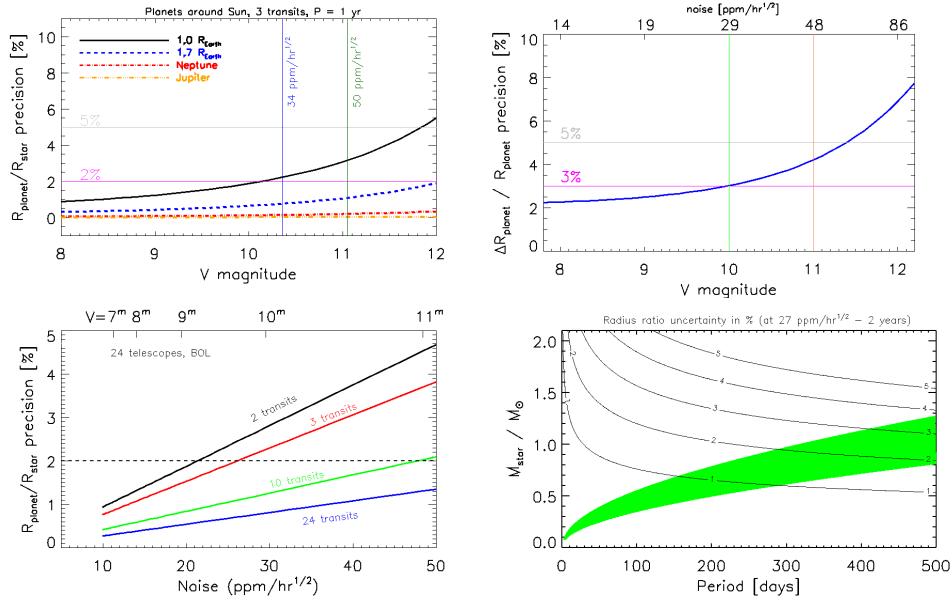


Fig. 7 Simulated radius precision for planets orbiting a Sun-like star. Top left: radius ratio precision for 3 observed transits and different planet types. Top right: The “Earth-around-a-Sun” case for 3 transits. The desired radius accuracies are noted, where we assumed that the stellar radius - independently of the magnitude of the host star - is known to 2%. Bottom left: radius ratio precision for the “Earth-Sun” case and different number of transits, where a larger number of transits can be reached at shorter orbital periods when the duration of the pointing is unchanged. Bottom right: Earth-sized planets transiting different host stars. The approximate position of the HZ is indicated in green. The stellar radius was estimated via $R_{\text{star}} = R_{\odot} (M_{\text{star}}/M_{\odot})^{0.95}$. The number of transits depends on the orbital period, where we assumed that all transits are detected during a 2 year long pointing.

ratio (SNR), preferentially $\text{SNR} > 45^1$, the planet radius as well as other parameters can be retrieved with highest accuracy, even for the difficult Earth-Sun reference case, as long as the stellar radius is known to better than 3% (we recall that detection is possible already at lower SNR – e.g. 7 to 10 –, but provides larger uncertainties in the planetary parameters). Thus, combined Gaussian processes and a wavelet technique to model the noise provide appropriate tools to obtain the radius ratio with the desired precision and remove the red noise effects while solving the stitching of PLATO light curves. Further analyses of respective data processing methods are ongoing in the PMC to support the present conclusion that PLATO will deliver the planetary radii with an accuracy better than 5% for the aforementioned baseline scenario.

¹In their work the signal-to-noise ratio was defined as: $\text{SNR} \equiv (R_{\text{planet}}/R_{\text{star}})^2 / \sqrt{\sigma_w^2 + \sigma_r^2} \times \sqrt{N_{\text{transit}} D / t_{\text{exp}}}$, where N_{transit} is the number of observed transits, D the transit duration, t_{exp} the exposure time, and σ_w and σ_r the white-noise level and the red noise per data point.

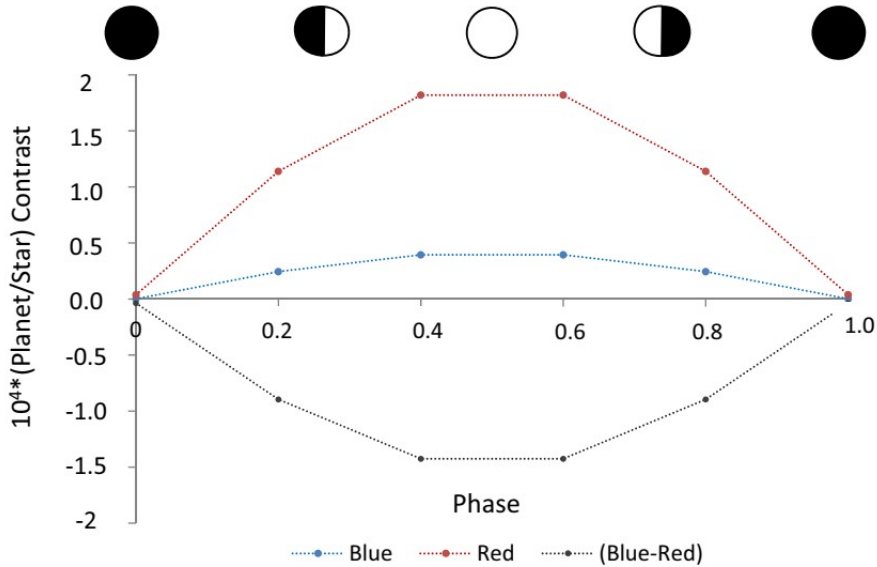


Fig. 8 The phase curve of the contrast (Planet/Star) enhanced by a factor 10^4 as would be observed by the PLATO fast cameras with their “red” and “blue” filters for a hypothetical, nearby (10 pc) Ultra-Hot-Jupiter, assuming the planetary properties of WASP-103b. Data begins at the nightside during conjunction and shows 6 equidistant points. Figure adapted from Grenfell et al (2020).

3.3 Constraints on planetary atmospheres

Although the PLATO mission is not primarily designed to study exoplanetary atmospheres, its light curves can nevertheless provide relevant information on atmospheric properties. The amplitude and shape of white-light orbital phase curves, for example, can provide a first constraint on atmospheric meridional transport, mass and albedo. Basic colour information (“red” and “blue”) from the broadband filters on the PLATO fast cameras (with fast read-out cadence) can constrain the bulk atmospheric composition from estimating the Rayleigh spectral absorption feature. Also, PLATO’s prime data products, namely planetary radius, mass, and age, are crucial for retrieval and interpretation of atmospheric properties from spectroscopic data.

Grenfell et al (2020) found that planetary geometric albedos, as well as moderate-to-strong Rayleigh extinction can be detected for targets up to 25-100 pc distance based on simulated SNR for observations of nearby hot and ultra-hot Jupiters (UHJs) with the PLATO fast cameras. Their work suggests that initial constraints can be deduced from UHJ phase curve amplitudes for nearby targets closer than 25 pc, although this will be challenging. To illustrate this, Figure 8 shows a simulated phase curve for a hypothetical close-by (10 pc away) UHJ as would be observed by the PLATO fast cameras. From phase curve data on UHJs as shown in Figure 8 one can infer the dayside and nightside temperatures and thus the energy balance and intrinsic heat flow as well as planetary albedos, which are very important planet properties. Given that at present there are about only two dozen planets with observed phase curves, any one that PLATO can add will be valuable.

Regarding warm sub-Neptunes and Super-Earths, the Grenfell et al (2020) study suggested that basic atmospheric bulk compositions and haze properties in the upper atmosphere can be distinguished for some nearby (<10 pc) favoured targets, although this will likely be a challenging task. Carrión-González et al (2020, 2021) point out that having prior information from PLATO on the planetary radius is an important input for model studies constraining atmospheric clouds and composition from direct imaging, since being able to fix the radius helps to disentangle degeneracies between planet radius, cloud layers and major atmospheric absorbers when studying planets in reflected light. Turbet et al (2019); Schlecker et al (2023) suggest that PLATO measurements of planetary radii for hot Super-Earths with giant steam atmospheres will allow us to pinpoint and characterise runaway greenhouse regimes with strongly inflated atmospheres (see also Boukrouche et al, 2021). Ortenzi et al (2020) offer a way to distinguish lighter, more extended Super-Earth atmospheres (outgassed by more reducing mantles (Lichtenberg, 2021)) from more compact atmospheres outgassed by more oxidised mantles from the high-precision PLATO measurements of the planetary radius.

Clearly, PLATO data alone are not sufficient to resolve the complex optical properties of planetary atmospheres. They can, however, serve as a guide to trigger follow-up observations with spectroscopic instruments. The full benefit of a large sample of exoplanets with well-known PLATO ages will become apparent when spectra of their atmospheres become available. As such, PLATO will provide constraints on the evolution of gaseous planets in combination with missions featuring spectroscopic capabilities such as JWST and ARIEL. In case of lucky detections of transiting planets which are sufficiently close to us and on sufficiently wide orbits can be made, they would even provide the opportunity to compare their transmission spectra to direct imaging spectroscopy. In the somewhat more distant future, well characterised terrestrial exoplanets with accurate age determinations will allow to obtain observable constraints on the typical evolution of such planets (Lichtenberg et al, 2019; Lichtenberg and Clement, 2022). We will then be able to compare the terrestrial Solar System planets and their evolutions with a major sample of terrestrial exoplanets. While this goal can only be fully achieved by combining results from various future space missions, PLATO will provide a significant piece to this puzzle.

3.4 Constraints on planet formation and evolution

A key science objective of PLATO is to further our understanding of how planets and planetary systems form and evolve. It was recognised at the inception of the mission concept that complementary theoretical modelling efforts in planet formation and evolution will be essential to achieving this goal. The large and well-characterised population of planets in diverse Galactic environments to be obtained by PLATO, with precise measurements of radius, mass, density, age and host star properties such as metallicity and stellar type, extending out to orbital periods > 80 – 100 days, will provide the most comprehensive testing ground for the modelling of formation and evolution processes to date. In particular, the discovery of Earth-like planets would help our understanding of how terrestrial planets form.

State-of-the-art global models of planet formation are in continuous development and already account for many of the important processes involved in the building and shaping of planetary systems during their first 10-100 Myr, leading to synthetic planet populations that can be compared with planet population data (Benz et al, 2014; Drazkowska et al, 2023).

These processes include protoplanetary disc evolution (Lesur et al, 2023), the growth of planetary embryos through pebbles and/or planetesimals (Morbidelli et al, 2012; Johansen and Lambrechts, 2017), the accretion of gas onto forming planets (e.g. Cimerman et al, 2017; Lambrechts et al, 2019a; Nelson et al, 2023), and disc-driven migration (Kley and Nelson, 2012). Although much progress has been made in the past decade on these topics, some key physical mechanisms and their relative importance remain poorly understood. For example, a variable mass budget available in pebbles could regulate the formation and migration of either Earth-like or super-Earth-like planets in the terrestrial zone (Lambrechts et al, 2019b). Disc evolution in turn regulates migration rates and resonant-trapping of planet systems (Kajtazi et al, 2023; Batygin and Petit, 2023; Huang and Ormel, 2023). Finally, the composition of planets is a complex product of the full planetary growth process, starting from the growth and drift of primordial dust grains (e.g. Johansen et al, 2021; Schneider and Bitsch, 2021). Models also exist of processes that act on longer timescales, such as tidal evolution, core-powered and photoevaporative gas envelope loss, and the role of stellar cluster membership in shaping planetary systems (e.g. Papaloizou, 2011; Wu et al, 2007; Rogers et al, 2021; Li et al, 2023).

Progress will be made through comparison between these models and the PLATO-observed planet population which will then shed light on the relative importance of these processes, and will point to areas where model improvements are required, either through the inclusion of hitherto neglected physical effects or through improved understanding and modelling of fundamental planet formation processes (e.g. Coleman and Nelson, 2016; Bitsch et al, 2019; Emsenhuber et al, 2021; Izidoro et al, 2021; Qiao et al, 2023). In addition to examining the global planet population, the models will explore important correlations in the data, for example between host star metallicity or stellar type and the emerging architectures of planetary systems, shedding additional light on the factors that control planet formation (Liu et al, 2019).

PLATO will not only find planets around single main-sequence stars, but is expected to find substantial numbers of more exotic planets, such as circumbinary planets, that provide more extreme environments that can act as stringent tests of planet formation theories. For example, allowing discrimination between in situ scenarios and those that require migration (e.g. Pierens et al, 2021). Development of population synthesis models of these types of systems (Coleman et al, 2023) will allow comparison with PLATO data, constraining theories of planet formation in diverse environments.

4 Stellar Science

4.1 State of the art of seismic stellar characterisation

The characterisation of exoplanets highly depends on the characterisation of their host stars. The more precise and unbiased the characterisation of the latter is, the more accurate will be the characterisation of the planets they host. Stellar properties such as mass or age are most often derived from stellar modelling constrained by classical data. Yet seismic information, whenever available, helps tremendously to improve such modelling because it provides direct information from the deep stellar interior.

Starting with the Sun, two decades of observations have demonstrated that solar-like seismic constraints are the most powerful tool to derive precise stellar masses, radii, densities, and ages, provided that high-quality seismic parameters are available (for reviews see [Chaplin et al, 2013](#); [Christensen-Dalsgaard, 2018](#); [García and Ballot, 2019](#); [Serenelli et al, 2021](#)). However, this requires short-cadence (less than 1 min for dwarfs and subgiants), ultra-high photometric precision (at the level of parts-per-million or ppm) and nearly-uninterrupted long-duration (from months to years) monitoring as best provided by space observations.

Beyond the precise characterisation of specific stars, seismology allows us to probe the physical interiors. In this way, it allows the identification of shortcomings in stellar modelling, to guide the theoretical developments for improvements in the physical description and then validate those improvements. This in turn leads to a more accurate characterisation of *all* stars – in particular their age-dating, not only for those with seismic features. Compared to classical modelling without asteroseismology, higher accuracy is achieved for the properties and parameters measured for a given star from the use of seismic constraints and more realistic stellar modelling ([Silva Aguirre et al, 2017](#); [Nsamba et al, 2018a](#)) or through the use of seismically calibrated relationships such as gyrochronology ([Angus et al, 2015](#); [van Saders et al, 2016](#); [Hall et al, 2021](#), and references therein) and abundance ratios – age relations ([Nissen et al, 2017](#); [Morel et al, 2021](#)).

4.1.1 Ultra-precise photometric seismology: the space era

After the proof of concept space missions – either by accident (WIRE: [Buzasi et al, 2005](#)) or dedicated (MOST: ([Walker et al, 2003](#)) – the French-led CoRoT satellite (2006 – 2009; [Baglin et al, 2006](#); [Auvergne et al, 2009](#)) really opened the space-seismic era with the detection of solar-like oscillations in about twelve bright dwarfs and subgiants ([Michel et al, 2008](#)) and thousands of red-giant stars ([de Ridder et al, 2009](#); [Miglio et al, 2013](#)). This has led to the first detailed asteroseismic studies of solar-like oscillations in main-sequence stars, as well as to the new field of red giant seismology (e.g. [Baglin, 2016](#)).

The NASA space mission *Kepler* (2009 – 2018; [Borucki et al, 2010](#)) monitored more than 150000 main sequence stars, of which about 2600 dwarfs and subgiants were observed for one month in short-cadence mode (58.85 sec). These measurements turned detailed seismic investigations into a reality for large samples of dwarfs ([Gilliland et al, 2010](#); [Chaplin et al, 2014](#)). Overall, the nominal *Kepler* mission led to the detection

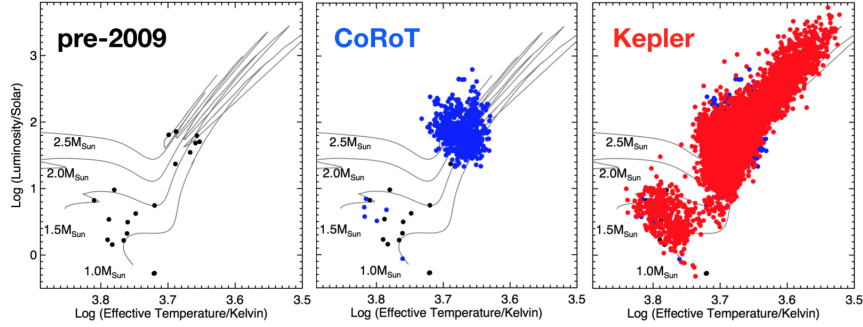


Fig. 9 Stars with detected solar-like oscillation from ground-based instruments prior to the seismic space era (left) and from the space missions CoRoT (middle) and *Kepler* (right). Figure reproduced from (Huber and Zwintz, 2020)

of solar-like oscillations for more than 600 dwarfs and subgiants. Most of them were observed for only one month while about 150 stars were observed for longer, up to 4 years. The so-called *Kepler* Legacy sample of 66 dwarfs revealed the major power of asteroseismology of Sun-like stars (Lund et al, 2017; Silva Aguirre et al, 2017). A few dozen of them host planets and these are now among the most precisely characterised host stars (Huber et al, 2013; Silva Aguirre et al, 2015; Bétrisey et al, 2022; Hatt et al, 2023).

The NASA TESS space mission launched in 2018 (Ricker et al, 2015) is currently in operation. It provides lower-quality photometry than the *Kepler* mission but focuses on bright stars ($5 < V < 11$) and carries out a nearly-all-sky survey. The observing time is short, 27 days for most stars, but it reaches up to 352 days in the continuous viewing zone. During its 2 year nominal mission, TESS had a short-cadence mode of 2 min. During the first extended mission an additional 20 second mode was operational, which is better suited for seismic analyses as advocated by Huber et al (2022). As demonstrated by the first results, TESS is capable of detecting solar-like oscillations with high amplitudes and therefore suitable to study seismology of subgiants and red giants (e.g., Campante et al, 2019; Huber and Zwintz, 2020; Chontos et al, 2021).

Figure 9 shows samples of stars covering the main sequence to the red-giant branch for which solar-like oscillations have been detected at three epochs marking the major progress of the space revolution in asteroseismology. Progress went from a handful of stars with solar-like oscillations detected with ground-based instruments to hundreds of detections from CoRoT focused on evolved stars and thousands of them resulting from the *Kepler* (and now TESS) space missions. The PLATO P1 and P5 samples will further increase the samples appreciably compared to those shown in Fig. 9, particularly for dwarfs and subgiants. With its 25 sec cadence during the entire long pointings, PLATO will not only deliver new detections of solar-like oscillations in thousands of stars, but the precision of the oscillation frequencies will also be unprecedented for such a large homogeneously assembled and analysed ensemble of dwarfs and subgiants, among which will be thousands of exoplanet host candidates.

4.1.2 Ultra-precise seismic stellar characterisation with *Kepler*

The *Kepler* seismic observations have motivated a large number of investigations over the past years to make the best use of seismic data to characterise stars. Here, we present some lessons of interest for the PLATO mission that one can draw from those studies.

The detection of solar-like oscillations, the quality of the measured seismic parameters, and the accuracy with which seismic stellar characterisation is obtained all depend on the SNR, the cadence, and the observation baseline for each star. The SNR depends not only on the instrumental observational noise and the apparent magnitude of the star but also on the type of star. Hence, depending on the quality of the observations and the type of star, we have different levels of stellar characterisation. PLATO is designed and optimally suited to perform asteroseismology of sun-like stars. However, we learned from the *Kepler* data that, for K dwarfs and M-type stars, either the oscillation amplitudes are too low for detection or the stars do not oscillate at all (Rodríguez-López et al, 2015; Rodríguez-López, 2019). Even for F to G-type dwarfs, it is thought that the impact of strong surface magnetic activity on envelope turbulent convection can cause a significant decrease of the oscillation amplitudes, which can hamper their detection (García et al, 2010; Chaplin et al, 2011b; Kiefer et al, 2017; Santos et al, 2021). Some other causes of non-detection are also possible, such as metallicity effects and binarity (Samadi et al, 2010; Karoff et al, 2018; Mathur et al, 2019). It is not yet clear whether TESS in its 20 second cadence mode with its limited photometric quality can lead to advances on these topics, but PLATO with its 25 second cadence mode and high photometric quality will bring new insights. On the hot side, late F-type stars have larger mode linewidths than G-type stars, causing larger uncertainties in their seismic measurements. These translate into larger statistical uncertainties for their stellar parameters (Appourchaux et al, 2012; Compton et al, 2019). However, those stars with their large radii (larger than 1.2 solar radius) and high temperatures are not the main priority for PLATO’s exoplanet search and characterisation. Actually the P1 sample is truncated at temperatures on the hot side, such that one still encounters solar-like oscillators. We therefore focus hereafter on the case of late F, G, and early K-type dwarfs, and subgiants.

Averaged seismic indices and scaling relations

When the SNR is low and/or the observation time duration is short (one month or so), the solar-like oscillations are detected mainly as a power excess in a power spectrum. One then takes the regularity of the frequency pattern to determine a first average seismic quantity, namely the mean large frequency separation, $\Delta\nu$, that scales with the square root of the mean stellar density. Several techniques also allow the determination of the frequency at maximum oscillation power, ν_{\max} , in a power spectrum. This frequency is related to the surface gravity of the star and to some lesser extent to the effective temperature. Given the effective temperature, these two quantities give direct access to the mass and radius of the star (Hekker, 2020, see also the quoted reviews above and references therein). Hence, uncertainties of the resulting mass and radius determination directly depend on the uncertainties of $\Delta\nu$, ν_{\max} , and T_{eff} . For a sample of about 500 *Kepler* stars observed in short cadence mode over a period of nearly a month, the quoted average median statistical uncertainties

are $\sim 1.5 - 2\%$ for $\Delta\nu$ and $\sim 4\% - 5.8\%$ for ν_{\max} . For rather high SNR (Verner et al, 2011) these measured seismic observables and their uncertainty lead to a median relative uncertainty of the order of 5.5% and 10% in radius and mass, respectively (Chaplin et al, 2011b). Further *Kepler* data have shown that one must take into account the correlation between ν_{\max} and $\Delta\nu$ due to stellar evolution. This correlation was empirically derived from *Kepler* data (Stello et al, 2009; Huber et al, 2011). Taking it into account in the modelling decreases significantly the statistical uncertainties in masses and radii (Serenelli et al, 2017).

Seismic stellar modelling with scaling relations

A more precise characterisation, including age determination, is obtained when one infers the properties of a star by means of a fitting technique. Usually a grid-based approach is adopted, where one selects the best stellar models from a large grid in such a way that the oscillations predicted for these models satisfy the observational constraints to within a defined matching criterion. Those best-fitting models are often referred to as “optimal (stellar) models” and their properties are attributed to the studied star. The interval of values of each property, such as mass, radius or age, spanned by the set of optimal models is then used to provide an estimate of the uncertainty for that property. Those approaches require that the observational constraints include not only the average seismic parameters but also classical observables such as the effective temperature and the metallicity of the star. The luminosity can be used as an additional constraint or to cross-check as validation after the modelling.

Several pipelines have been developed for asteroseismic modelling, each with the same goal but differing in various aspects. The inter-comparison of their results shows good agreement if all other aspects, such as input data and stellar models, are kept the same. One of the most popular techniques searches the optimal stellar models in a pre-computed grid and is therefore referred to as grid-based modelling (GBM) (e.g. Silva Aguirre et al, 2015; Rodrigues et al, 2017; Rendle et al, 2019; Lebreton and Reese, 2020; Farnir et al, 2021; Aguirre Børsen-Koch et al, 2022, and several others). Because it is easy to use and relatively fast, the GBM approach is favoured for the PLATO baseline stellar modelling pipeline.

The use of seismic average parameters together with a GBM approach leads to a significant reduction of the uncertainties in the overall characterisation of a set of stars compared to those provided by classical modelling methods only, even when including interferometric constraints, as the age uncertainties can still reach more than 50 % in that case (Mathur et al, 2017; Berger et al, 2020). With statistical uncertainties of $\sim 2\%$ for $\Delta\nu$ and $\sim 4\%$ for ν_{\max} , the first GBM determinations for ~ 500 stars with seismic one-month observations yielded median relative uncertainties of the order of 2.8%, 2.2%, 5.4%, and 25% in mean density, radius, mass, and age when spectroscopic effective temperatures are adopted (Chaplin et al, 2014). A number of seismic modelling efforts characterised sets of *Kepler* stars, including planetary hosts. This led to homogeneously derived stellar properties based on the average seismic parameters (Huber et al, 2014; Lundkvist et al, 2016; Campante et al, 2016; Mathur et al, 2017, 2022; Balona and Ozuyar, 2020).

A homogeneous catalogue consisting of 415 stars taken from the Chaplin et al. sample is available, where the seismic analyses were based on long observation baselines up to 1050 days and spectroscopic T_{eff} and metallicity were used (Serenelli et al (2017)). This provided average median precisions of $\sim 1.7\%$ and $\sim 4\%$, respectively, for $\Delta\nu$ and ν_{max} . A GBM stellar characterisation yielded median statistical errors of about 2.3%, 4.2%, and 15% for radius, mass, and age, respectively. We note that the faintest stars in PLATO’s P1 sample as well as a number of the brightest stars in the P5 sample are likely to be in this situation, meaning that for their mass, we are already within the PLATO requirements as far as precision is concerned. The PLATO age-dating requirement, however, still needs to be scrutinised with better models and modelling methodology, which is under current development.

Ultra-precise stellar characterisation based on individual mode frequencies

While acceptable results are obtained by using the average seismic quantities, the most precise stellar characterisation is obtained when a detailed measurement of the frequencies of individual oscillation modes is possible. This occurs for the brightest stars observed over a long temporal baseline. In such cases, individual mode frequencies can be fitted with methods such as the popular “peak-bagging” technique (e.g. Appourchaux, 2003; Handberg and Campante, 2011; Corsaro and De Ridder, 2014). In this way the *Kepler* mission has provided precise seismic and stellar parameters for about 150 dwarfs and subgiant stars, including planetary hosts, using individual frequencies of oscillation modes and various frequency-difference combinations. Combined with optimisation procedures such as a GBM approach, this allowed for a very precise determination of the properties of these stars. The precision obtained with detailed modelling are somewhat dependent on the chosen quantity to be reproduced (frequencies or frequency combinations), as well as the optimisation algorithm and the density of the stellar evolution model grids in terms of the free stellar parameters involved in the fitting procedure.

At present, two major catalogues of stars exist from the viewpoint of containing the best homogeneously derived oscillation frequencies, stellar masses, radii, and ages: the so-called Kages sample and the Legacy sample. The Kages sample includes 35 exoplanet host stars, which were observed over the whole nominal *Kepler* mission, resulting in oscillation frequency uncertainties at the level of $0.3 \mu\text{Hz}$ (best cases $0.1 \mu\text{Hz}$) in the vicinity of ν_{max} for dipolar modes (Davies et al, 2016). Silva Aguirre et al (2015) used combinations of the individual frequencies and a GBM approach to derive stellar properties with median statistical uncertainties of 1.7% (density), 1.2% (radius), 3.3% (mass), and 14% (age). The Legacy sample includes 66 dwarfs of low-mass with short-cadence *Kepler* observations spanning at least 1 year and up to 4 years. With a white noise level ranging between 0.1 and $8 \text{ ppm}^2/\mu\text{Hz}$ ($5.3 - 47 \text{ ppm h}^{1/2}$), frequency uncertainties at ν_{max} for dipolar modes are found in the range $0.03 - 0.35 \mu\text{Hz}$ depending on the star (Lund et al, 2017). The first stellar modelling based on these high quality data was carried out by seven different teams. All teams used their own pipelines, which differ by their optimisation methods, evolution and oscillation codes, input physics assumptions, and seismic diagnostics (individual frequencies or frequency combinations). Quoted average uncertainties range from 0.5%

to 2.6% in density, 1.3% to 4.2% in radius, 2.3% to 4.5% in mass, and 6.7% to 20% in age (Silva Aguirre et al, 2017).

Following these pioneering ensemble modelling studies, a number of theoretical studies flourished using the Legacy sample or a subset of this sample that have confirmed the ability of asteroseismology to provide stellar masses and ages with precisions of a few tens of a percent (e.g. Creevey et al, 2017; Bellinger et al, 2017; Nsamba et al, 2018b; Farnir et al, 2020, 2021; Aguirre Børsen-Koch et al, 2022). As an example, Nissen et al (2020) found uncertainties of typically 10-20% for the ages and masses at the level of 2-4%, while lower than 0.01 dex for surface gravities for the *Kepler* Legacy sample.

These results are in agreement with the level of mass and age uncertainties determined from hare-and-hound exercises (Reese et al, 2016) which give 1.5% (radius), 3.9% (mass), 23% (age), 1.5% (surface gravity), and 1.8% (mean density). For two $1 M_{\odot}$ stellar targets, the precision on the age is better than 10%. Moreover, for the best (mostly brightest) stars in those samples, a seismic determination of the stellar rotation rate and inclination was also possible and valuable for studies on spin-orbit alignment and orbital eccentricities of exoplanetary systems. Those *Kepler* stellar sets are, however, biased towards main-sequence stars hotter and more evolved than the Sun because the oscillation amplitudes are higher in such cases. It is a major goal of the PLATO mission to extend and better populate this seismic dwarf sample with thousands of dwarfs instead of tens.

For cool stars, the TESS survey is more adapted to M-dwarf observations. Yet, in its short cadence mode, TESS provides data enabling the detection of solar-like oscillations and characterisation of very bright ($V \sim 5 - 6$) main-sequence stars (Chontos et al, 2021; Huber et al, 2022; Hatt et al, 2023). TESS is better suited for seismic studies of subgiants due to their larger oscillation amplitudes compared to those of main-sequence stars (Chaplin et al, 2020; Metcalfe et al, 2021). However, the short duration of the TESS observations results in the detection of only a few modes around ν_{\max} . Due to their evolved structure the subgiant frequency spectra include a few mixed modes. The data analysis process and characterisation procedure based on mixed modes has to be more sophisticated but can lead to an extremely precise characterisation in mass and age (see for instance Ball et al, 2020; Nielsen et al, 2020; Li et al, 2020; Noll et al, 2021).

Summarizing at this stage, the Kages and Legacy stars together with a few other individual seismically studied stars from CoRoT, *Kepler*/K2 and TESS represent today's set of most precisely characterised field stars. The addition of asteroseismology to stellar modelling permits to reach levels of $\sim 10\%$ precision in stellar ages at least for stars similar to the Sun (see for the case of Kepler 93 Bétrisey et al, 2022). This complies with the requirements for the PLATO mission as far as precision is concerned. This was further confirmed by a PLATO dedicated hare-and-hound exercises (Cunha et al, 2021, see below). Together with the Sun, those stars are now being used to calibrate gyrochronology relations, which can then be used to age-dating other stars without detected oscillation modes. Those stellar samples also serve as reference stars to validate other techniques capable of constraining stellar properties, such as

the derivation of $\log g$ from photometric variability due to surface granulation (Bugnet et al (2018) and references therein).

4.2 Precision versus accuracy

Precision on stellar radius, mass, and age determinations as mentioned above is associated with statistical uncertainties due to the propagation of observational errors. In addition to those uncertainties, one must also account for systematic errors or biases for assessing the accuracy of the seismic results. Such systematic errors contribute to the final error budget but do not directly depend on the observations themselves. Rather, they depend on our ability to improve the data-analysis procedures, adopted choice of constraints, optimisation procedures and strategies, and most importantly approximations adopted for the physical description of the stellar models used in seismic inferences. When highly precise and accurate seismic observations are available together with precise and accurate classical stellar parameters (effective temperature, chemical composition), the statistical errors on the derived stellar properties decrease to a level where the systematic errors due to stellar modelling dominate the uncertainties.

Several studies using simulations have shown that, given the same input set of information, the various data-analysis and optimisation methods have reached such a high level of sophistication that they do not introduce large biases and yield similar results. In contrast, even restricting the case to low-mass main-sequence and subgiant stars as we do here, important sources of systematic errors result from our poor knowledge of various physical processes that affect the stellar structure and evolution, as well as the oscillation frequencies. This is particularly true for the age, which of all stellar properties, is by far the most challenging to determine accurately. In most cases, stellar ages can only be determined through stellar modelling and their accuracy therefore strongly depends on the degree of reliability of the available stellar models (e.g., Christensen-Dalsgaard and Silva Aguirre, 2018). Particularly critical (and uncertain) are physical processes that mix the chemical elements in the stellar cores, affecting the relation between the age and the composition profile and, thus, the seismically inferred age.

The stellar properties of the targets in the Legacy sample modelled by Silva Aguirre et al (2017) were actually determined with varying degrees of uncertainties depending on the adopted pipeline (including different input grids of stellar models) while using the same observational data. When considering the results of the three pipelines – out of the seven considered – which used the same seismic diagnostics (individual frequencies), the median age uncertainties range from 0.5 – 0.8%, 1.3 %, and 6.7 – 10% for the three respective pipelines. The spread of these uncertainties can be mostly attributed to the use of different input physics assumed by the three pipelines and not to the pipeline operational strategies themselves. For instance, the lowest values of these uncertainties can be partly attributed to a different adopted GBM procedure. Yet the systematic uncertainties are mostly due to the use of a grid of stellar models where the values of two free parameters are held fixed, while for the other two pipelines they are left either variable or free to take more than one value. Fixing the values of the parameters (usually taken as those of the Sun) decreases the uncertainties but at the cost of being less accurate since there is usually no reason for these parameters to

take exactly the solar values. This is confirmed with PLATO hare-and-hound exercises (Cunha et al, 2021).

Therefore, besides the precision, one must also be concerned about the accuracy of the central or median values themselves: how can we assess the accuracy of these results? Improving stellar modelling not only requires theoretical developments but also a set of very well and accurately characterised stars. The latter serve to diagnose the dominant shortcomings in stellar modelling on one hand and to validate the theoretical developments designed to correct for those shortcomings on the other hand. Characterisation of the properties of such stars must of course be as independent from stellar models as possible (e.g. benchmark stars such as eclipsing binaries, stars with interferometric radii) or enable ensemble studies to constrain some physical ingredient or to calibrate a free parameter involved in an empirical physical formulation (stars in clusters, unevolved massive stars, red giants).

Accuracy tests: the Sun. A routinely used test of the accuracy of seismic modelling is to look at the results for the so-called “degraded” Sun for which seismic and non-seismic data were built to match the typical quality of the *Kepler* Legacy sample ($\sim 0.15 \mu\text{Hz}$ for a $l = 1$ mode at ν_{max}). The derived values depart from the independently known solar values by $\sim 3\%$, 0.8% , 1% , and 9.8% for the solar luminosity, radius, mass, and age, respectively, the differences being mainly due to the adopted chemical composition. This must be compared to 1σ uncertainty given by the pipelines, which are in the typical range $0.5 - 4\%$ and $3 - 8\%$ for the mass and age. While the net error budget for the “degraded” Sun is at the level of 10% accuracy for the age, one must keep in mind that the seismic Sun is still discrepant in several aspects compared to our real Sun (Christensen-Dalsgaard, 2021). The same discrepancies, still not fully identified, will have an impact of unknown magnitude for other (solar-like) stars for which no independent age is available and differing in mass, chemical composition, evolution, and environment.

Accuracy tests: independent additional observational information. For *Kepler* stars using interferometric or astrometric observations as external constraints, scaling relations have been reported to be accurate at the level of $\sim 2\%$ in density, $2 - 5\%$ in radius, and about 5% in masses for dwarfs and subgiants (e.g. Coelho et al, 2015; Huber et al, 2017; Zinn et al, 2019). Taking into account several different sources of systematic error in a GBM approach, Serenelli et al (2017) quoted a systematic error of the order of 1.2% in radius, 3% in mass and 12% in age with a total combined error of approximately 2.6% in radius, 5.1% in mass, and $\sim 19\%$ in age (see Tab.2 in Serenelli et al, 2017). Those studies also emphasised the importance of having accurate and precise classical parameters to exploit the full potential of seismology. Getting such classical parameters requires the development of specific and sophisticated pipelines based on as accurate model atmospheres as possible (Morel et al, 2021; Gent et al, 2022). This by itself represents a whole branch of stellar astrophysics, which contributes to properly characterise stars.

Accuracy tests: “differential” studies. Another commonly used way of at least partially assessing the accuracy is rather differential than absolute: it consists of considering the dispersion of the results provided by different pipelines (which differ in many

aspects of input physics) or the results coming from a single pipeline but varying the input physics of the stellar models. In this context, several studies have revisited the characterisation of the Kages and *Kepler* Legacy stars. It was found that significant systematic differences for the mean values of the mass and the age occur. The dispersion in medium age can range between $\sim 15\%$ and $\sim 33\%$. This is attributed to different options about the optimisation strategy but mostly to different options of the stellar modelling (Bellinger et al, 2016, 2017; Creevey et al, 2017; Farnir et al, 2020; Nsamba et al, 2018b,a, 2021). The most studied Legacy stars are the brightest (G1.5V + G3V) solar analogue components A and B of the multiple system 16 Cyg (with apparent *Kepler* magnitudes $K_p \sim 5.86$ and 6.09 , respectively). Their masses are precisely determined at the level of 3% or below. Most studies passed the accuracy test of both stars having the same age – as expected for a binary system – within the quoted uncertainties (reported to be in the range $2 - 6\%$ depending on the study) (e.g. Silva Aguirre et al, 2017; Creevey et al, 2017; Bellinger et al, 2016, 2017; Buldgen et al, 2016; Verma et al, 2016; Bazot, 2020). However, examining the mean values derived by those various studies tells us that the seismically derived age of 16 Cyg A covers a range of $\sim 6.4 - 8.3$ Gyr depending on the assumed input physics. Farnir et al (2020) modelled both stars varying one input physical ingredient at a time and found ages in the range $6.4 (\pm 0.08)$ to $7.5 (\pm 0.1)$ Gyr. This represents an age dispersion up to about 16% when one takes 6.95 Gyr as a reference mean value for 16 Cyg A. All these above dispersion estimates are larger than the uncertainties provided by each individual pipeline and currently remain larger than the 10% accuracy for such a type of star as required for the PLATO mission.

Accuracy tests: seismic inversions. They represent the most efficient way to diagnose shortcomings in stellar modelling by providing model-independent constraints (Buldgen et al, 2017, 2018, 2019; Bellinger, 2020). We must however stress that the inversion techniques need to be performed from a reference model that is assumed to be already fairly close to the actual stellar structure. For dwarfs other than the Sun, their use remains difficult due to the small number of significant modes. Inversions are therefore restricted to the brightest stars with the highest SNR such as 16 Cyg AB (Buldgen et al, 2016; Bellinger et al, 2017). The seismic inversions for the 16 Cyg AB system reveal discrepancies in the sound-speed profiles when using the currently adopted physics of stellar models. The stellar modelling of the most constrained system 16 Cyg AB is therefore still not satisfactory as it cannot reproduce simultaneously all the seismic and non-seismic constraints. For the main-sequence star KIC 622571 (Bellinger et al, 2019) and the subgiant HR 7322 (Bellinger et al, 2021) discrepancies were also found in the sound-speed profile at the border between respectively the convective core or the helium core and the layers above. In all these cases, the origins of the discrepancies are not yet identified, although it is likely due to some missing or poorly modelled transport processes with a so far unknown impact on the age accuracy.

Although the various sources of systematic errors due to stellar modelling cannot be detailed here, it is clear that improvements in stellar modelling are still necessary in the coming years in order to reach the PLATO age-dating requirement. This is within reach from intense on-going theoretical work within the PMC addressing the main

inaccuracy issues. Real advances in this activity will come from the confrontation of the updated modelling with observations of a sample of well-characterised stars (i.e., with the highest possible precision and accuracy, mainly via seismology).

4.3 Detecting solar-like oscillations with PLATO

PLATO will complement the above samples with a much larger number of bright main-sequence stars (hereafter MS-stars) and subgiants, increasing significantly the number of low-mass seismically-characterised stars. A total of 630 *Kepler* stars (see Fig. 10) belong to the PLATO observable fields of view mentioned in [Nascimbeni et al \(2022\)](#). Of this set, 296 *Kepler* stars belong to the P1 sample (14886 stars) and 331 *Kepler* stars are in the P5 sample (266673 stars). Among the 57 Legacy stars in the PLATO Input Catalogue (PIC), 49 are in the P1 sample.

The requirements of the PLATO mission are extremely challenging, especially for the stellar age (e.g. 10% accuracy for a reference star with $V = 10$ mag with $1M_{\odot}, 1R_{\odot}, T_{\text{eff}} = 6000$ K – that is a solar analogue slightly hotter than our Sun). In the following, the assessment of the seismic performance of PLATO is discussed at two levels: the detection of oscillations as an excess of power in a power spectrum that comes with the measurement of the two averaged seismic parameters and the detection of oscillation modes for which individual frequencies will be measured. We will consider the performance for the sample P1–P2 on the one hand and the sample P5 on the other hand. The estimates are based on what *Kepler* data taught us (for details see, [Goupil et al. in prep.](#)).

The P1–P2 sample is deliberately designed as composed of stars with a noise level (random and systematic residual, non-stellar) below 50 ppm $h^{1/2}$ at magnitude $V = 11$. It is therefore made up of a large number of targets for which one expects the detection of solar-like oscillations in the majority of cases (K-stars remain an open issue) as well as the measurement of individual mode frequencies with a precision high enough to provide high quality seismic masses, radii, and ages. We expect a considerable improvement in the quality of stellar modelling in terms of accuracy thanks to the P1–P2 seismic sample.

The P5 sample, on the other hand, consists of stars to be observed with a lower SNR. Its targets will mostly be observed with a cadence of 600 s, which is too long to properly detect solar-type oscillations of dwarfs and subgiants. However, at least 10 % of these stars will be observed with a cadence of 50 s (see Section 6), suitable for the detection of stellar oscillations and for a measurement of the two global seismic parameters that can provide seismic masses, radii, and ages. The precision will be degraded compared to the results for the P1–P2 sample but will nevertheless greatly improve their modelling compared to the stars without seismic constraints.

4.3.1 Expected solar-like oscillations within the PLATO P1-P2 sample

The first question is to what extent solar-like oscillations can be detected for PLATO targets. Figure 11 shows the stars in the P1–P2 sample for two long-pointing fields in an HR diagram. They are taken from the PIC version PICv1.1.0 ([Nascimbeni et al,](#)

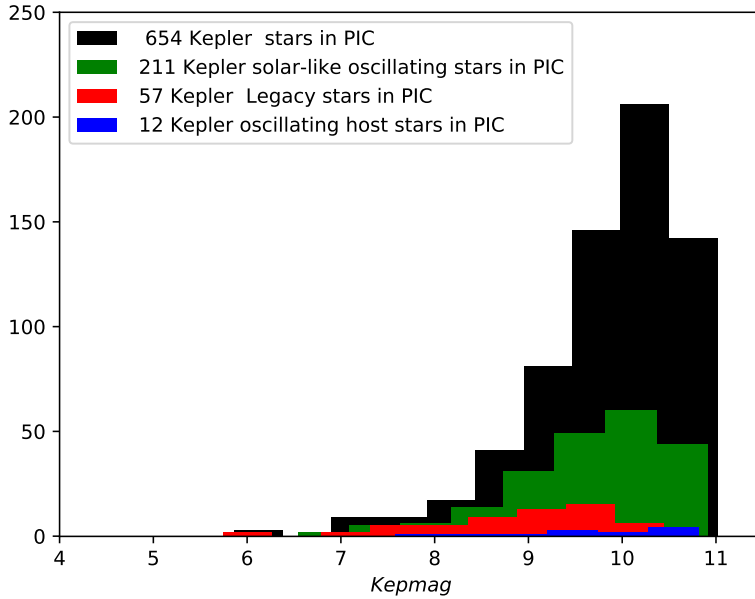


Fig. 10 Distribution of various types of *Kepler* stars in the PIC (Nascimbeni et al, 2022) according to their brightness, as labelled according to the legend.

2022), which provides effective temperatures and stellar radii, hence luminosities. In Fig. 11, we distinguish between stars for which a theoretical calculation has led to a probability of detection of solar-type oscillations and those for which the threshold for a positive seismic detection has not been reached. The probability of detection were not calculated for hot stars in the instability band defined according to the criterion adopted by (Chaplin et al, 2011b). This concerns few stars because the restriction on the temperature of the hot side adopted to construct the PIC is more severe. We also did not consider the early red giants –also contained in the PIC– which will be included in a specific scientific calibration sample catalogue as part of the overall PIC (Aerts, 2021). Their performance will be addressed elsewhere. Once early red giants and hot stars have been removed, the total subsample (dwarfs and subgiants) contains 14083 stars. We considered a positive seismic detection when the probability of the signal being due to noise is below 0.1% and the probability of detecting solar-like oscillations is equal to 99% or above. The computation of the probability was adapted from the one described in Chaplin et al. (2011a). The seismic detection probability depends on the observing duration. We therefore show two cases in Fig.11 : observing runs of 30 days and 2 years long. The probability also involves the signal-to-noise ratio in a power spectrum. We then used a combination of the formulations by Chaplin et al (2011b) and by Samadi et al (2019) for the oscillation amplitudes calibrated with *Kepler* data (a compilation of oscillating stars from the catalogues of Serenelli et al (2017) and Mathur et al (2022) and short-cadence stars found with no detection from

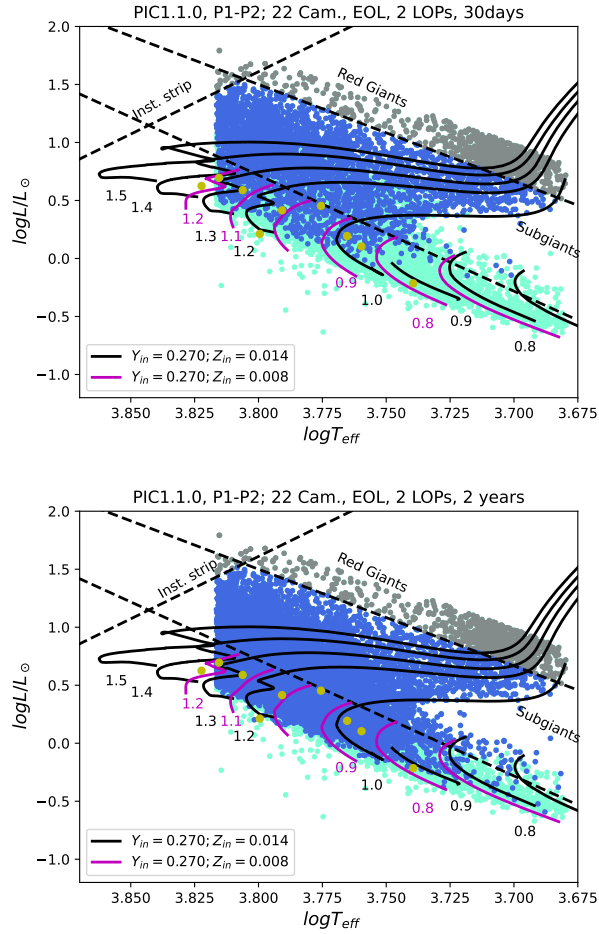


Fig. 11 HR diagram showing the subsample of P1–P2 dwarfs and subgiants of the PIC catalogue for which a theoretical calculation led to a probability of detecting solar-like oscillations equal or above 99% (blue dots). Stars for which the detection level 99% was not reached are represented with cyan dots. Early red giants and hot stars beyond the instability strip - included in the PIC catalogue but not in P1–P2- are shown in grey dots. The detection probability assumed an observing run of 30 (top) and 730 (bottom) days. Yellow dots represent selected stars from the *Kepler* Legacy sample. We classify stars as main sequence stars when they satisfy $\log T_{\text{eff}} \geq 3.7282 + 0.10 \log L/L_{\odot}$ which corresponds to a central hydrogen relative abundance in mass greater than 10^{-6} . Subgiants are then located above that threshold in a HR diagram as represented by a dashed line. Dashed lines also delineate the instability strip and the arbitrary separation between subgiants and early red giants. The coloured solid curves represent evolutionary models for masses ranging from 0.8 to $1.5 M_{\odot}$ and for two initial metallicities.

the [Mathur et al \(2019\)](#) catalogue. For the noise, we used the PLATO (random and systematic residuals) noise level included in the PIC, to which we added the stellar granulation background noise. For comparison, we included in the plot the positions of some *Kepler* stars from the Legacy sample ([Lund et al, 2017](#); [Silva Aguirre et al,](#)

2017) as characterised by Creevey et al (2017). The calculation of the probability to detect oscillations also depends on the width ($\delta\nu_{\text{env}}$) of the assumed Gaussian-shape envelope due to oscillations in a power spectrum. From observations, $\delta\nu_{\text{env}}$ ranges from ν_{max} to $\nu_{\text{max}}/2$. The first option ($\delta\nu_{\text{env}} = \nu_{\text{max}}$ together with a probability threshold set at 0.90) provides a number of positive detections in agreement with the number of *Kepler* stars with detected oscillations, but a too large number of false-positive detections among the *Kepler* stars with no detected oscillations. For the other option ($\delta\nu_{\text{env}} = \nu_{\text{max}}/2$ together with a conservative probability threshold of 0.99), it is the reverse, i.e., the number of predicted non-detections is in agreement with the number of *Kepler* stars without oscillations, but too few detections are found compared to the *Kepler* stars with detected oscillations. Here we remain conservative and use the second option to derive the number of expected detections for PLATO. We count ≈ 11408 PLATO P1–P2 stars – including ≈ 6137 subgiants – for which detections of solar-like oscillations are expected after 2 years of observation. These stars span the whole range of mass and age of the P1–P2 sample. With 2 years of observation, the number of MS-stars with expected detection is about 5271. The impact of the observation duration is significant: from 30 days to 2 years and limiting the count to stars with masses $\leq 1.2M_{\odot}$, the number of detections increases from 324 ($\sim 7.5\%$ of stars with masses $\leq 1.2M_{\odot}$) to 2393 ($\sim 55\%$ of stars with masses $\leq 1.2M_{\odot}$). Had we assumed the other option, the number of expected detections for stars with mass $\leq 1.2M_{\odot}$ would increase up to 3291 (76% of stars with masses $< 1.2M_{\odot}$) for a 2 years run. Not surprisingly, stars for which one might not detect solar-like oscillations for too short an observing time are MS- stars of low mass because their oscillation amplitudes are too small. In contrast, detection of solar-like oscillations - when applied to the *Kepler* sample- is not obtained for some stars for which they are theoretically expected (Chaplin et al, 2011b,a; Mathur et al, 2019). Several reasons may occur, one being the strong magnetic activity. As an example, we found $\approx 8\%$ false-positive detections for the Mathur et al (2019) *Kepler* sample. Based on this, the number of PLATO detections for main-sequence stars with mass $\leq 1.2M_{\odot}$ decreases to $\sim 51\%$.

Uncertainties in the probability calculation and the number of stars with expected detections of solar-like oscillation may originate from the use of the PIC1.1.0 radius and effective temperature adopted to compute the global seismic parameters and to derive the seismic mass. The scaling relations used to derive the seismic masses remain themselves approximate and as a result the number of stars in the different mass regimes remains also approximated, albeit with the same order of magnitude.

4.3.2 Expected solar-like oscillations within PLATO P5 sample

Let us note that 10% of the P5 sample will be observed with a 50 s cadence. This will make it possible to detect solar-like oscillations and to measure at least the global seismic parameters $\Delta\nu$ and ν_{max} . We performed the same probability calculation as for the P1–P2 sample after eliminating the same types of stars and assuming a detection probability equal or greater than 99% (and $\delta\nu_{\text{env}} = \nu_{\text{max}}/2$). The number of seismic positive detections is estimated to be 9941 stars for an observation period of 2 years. This number falls to 5637 stars after only 1 year of observation and only 401 stars after 30 days of observations. In the last case, none are expected to be in the main sequence:

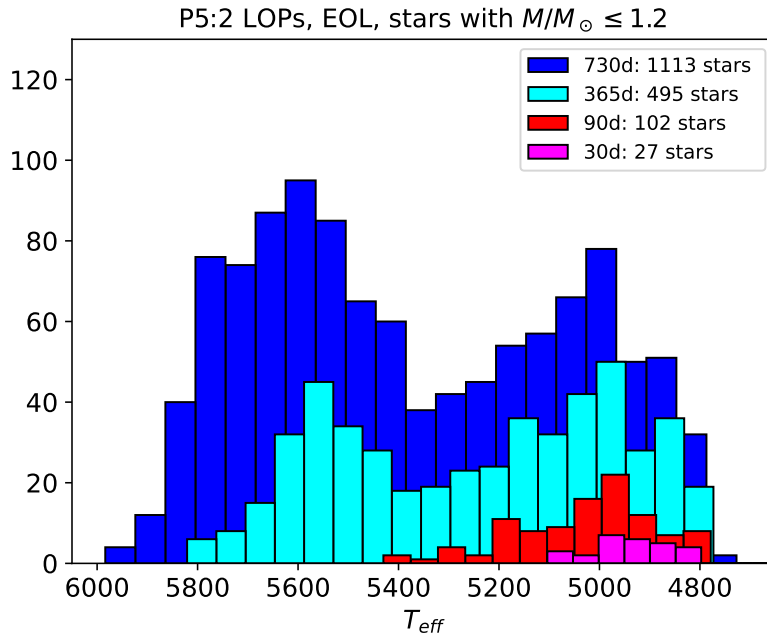


Fig. 12 Histogram of the number of stars with masses $M \leq 1.2M_{\odot}$ from the P5 sample with an expected detection of solar-like oscillations with a at least 99% probability for uninterrupted observations lasting 730, 365, 90 and 30 days.

the sample is dominated by subgiants because their amplitudes (roughly $\propto L/M$) are higher than for main-sequence stars. The drastic increase of detections of oscillating stars with the observing time in the P5 sample is illustrated in Fig. 12.

4.4 PLATO seismic performance for stellar mass, radius, and age characterisation for the P1–P2 sample

For the subset of P1–P2 stars with expected solar-like oscillations, the detection and highly precise measurement of individual frequencies for a significant number of modes is ensured by the selection of a high signal-to-noise ratio by construction. This will allow the determination of the stellar age at the level of 10% for F and G stars. As an illustration of the expected PLATO performance, Samadi et al (2019), to which we refer for details, illustrated the excellent PLATO performance for the *Kepler* legacy star, 16 Cyg B, a 6th magnitude dwarf observed over 815 days. The simulated PLATO power spectrum built assuming the expected noise for a $V = 10$ star observed with 24 cameras at the end-of-life (EOL) conditions and for 2 years of observations with the PSLS simulator reveals the strong capacity of the mission to detect the oscillations (note that the noise level was for 28 telescopes ($34 \text{ ppm h}^{1/2}$) at the time).

Oscillation frequency uncertainties

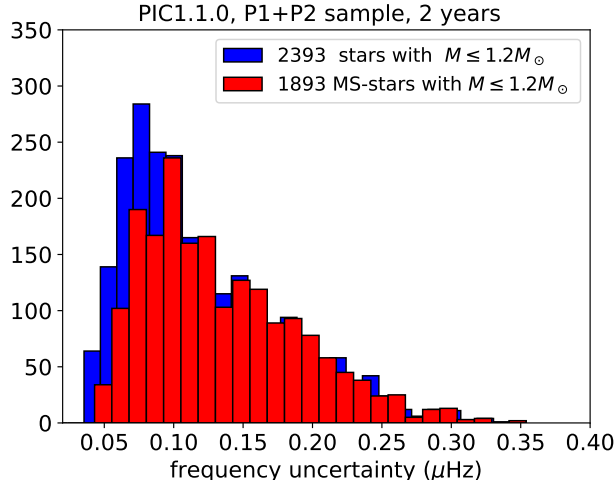


Fig. 13 Histogram of the frequency uncertainties for an $l = 1$ mode at ν_{\max} for the sample of P1–P2 low mass stars with detection probability equal or larger than 99%.

Dipole ($l = 1$) modes produce the highest amplitude and smallest uncertainty, so we focus on these here. Denoting the uncertainty of the $l = 1$ mode closest to ν_{\max} as σ_1 , *Kepler* data taught us that a precision on frequencies of the order of $\sigma_1 = 0.2\mu\text{Hz}$ for a few modes around the frequency at maximum power can provide an age precision at the level of 10% for a Sun-like star. Several hare-and-hound exercises using artificial data constructed for the PLATO noise characteristics were conducted by PMC members (e.g. Goupil 2017, Cunha et al 2021) and confirmed this result. The artificial star named Zebedee and studied by Cunha et al (2021) has a mass, radius, and effective temperature similar to the PLATO reference star and is situated close to the PIC star, PICid 8525275 ($V = 10.28$ mag). With an assumed PLATO noise level for a 9th magnitude star, the frequency uncertainty was found to be $\sigma_1 = 0.13\mu\text{Hz}$ at ν_{\max} and the age uncertainty was 13%. The target was estimated to be 3.085 Gyr old, i.e., younger than the Sun. Rescaling to the solar age, the age uncertainty is at the level of $\sim 8.8\%$. When the Zebedee data are degraded to the level that the frequency uncertainty increases to $\sigma_1 = 0.39\mu\text{Hz}$, corresponding to a $V \sim 10.5$ mag star, Cunha et al (2021) found an age uncertainty of the order of 15%. This becomes $\sim 10\%$ when rescaling to the Sun’s age. Another practical yet more conservative estimation results from using $\Delta\text{age}/\text{age} = \sigma_1/2.2$ (Appourchaux et al, 2016), leading to a relative age uncertainty of 17% for Zebedee, turning into a relative age uncertainty of $\sim 12\%$ when rescaling to the Sun’s age at 10.5 mag.

Lund et al (2017) computed how the frequency uncertainties for individual modes decrease with increasing observation duration. A light curve was simulated for a star of $V = 10.5$ mag with $M = 1.12M_{\odot}$, $R = 1.20R_{\odot}$, $T_{\text{eff}} = 6129$ K. The foreseen PLATO reference noise level of $34 \text{ ppm h}^{1/2}$ at magnitude 11 for 28 telescopes at the time of this study was used. With an updated current reference noise level of $50 \text{ ppm h}^{1/2}$ at magnitude 11 (Börner et al. in prep.), the frequency uncertainties correspond to a

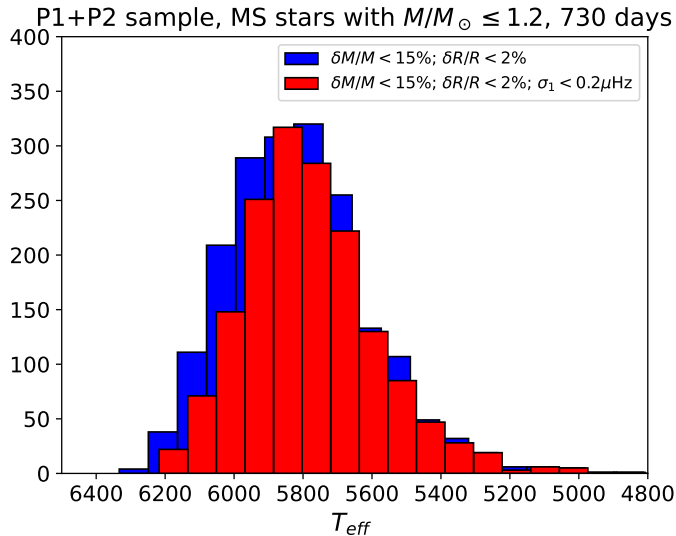


Fig. 14 Histograms of T_{eff} for MS-stars with masses $M \leq 1.2M_{\odot}$ in the P1 -P2 sample with expected detection of solar-like oscillation after 730 days of observation and satisfying $\delta M/M < 15\%$ and $\delta R/R \leq 2\%$ (blue, 1893 stars); $\delta M/M < 15\%$, $\delta R/R \leq 2\%$ and Libbrecht (1992) frequency uncertainty of the dipole mode with frequency closest ν_{max} , $\sigma_1 < 0.5\mu\text{Hz}$ (red, 1640 stars) and.

simulated star of $V \sim 9.7$ mag. The frequency uncertainty increases with increasing magnitude but decreases with decreasing effective temperature. In this way, it is found that a level of $0.2 \mu\text{Hz}$ can be reached after more than roughly 1.5 years of observations. We will then take that criterion to estimate the number of stars for which one can reach a statistical error of 10% for the stellar age of a reference star.

Assuming individual frequencies are available, we determine the uncertainty on the frequencies using the Libbrecht (1992) formula, which depends on the total SNR and the duration of the observation and has been proven to yield the right order of magnitude. Figure. 13 shows the histogram of the frequency uncertainty σ_1 computed from the formulation by Libbrecht (1992) for each P1–P2 star for which the detection probability is equal to or larger than 99% and with masses less or equal to $1.2M_{\odot}$. The bulk of stars have frequency uncertainties below about $0.12 \mu\text{Hz}$. Those estimates are purely theoretical but give the same order of magnitude than for the *Kepler* Legacy sample.

Mass, radius and age seismic uncertainties

We now turn to the expected accuracy of the seismic determinations of masses, radii, and ages. For the mass and radius relative uncertainties, we used empirical formulations obtained as fits of the results of seismic inferences of mass, radius and age of synthetic stellar models (see Goupil et al. in prep. for detail). For the age uncertainty, as mentioned above, we consider the criterion $\sigma_1 \leq 0.2\mu\text{Hz}$ as a proxy for the requirement on the age uncertainty (i.e. \leq than 10%). Those estimates indicate that roughly 5271 MS-stars will have mass and radius uncertainties below 15% and 2% respectively. Among them about 2651 stars will have a frequency uncertainty

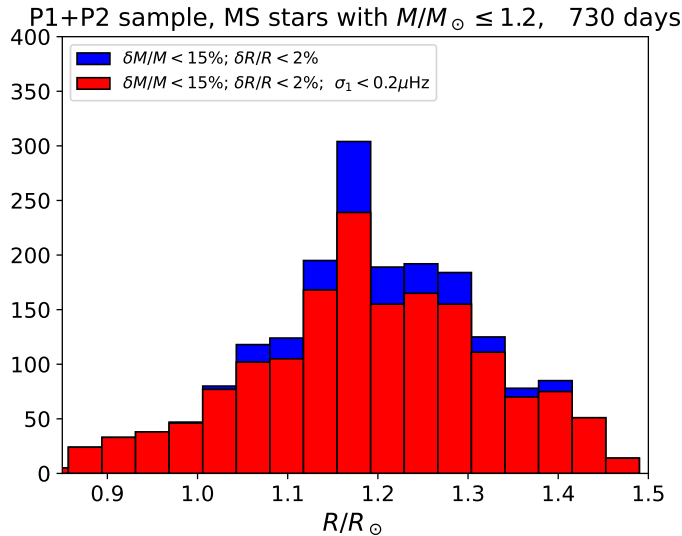


Fig. 15 Same as Fig. 14 but for the stellar radius.

$\sigma_1 \leq 0.2\mu\text{Hz}$. Figures 14, and 15 focus on MS-stars with masses $M/M_{\odot} \leq 1.2$ and show the T_{eff} , and radius histograms for stars satisfying the above constraints : mass and radius relative uncertainties better than 15 % and 2% respectively and $\sigma_1 \leq 0.2\mu\text{Hz}$. Of interest for the exoplanet yields, 1640 stars with masses $M \leq 1.2M_{\odot}$ and 937 stars with radius $\leq 1.2R_{\odot}$ have $\sigma_1 \leq 0.2 \mu\text{Hz}$.

We recall that our estimates are based on a PLATO noise level corresponding to observations with 22 cameras at EOL. Note also that the above uncertainties refer to precision and do not account for systematic errors due to limitations in the models of stellar interiors and atmospheres discussed above (such as surface effects, [Jørgensen et al \(2020\)](#), or stellar activity). Currently the total uncertainties increase roughly by ~ 3 to 5% due to lack of accuracy for a solar-like star and to $\sim 15\%$ – 50% for a more massive star with a convective core. Theoretical work is ongoing to decrease the impact of lack of accuracy. The impact of the main systematic effects were investigated by ([Cunha et al, 2021](#)) in view of PLATO applications using also seismic inferences of mass, radius and age of synthetic stellar models.

4.5 Expectations for M dwarfs (P4 Sample)

One does not expect to detect solar-like oscillations for M-dwarfs, mainly because of their high level of activity. Without seismic data from the PLATO mission, one will have to resort to classical methods and stellar models to characterise such stars (see for instance the input Carmenes catalogue, [Cifuentes et al \(2020\)](#) and references therein).

In the framework of the PLATO project, an updated and accurate preliminary library of stellar models for M-dwarfs – stars with $M < 0.5M_{\odot}$ – has been produced. This model set is based on the best available input physics as far as opacity and thermodynamical tabulations, nuclear cross sections, and outer boundary conditions

are concerned. Comparison with suitable observational benchmarks has shown good agreement between model predictions and observations, although some discrepancies occur. More precisely, in the regime of fully convective stars ($M < \sim 0.35M_{\odot}$), stellar models over-predict the effective temperature of suitable benchmark stars by on average 3–4%, and underestimate the stellar radius by about 5%. Current theoretical mass – IR-band magnitude luminosity relations to derive the mass of M dwarfs deliver an accuracy of the order of 4% (e.g., [Passegger et al 2019](#)). Quantifying the uncertainty of the age estimation is, however, quite difficult due to the intrinsic extremely long evolutionary lifetimes of M dwarfs. A search for suitable binary systems formed by an M dwarf and a more massive star is ongoing within the PMC. Improvements in M-dwarf modelling are expected on the topics of better treatment of the outer boundary conditions – a critical issue in the computation of M dwarf models – of convection and its link with the presence of magnetic fields and with the process of formation via mass accretion during the pre-main-sequence stage. All these poorly known phenomena affect the structural and evolutionary properties of these intriguing low-mass host stars.

4.6 Measurement of surface rotation period, stellar activity indices and flares

Stellar rotation, whether uniform or differential, is an important input to both the Exoplanet and Stellar Analysis Pipelines of PLATO. Indeed, in order to characterise and model the host star and its cohort of planets, information about the occurrence of stellar activity and its magnitude is required for both applications. Measurements of various quantities related to stellar rotation and activity are therefore among the top objectives of the PLATO mission. The measurement procedures rely on our experience obtained from the *Kepler data* ([García et al, 2011](#); [Handberg and Lund, 2014](#); [McQuillan et al, 2013](#); [Garcia et al, 2014](#); [McQuillan et al, 2014b](#); [Aigrain et al, 2015](#); [Breton et al, 2021](#); [Santos et al, 2021](#)).

All the PLATO photometric timeseries will be analysed to search for surface rotation periods, surface differential rotation, and magnetic indicators and activity cycles. The analyses will be carried out on the data collected during each quarter, and on consecutive stitched quarters as the mission progresses. Such techniques are very sensitive to contamination from instrumental modulations. The long-term stability of the instrument at low-frequency is therefore crucial as discussed by [Santos et al \(2019\)](#) for instance. The time series will be analysed using a combination of different algorithms, such as the Generalised Lomb-Scargle (GLS; [Handberg and Lund 2014](#) and references therein) and the AutoCorrelation Function (ACF; [McQuillan et al 2013](#); [Garcia et al 2014](#)), to produce a composite spectrum (hereafter CS) ([Ceillier et al, 2016, 2017](#)). Only highly-significant periodicities in the GLS power spectrum will be considered. Once the rotation period is identified in the CS, a machine learning (ML) random-forest approach is used to decide if the final rotation period will be the one computed from the GLS, the ACF or the CS (see, e.g., the Random fOrest Over STEllar Rotation (ROOSTER) methodology; ([Breton et al, 2021](#); [Santos et al, 2021](#))). Some additional stellar parameters such as luminosity or effective temperature can also be used to help in such selection.

An important point of such a methodology is that a random forest allows us to use more parameters in the decision than a manually-set threshold when assessing the robustness of a rotation detection and selecting the corresponding rotation period. This methodology has the advantage of preserving the uncertainty and the posterior distribution of the method selected by the random forest. This type of machine learning algorithm can be combined with any inference techniques applied on the light curve or the periodogram. In the baseline version of the PLATO pipeline, the uncertainty associated with the rotation period and the activity cycle length will be inferred from the width of the corresponding power spectrum peak, and it is expected to improve as the timeseries get longer. Candidate values for starspots and levels of differential rotation will be inferred from the relative difference between the rotation period and other, if any, significant periodicities. Such candidate values will be validated using priors from theoretical models, as well as information on either the single or binary nature of the star, since unresolved secondary components can also produce detectable periodicities in the flux timeseries. The presence and length of long-term periodicities, likely arising from either activity cycles or from beating of close frequencies, will be inferred as done for the rotation period, but focusing on the lower-frequency region of the power spectrum computed from the stitched timeseries. The baseline version of the PLATO pipeline may miss the detection of rotational modulation signals in stars with a low level of activity and active regions with lifetimes shorter than the rotation period such as the Sun during some specific activity phases along its activity cycle (cf. [Reinhold et al 2021](#)). In such cases, we plan to apply other methods to estimate the stellar rotation period in future versions of the PLATO pipeline. Although with a lower precision of about 15-20%, those methods can be applied to stars with a low-activity level at an age comparable or older than the Sun (e.g. [Amazo-Gómez et al 2020](#); [Reinhold et al 2022](#)).

The Stellar Analysis pipeline will also detect and remove stellar flares from PLATO light curves. Flares are both a nuisance for the detection of exoplanet transits or any other astrophysical signal in PLATO light curves and an important input parameter for the modelling of the evolution of planetary atmospheres ([Tilley et al, 2019](#); [Gronoff et al, 2020](#)). The duration, peak flux, and total energy of these events in the PLATO passband will be measured. Typical durations of optical flares are on the order of few minutes up to about one hour, and the flare duration and energy are correlated ([Namekata et al, 2017](#)). This makes PLATO with its superb data cadence combined with unprecedented photometric precision ideally suited to study these fast transients.

5 The PLATO Complementary Science programs

5.1 Background

PLATO's Complementary Science (PLATO-CS hereafter) is dedicated to exploit the mission's capacity for answering scientific questions outside its core remit and can be addressed via successful proposals within PLATO's Guest Observer (GO) programme (see Section 10). Up to 8% of PLATO's science data rate will be spent on PLATO-CS and will make it a unique legacy programme.

Previous photometric space missions built for exoplanet detection by the transit method, such as CoRoT (Auvergne et al, 2009), *Kepler* (Koch et al, 2010), and TESS (Ricker et al, 2015) have already shown that the uninterrupted high-precision photometric light curves they assembled triggered studies far beyond the nominal mission goals. PLATO-CS will combine the best of *Kepler* and TESS in that it will provide a legacy programme based on long-term monitoring capacity for a huge sky coverage per Field-of-View (FoV), containing stars with a dynamical range in brightness covering ten orders of magnitudes, for sampling rates of 2.5 s, 25 s, 50 s, and 10 min. PLATO-CS will be able to rely on all raw (L0) and calibrated (L1) PLATO light curves, as well as imagerettes for tens of thousands of them.

5.2 Support for the community

The PLATO-CS activity within ESA’s Science Working Team and supported by the PMC has several operational aims. First of all, it will help the worldwide community to prepare competitive GO programs (see Section 10) by means of simulated data and by using *Kepler* and TESS as preparatory tools and testbeds. The PLATO simulation *PlatoSim* (Janssen et al, 2023) offers a versatile tool for the community to help prepare the assessment of PLATO’s capacity for various scientific goals. PLATO-CS will encourage and trigger GO proposals covering a variety of topics in Solar System science, stellar astrophysics, the Milky Way galaxy, transients and more broadly extragalactic science. Although we anticipate a large over-subscription factor for the GO call, the PLATO-CS team will facilitate relevant simulations with *PlatoSim* to showcase PLATO’s capacity for the CS, which will stimulate interest in the worldwide community.

A second crucial activity within the ongoing PLATO-CS activity is to offer the community an electronic database containing a variability classification of the stars in the FoV prior to the launch of PLATO. An intense activity to train a meta-classifier by means of supervised and unsupervised classification is currently ongoing. This classification relies on machine-learning tools and is trained on *Kepler* light curves and class definition. Global and refined variability classifications will be done for the TESS all-sky survey (Audenaert et al, 2021). With PLATO’s first FoV being recently fixed, these TESS variability classifications will be cross-matched with the sky position, and the content will be fine-tuned to be optimally suitable to help the community in its hunt for the best targets for all the science cases. The PLATO-CS variability catalogue will be made publicly available via a webform and will be continuously updated as newer results from the classifiers become available (Audenaert et al, 2022). This variability catalogue will be a major source of information for GO applicants.

Other examples PLATO-CS can cover include, e.g., non-core exoplanet science as well as Solar System objects (see also examples in Rauer et al 2014), such as microlensing events, stellar occultations by Solar System objects (e.g. asteroids), or studies of star-planet interaction mechanisms via phase curves detecting hot spots induced by orbiting planets (Shkolnik et al, 2003).

We now provide three examples from stellar sciences which PLATO will be able to address.

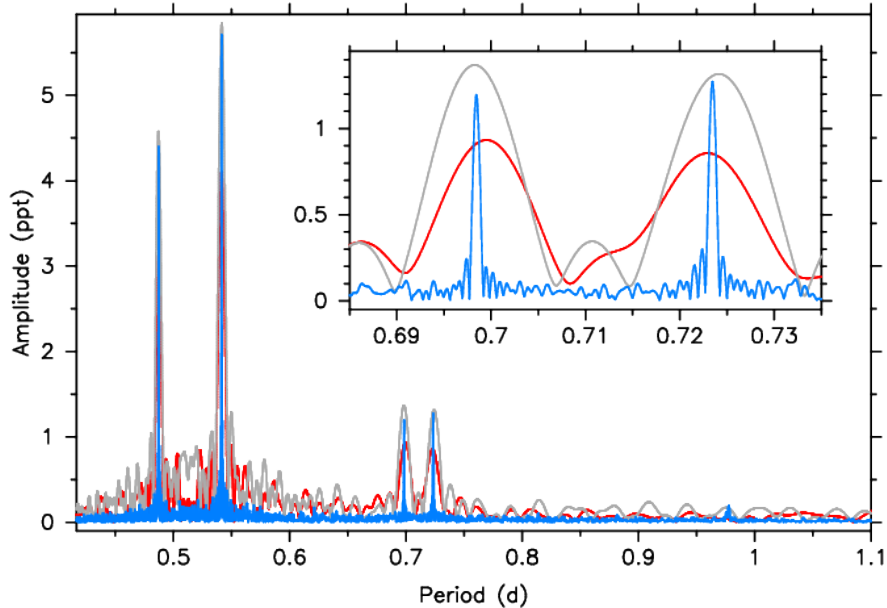


Fig. 16 Amplitude spectrum of the γ Dor g-mode pulsator KIC 8645874 (V mag of 9.9) plotted as a function of period. Blue: periodogram deduced from the *Kepler* light curve covering 684 d, red: periodogram from TESS data covering 54 d; grey: periodogram for an excerpt of the *Kepler* data with a time base of 54 d. The dipole prograde modes deduced from the blue periodogram reveal a period spacing value of 2322 s (or 0.026876 d) as can be seen in the inset. This observational diagnostic gives direct information on the internal rotation and buoyancy frequencies of the star (Van Reeth et al, 2016). PLATO is anticipated to deliver a g-mode periodogram similar to the blue one should the star be observed by all 24 normal cameras.

5.3 Example 1: g-mode asteroseismology

We highlight the major asset of PLATO-CS for the domain of gravity-mode (g-mode) asteroseismology, which got kick-started by the CoRoT mission with the discovery of period spacing patterns due to high-order g modes in the B-type dwarf HD 50230 (Degroote et al, 2010). While the 5-month CoRoT light curve was sufficient to discover the g-mode pattern of this slowly rotating pulsator, the g modes must be measured during at least two years to derive values for the internal rotation and mixing of rotating dwarfs. The real start of this science case thus came from the *Kepler* mission, whose 4-year light curves allowed for the development and application of g-mode asteroseismology along the main sequence. This meanwhile led to the internal rotation rates near the convective core in ~ 700 dwarfs covering the mass range from 1.3 to $9 M_{\odot}$ (see Aerts, 2021, for a summary). PLATO-CS will be able to rely on light curves of 2-year duration, according to the current baseline observing scenario. This suffices to embark upon g-mode asteroseismology for a wide variety of masses, metallicities, and evolutionary stages, opening up asteroseismic probing of stars that will eventually explode as supernova as well as the most massive exoplanet host stars outside of PLATO's core science. PLATO's 2-year time base is critical to achieve this.

The PLATO-CS potential for g-mode asteroseismology of exoplanet hosts is illustrated in blue in Fig. 16, which shows the Fourier transform in the form of a periodogram for the 684-d *Kepler* light curve of the γ Doradus pulsator KIC 8645874. This young intermediate-mass early-F type star has an effective temperature of 7240 ± 90 K, $\log g = 3.88 \pm 0.27$, $v \sin i = 21.4 \pm 0.9 \text{ km s}^{-1}$ and solar metallicity (Tkachenko et al, 2013). It was discovered to be a dipole prograde g-mode pulsator with an asteroseismic mass determination of $1.52 \pm 0.02 M_{\odot}$. The star is found to rotate quasi-rigidly with a rotation period of ~ 2.7 d, which is about 5 times slower than the period of its dominant dipole g mode shown in Fig. 16 (Van Reeth et al, 2015; Mombarg et al, 2021).

Figure 16 also shows the periodogram derived from this star’s 54-day TESS light curve in red. For comparison, we show in grey the periodogram resulting from a 54-day excerpt of the *Kepler* light curve, to illustrate that the increased pixel size of TESS versus *Kepler* does not bring any contamination issues for this particular star, which has a visual magnitude of 9.92. The inset in Fig. 16 zooms in on two of the star’s g modes and reveals that the mode period precision downgrades tremendously by reducing the light curve from 684 d to 54 d (grey versus blue). It is also seen that the multiperiodic g-mode beating over the years and the limited frequency resolution of a 54-day light curve imply a different shape for the red and grey periodograms. Adding the TESS 54 d curve to the 684 d *Kepler* curve essentially gives the same result as the blue curve in Fig. 16 because the addition of the 2400 TESS data points to the 30620 *Kepler* data points, having a 2260 d gap in between, is not helpful to detect more modes in this particular example.

The *Kepler* data of this star led to a derivation of the size and mass in its convective core due to internal mixing and allowed to deduce its evolutionary stage in terms of its central hydrogen mass fraction with a relative precision of $\sim 10\%$ (Mombarg et al, 2021). PLATO’s 2-year light curves will deliver similar asteroseismic probing capacity to the blue curve in Fig. 16. This offers a good compromise between the 2-year duration of the light curve required to derive the internal rotation frequency along with the level of element mixing and the age, versus the number of suitable pulsators to perform g-mode asteroseismology by pointing at various positions in the sky.

5.4 Example 2: red giants and stellar ages

Step-and-stare phases of duration shorter than two years are currently not foreseen in the nominal 4-year mission, but the instrument design makes it possible to take up such an observing strategy during the extended mission (see Section §7). Such step-and-stare phases offer limited capacity for the particular science case of g-mode asteroseismology of dwarfs, as the need to unravel the period spacing values with high precision requires the staring to cover at least one to two years (cf. Fig. 16 and Garcia et al, 2022).

However, such a strategy would be optimal for other PLATO-CS topics, notably determining the age of red giant stars distributed across the Milky Way for galactic archaeology. This PLATO-CS science case is extensively discussed by Miglio et al (2017), who showed that asteroseismic age-dating of red giants at $\sim 10\%$ level requires light curves with a duration of at least 150 d. However, the internal rotation of red

giants can only be deduced from rotational splitting of their dipole mixed modes and requires a minimal duration of 2 years for the light curves, as also revealed from the detections of core rotation from *Kepler* data (Beck et al, 2012; Mosser et al, 2012).

The capacity to deduce the internal rotation and mixing properties of red giants and F-type dwarfs offers a critical tool to determine the age of PLATO’s core science exoplanet hosts at a level better than 10%. This is achieved by applying backtracking of the measured cumulative evolutionary effect via red giant models to the main sequence and by downscaling the models of γ Dor pulsators in mass (e.g., Montalbán et al, 2013). Such backtracking and downscaling of asteroseismically calibrated models will allow us to compute improved stellar models for the regime of the PLATO exoplanet hosts in the core science programme. This strategy will deliver models for the exoplanet hosts in the core science programme capable of age-dating at 10% level. The host stars themselves do not reveal oscillation modes capturing the internal rotation and mixing in the deep interior sufficiently well to achieve the required accuracy in age. For this reason, the PLATO core science calibration plan will rely on tens of thousands of red giants and thousands of γ Dor stars to be monitored during 2 years and covering proper ranges in mass, evolutionary stage, and metallicity. Of course, these red giants needed for the core science calibration then also serve for galactic archaeology as its requirements are less stringent, given that red giant age determination can already be done from ~ 150 d light curves.

5.5 Example 3: transient studies

Outbursts in accreting compact binaries harbouring white dwarfs, neutron stars and black holes hold the potential to gain crucial information on disc instabilities and accretion processes. In particular low-mass X-ray binaries display outbursts precursors in optical wavebands prior to the X-ray detections and subsequent delays in optical to X-ray emission during the onset of outbursts (Russell et al, 2019; Goodwin et al, 2020).

Outbursts from accreting white dwarf binaries of Cataclysmic Variable (CV) type have been studied for more than a century. These binaries have orbital periods ranging from ~ 5 min to half a day and contain a white dwarf accreting material from a late type main sequence star or another white dwarf. Their outbursts arise through instabilities in the accretion disc and can have timescales from a few weeks to decades.

Although there were only a dozen CVs in the *Kepler* field, the nature of the data allowed the accretion process to be studied in an unprecedented way. Dozens of normal and superoutbursts were observed from V344 Lyr which revealed positive and negative superhumps at different stages of the outburst cycle. These superhumps have periods slightly longer (positive) and shorter (negative) than the binary period and are due to a precessing and/or tilted accretion disc and whether the accretion stream impacts with the disc (Still et al, 2010; Wood et al, 2011; Osaki and Kato, 2013). *Kepler* observations of V1504 Cyg and V344 Lyr also revealed that superoutbursts are preceded by a normal outburst giving insight to the physics of superoutbursts in general (Cannizzo et al, 2012).

Since then, many more CVs and accreting binaries have been studied using K2 and TESS. As one example of a CV observed using TESS in 2-min mode, we show in

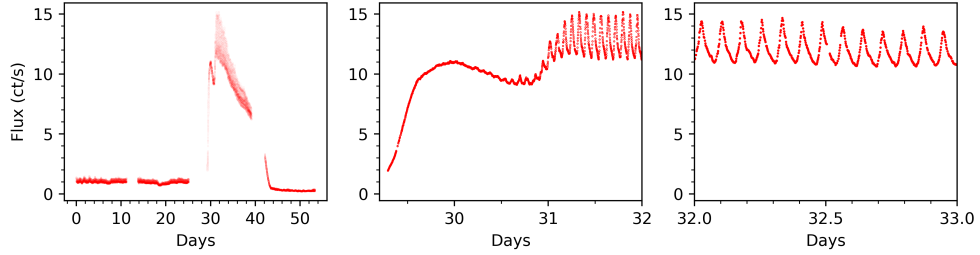


Fig. 17 A snapshot of TESS 2-min cadence observations of the CV VW Hyi made in Cycle 1 between 2019-03-28 and 2019-05-20 and showing a superoutburst. Positive superhumps are seen at the point of maximum light (middle panel); their period starts to shorten as the outburst progresses (right panel).

Fig. 17 two months of data of the CV VW Hyi. It shows a normal outburst preceding a superoutburst, with superhumps appearing at maximum brightness. The period of these positive superhumps starts to decrease as the outburst progresses. Observations such as these can be compared directly with models of superoutbursts (Thomas and Wood, 2015; Kimura et al, 2020). Other types of CVs have also been discovered to display unusual behaviour that went unnoticed using ground-based telescopes, such as the switch on and switch off of accretion in TW Pic (Scaringi et al, 2022a) and fast optical enhancements in a number of magnetic CVs interpreted as micronova events (Scaringi et al, 2022b).

PLATO-CS will allow long term observations of relatively bright CVs, or systems which are usually faint but experience rare outbursts. More importantly, the potential exists to obtain high cadence, *multi-colour* photometry over the outburst cycle from PLATO’s fast cameras. This will allow for a search for variations in colour over orbital cycles and super-humps. Observations of VW Hyi made several decades ago (van Amerongen et al, 1987) showed such colour variations can be present. PLATO-CS will also allow for the detection of longer period dwarf nova oscillations which can be used to probe the accretion process. We expect that outbursts from accreting binaries will be prime targets for pre-approved ToO observations.

6 PLATO Stellar Target Samples

6.1 Stellar Samples Definition

The PLATO mission has defined seven overall science objectives and four types of stellar samples (P1, P2, P4 and P5. P3 was dropped during mission development.). Here, we summarise the key parameters of the stellar samples (see Table 3, and Fig. 22 for a comparison to other missions).

6.1.1 The bright samples (P1 and P2)

These samples are at the core of the PLATO mission and consist of the brightest targets that PLATO will observe. Most of them will be part of the prime sample

Sample	target V mag	noise ppm in 1 h	type	# targets	sampling sec	data
P1	≤ 11	≤ 50	F5-K7	≥ 15000	25	imassettes
P2	≤ 8.5	≤ 50	F5-K7	≥ 1000	25	imassettes
P4	≤ 16		M	≥ 5000	25	imassettes
P5	≤ 13		F5-K7	≥ 245000	600	light curve
including:				$\geq 10\%$	50	light curve
				$\geq 5\%$	50	centroids
				≥ 9000	25	imassettes

Table 3 Summary of PLATO stellar sample requirements on dwarf and sub-giant targets.

forming the main body of the final ‘‘PLATO Catalogue’’. The sample P1 includes at least 15,000 dwarf and sub-giant stars (types F5 to K7), cumulative over the nominal mission, with $V \leq 11$ mag and a noise level of < 50 ppm in 1 h (see Table 3). We note that for the brighter stars in the sample ($V < 10$ mag) a noise level as low as 34 ppm in 1 hour can be reached (see Section 11). Sample P2 includes at least 1000 targets of the same type and noise performance with brightness $V \leq 8.5$. Targets in bright stellar samples observed by the normal cameras (N-CAM) are obtained with 25 sec sampling cadence.

A sub-sample of 300 stars will be observed with the two ‘‘fast’’ cameras (F-CAM) with 2.5 sec cadence, providing ‘red’ and ‘blue’ colour information. We note, however, that the F-CAMs cover only part of the central FoV of the normal cameras.

For all targets in the P1 and P2 samples, imassettes consisting of a small cut-out image of the respective targets of configurable size (typically 6×6 pixels) will be obtained and down-linked to ground without on-board pre-processing (see Section 6.2 for a discussion of the share of data on light curves versus imassettes).

The P1 and P2 samples are bright enough to determine the prime planetary parameters mass, radius and mean density in a wide range of systems, including terrestrial planets in the habitable zone of solar-like stars. Host stars are bright enough for asteroseismology. Table 4 illustrates the expected performance for planet characterisation for different noise levels and samples (see also Section 11). Known eclipsing binaries will be part of the sample (also of P5), after a revision of their suitability for the potential detection of circumbinary planets.

We expect a sample of > 100 (goal: 400) exoplanets characterised for their radii with better than 3% accuracy when their host stars are brighter than $V = 10$ mag, and better than 5% radius accuracy for host stars brighter than $V = 11$ mag. Their masses are expected to be determined with an accuracy of $\sim 10\%$. This planet sample will span over a wide range of physical sizes and mean densities, including > 5 (goal: 30) (super-)Earths in the habitable zone of solar-like stars. See Section 3.1.2 for an analysis of the expected PLATO planet yield and a comparison to other missions.

Asteroseismic measurements will be performed for $> 5,000$ stars in the bright samples to obtain precise ages of planetary systems. Asteroseismic modes can be analysed with high precision to improve stellar models. This is expected to result in a sample of > 100 (goal: 400) bright planetary host stars with accurate ages ($\sim 10\%$). This data set is therefore of fundamental importance for the mission and will also be used to e.g. calibrate classical age determination methods applicable to hosts which

noise ppm/sqrt(1h)	sample	performance for solar-like hosts
34	P1, $V \leq 10$ mag	3% r_p , 10% age
50	P1, $V \leq 11$ mag	5% r_p , 20% age
80	P5, $V \leq 12$ mag	detection of 1 R_{Earth}

Table 4 Overview of expected performance for different samples and noise levels.

do not allow for asteroseismic investigation.

6.1.2 The "M dwarf sample" (P4)

This sample is dedicated to survey cool late-type dwarfs (i.e., late K to M dwarfs) in the solar vicinity and shall include at least 5000 objects with $V \leq 16$ mag monitored during long pointings.

6.1.3 The "statistical sample" (Sample P5)

At least 245000 dwarf and subgiant stars (F5-K7) with $V \leq 13$ mag are observed in this sample, cumulative over at least two target fields. For most of these targets, stellar light curves are computed on-board the satellite. The final sampling of these light curves will then be 600 sec. However, the data volume allows for some of the P5 targets, e.g. the brightest ones in this sample or targets of special interest, to be transmitted to ground as imagerettes, see discussion below. For stars with light curve noise levels better than 80 ppm in 1 hour we expect that detection of Earth-sized planets around solar-like stars will still be possible in the P5 sample, even if their bulk parameters cannot be characterised with the same accuracy as for the P1/P2 samples.

The "statistical sample" will be used for, e.g., planet frequency determinations, studies of planet parameter correlations with stellar parameters or with the environment of planetary systems. We expect >4000 (goal: 7000) planets with well determined orbital parameters. For >100 (goal: 400) of them, orbiting bright stars, accurate masses will be determined via RV. In addition, mass determination from TTVs will provide upper mass limits for suitable systems. We note, however, that the majority of targets in the statistical sample will be too faint for large-scale asteroseismic analysis and RV follow-up activities with highest precision.

6.1.4 The "prime" sample

A "prime sample" of up to 20000 targets will be selected out of the above stellar samples, supervised by the ESA PLATO Science Working Team (SWT), for observations with highest accuracy and will be treated with highest priority throughout the mission. Level-2 and Level-3 data products for the "prime sample" will form the core of the final "PLATO catalogue" consisting the final planet and stellar parameters derived by the mission.

Data product	UC1	UC1	UC2	UC2
	#/pointing	#/mission	#/pointing	#/mission
24 x N-cameras/12 N-DPU				
imagettes (36 pixels, 25s sampling)	22000	44000	41300	82600
light curves (600s sampling)	147000	294000	97210	194420
light curves (50s sampling)	62700	125400	62700	125400
Centroids (50s sampling)	7400	14800	7400	14800
background (25s sampling)	6000	12000	6000	12000
2 x F-cameras/2x F-DPU				
imagettes (36 pixels, 2.5s sampling)	325	650	325	650
background (2.5s sampling)	100	200	100	200
fine guidance data (2.5s sampling)	40	80	40	80

Table 5 Examples (use cases, UC) of possible shares between imagettes and light curves. Numbers are given per pointing for the whole FoV and over the mission assuming 2 pointings in total (current baseline).

The prime sample with targets in the first long pointing sky field will be defined nine months before launch and updated six months before every satellite sky field pointing. The PMC will organise ground-based follow-up observations to confirm the planetary candidates for this sample and measure the mass of the planets via its Ground-based Observing Programme (GOP).

The Science Management Plan grants the PMC proprietary rights over a small, pre-defined set of a maximum of 2000 targets in total over the 4 years of nominal mission duration. These targets will be selected using the first three months of PLATO observations of each field. From the Prime sample stars with brightness $V \leq 11$ for each sky field, the stars belonging to the lowest quartile (25%) of the noise distribution will be identified. The PMC proprietary targets will be 25% of these, with the condition that they will have a noise distribution similar to that of the original sample.

6.2 Light curves versus Imagettes

The processing and telemetry resources of PLATO easily cover the needs of the science requirements concerning the number of imagettes and light curves as outlined in Section 6.1. It is, however, not possible to transfer imagettes for all PLATO targets to ground. Therefore a choice has to be made on how to distribute the resources between further imagettes and on-board processed light curves. Table 5 shows two examples of such possible "use cases (UC)". The final choice will be made once the target fields and guest observer programs are selected.

Let us have a look at the two examples to illustrate the capabilities of PLATO. The Table 5 assumes a homogeneous distribution of targets over the field of view and the maximum capabilities of the data processing system at camera level. In UC1 22,000 imagettes with 25 s sampling rate have been allocated per pointing. With two target fields, therefore, 44000 imagettes can be obtained. This number has to be compared to the requirements for the mission, which include at least 16000 imagettes for P1+P2, at least 9,000 imagettes in P5 and optionally additional imagettes for the P4 sample, adding to 30,000 required imagettes. The 44000 imagettes allocated here therefore include a substantial number of additional imagettes. This use case also foresees resources for 147,000 light curves per pointing with 600 s sampling. Assuming

again 2 pointings over the course of the mission, this is much more than the required P5 sample size. In addition, resources have been devoted to light curves with higher sampling rates, centroids and housekeeping data, and calibration data. It is therefore an example where on-board light curve processing is maximised.

UC2 illustrates another option, aiming at maximizing the number of imagerettes. In this case 41300 imagerettes/pointing have been allocated. In addition, more than 97000 light curves with 600s/pointing are possible, plus the additional sampling rates and housekeeping budgets. These values are indicative and can vary by about 10% depending, e.g., on the targets chosen.

Table 5 also includes a budget for the two fast cameras. We will obtain 325 imagerettes with 2.5 s sampling rate per pointing from the F-CAMs, resulting in 650 imagerettes of the brightest stars over the mission (assuming 2 pointings). In addition, a budget of 40 targets is maintained for fine guidance.

The final distribution and absolute numbers of imagerettes and light curves observed by PLATO will depend on the distribution of stars in the field of view, the data processing prioritization chosen by the ground segment, the in-flight performance of the instrument, and the system-level margins released after final development. The numbers in Table 5 serve as illustration for the sizing of the design.

We note that it is in principle possible to change during science operations from imagerette to light curve mode, and vice versa, for a given target. This is however subject to the operational planning cycle and will be addressed on a case by case basis depending on the resulting impacts on mission performance due to observational gaps. The same applies for changing/adding targets during science operation phases.

In conclusion, the requirements for target samples sizes recalled in the previous subsection from PLATO’s Science Requirement document are well within the instrument telemetry and computing resources. The share between transmission of additional light curves and/or imagerettes has to be defined once the target stars are selected.

7 Target Fields and Observing Strategy

PLATO is a wide-field instrument whose field-of-view (FoV) covers 2132 deg² on the sky (see Section 13). For comparison, the *Kepler* mission FoV was 115 deg² (Koch et al, 2010), and the TESS satellite FoV covers 2300 deg² (Ricker et al, 2015), while CoRoT covered a square of 2.8x2.8 deg² (Auvergne et al, 2009). For illustration purposes, Fig. 18 shows approximate PLATO field positions on the sky in comparison to *Kepler*/K2 (K2 being the extended use of the Kepler satellite (Howell et al, 2014)) and CoRoT mission fields.

PLATO will be launched into an orbit around the L2 Lagrangian point. The cruise and commissioning phases after launch can take up to 90 days. The duration of the nominal science operation phase of PLATO is then planned for 4 years. Extensions of the mission science operations are possible as the satellite has been designed with consumables for up to 8.5 years (see Section 12). For the design of the spacecraft, on-ground operations and mission performance studies, a set of baseline assumptions concerning the science observing strategy have to be made. The assumed baseline

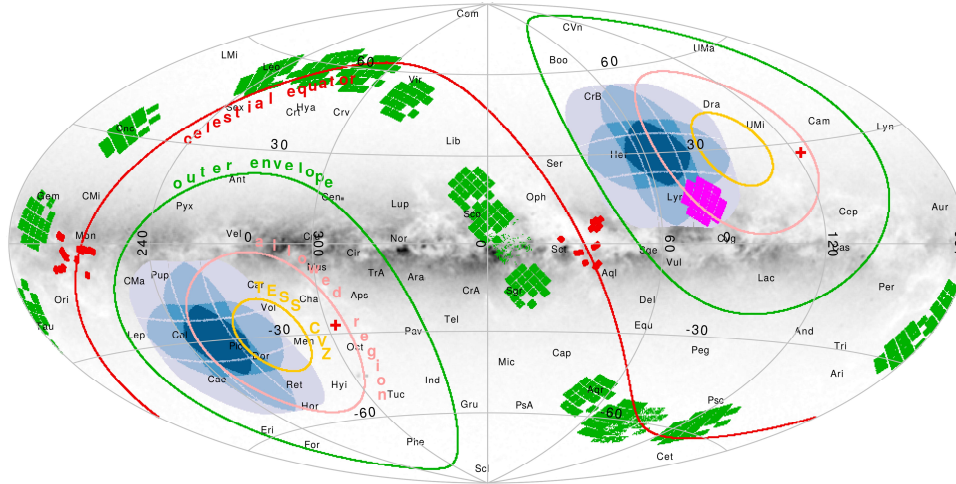


Fig. 18 Illustration of PLATO FoVs (blue) in comparison to *Kepler* (pink), K2 fields (green) and CoRoT mission fields (red). Lines indicate the TESS viewing zones. The position of the PLATO fields is indicative only (figure re-produced from [Nascimbeni et al 2022](#)).

observing scenario therefore splits the 4 years science observation phase into 2 observing blocks of 2 years each, so-called long-pointings (LOPs). Alternative scenarios are possible, e.g. a longer field of 3 years duration followed by a phase of shorter step-and-stare pointings (SOPs). Another possible scenario would be, for example, to stare at one field only for the whole science operation phase. The spacecraft provides the technical flexibility to choose from such scenarios, and even adapt the strategy during the science operation phase if needed.

The PLATO Input Catalogue (PIC) for first pointing of the satellite must be defined by ESA's PLATO SWT at the latest 2 years before launch. An update is planned for 9 months before launch, including the definition of the so-called "prime sample" (see Section 6). The subsequent target fields and their "prime sample" members are defined 6 months before the start of each field. Once this mission is completed and in case an extended mission is granted, another evaluation for key regions which would deserve dedicated PLATO pointings can be made, unless extended observations of already covered fields are given priority.

PLATO target sky regions are constrained by the mission science requirements defining the stellar samples to be observed (see Section 6) as well as technical constraints (e.g. Sun avoidance angles). In fact it turned out that due to the large field

	LOPS2	LOPN1
α [deg]	95.31043	277.18023
α [hms]	06:21:14.5	18:28:43.2
δ [deg]	-47.88693	52.85952
δ [hms]	-47:53:13	52:51:34
l [deg]	255.9375	81.56250
b [deg]	-24.62432	24.62432
λ	101.05940	287.98162
β	-71.12242	75.85041

Table 6 Coordinates of two long pointing target fields of PLATO (Nascimbeni et al., in prep.). LOPS2 has been selected by the SWT as the first target field of the mission.

size and the requirement for long pointings, the possible sky target regions are constrained rather well. In a first step, stellar properties meeting the requirements of PLATO samples were investigated to produce an all-sky version of the PLATO Input Catalogue (PIC, [Montalto et al, 2021](#)). In a next step, [Nascimbeni et al \(2022\)](#) presented the identification of possible sky regions for PLATO’s Long Pointings, taking into account technical boundary conditions, Gaia data and simulated signal-to-noise ratios for targets in these regions. First two provisional LOPs were presented, one for each hemisphere ([Fig. 18](#)).

Meanwhile the final choice of two long pointing target fields has been made ([Table 6](#)), see [Nascimbeni et al. in prep.](#) for details on the selection and field properties. It turns out that both fields (north and south) meet the science requirements for the P1-P5 sample equally well. The choice of the first field was therefore made based on the availability of ground-based facilities for radial-velocity follow-up, in particular to provide masses for small planets. As a result of this assessment, the ESA PLATO SWT decided to start observations with the southern field (LOPS2).

8 The PLATO Science Ground Segment: Data Products and Releases

8.1 Generation of the Data Products

The PLATO Science Ground Segment (SGS) is in charge of the validation, calibration, and processing of the PLATO observations to generate the PLATO science data products. The SGS encompasses the PLATO Science Operations Centre (SOC) under ESA and the following entities within the PMC: the PLATO Data Centre (PDC), PLATO Science Management (PSM), and the PMC Calibration/Operation Team (PCOT).

The scientific specifications for the on-ground software for generating the data products are provided by the PSM, which benefits from extensive expertise from the European scientific community. These specifications account for the lessons learned from CoRoT, *Kepler*, K2, CHEOPS, and TESS and build on the latest advances in stellar and exoplanet sciences. During operations, the PSM will scientifically review the data processing chain and provide updated scientific specifications for algorithms

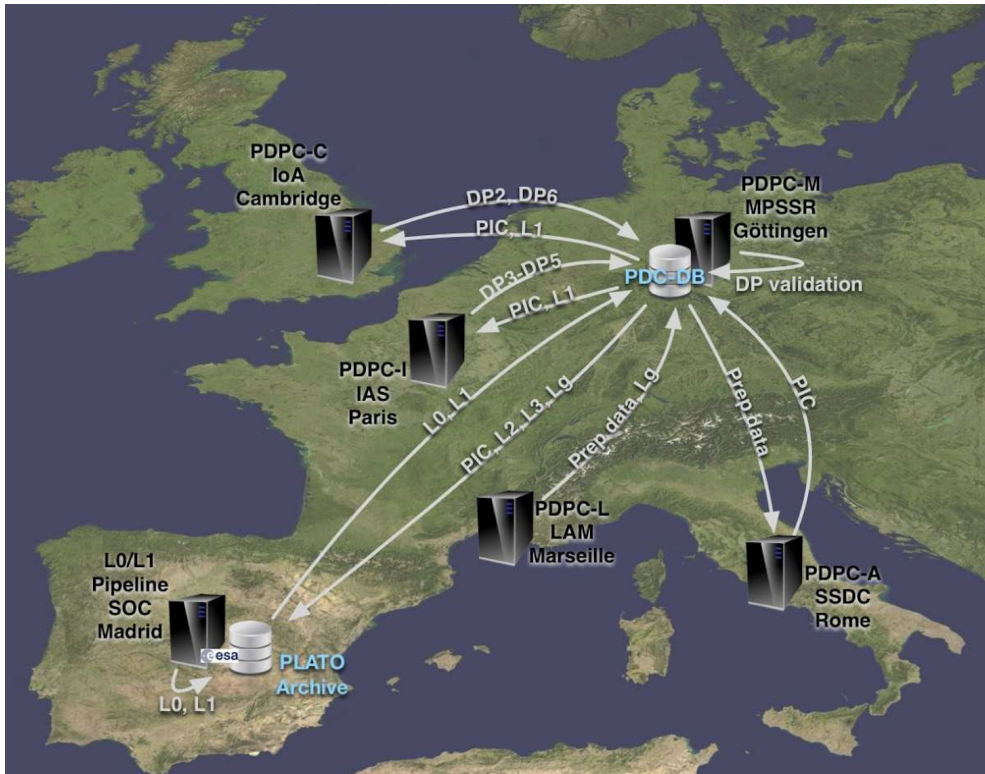


Fig. 19 Data flow within the Science Ground Segment for the processing of the PLATO science data products.

and tools where needed. For each target field, PSM provides the requirements for the PIC. PSM also includes the Ground-Based Observing Programme (GOP), which will provide the Lg Data under PSM responsibility, including the observations needed for the confirmation of the planets and the radial velocities for the determination of their masses. The PSM will also scientifically validate the final list of planets and their characteristics. The PCOT will support the calibration activities and operations, e.g. by providing input to the procedures needed for payload operation and for scientific mission planning.

The PDC responsibilities include the definition and implementation of the L1 and Calibration (CPDS) pipeline (to be run by SOC at ESAC, Spain) and the development of the software for processing the L2 and L3 data products (L3 combines L2 and Lg). The generation of the PLATO data products will be performed within two main pipelines, the Exoplanet Analysis Pipeline (EAS) and the Stellar Analysis Pipelines (SAS). These pipelines do not work independently, and several intermediate products (e.g. stellar rotation periods; transit detections) will be interchanged between them. A more detailed description of these pipelines will be provided elsewhere after finalising their design.

The PDC will include a main database system (PDC-DB, see Fig. 19) that will comprise the PLATO data products, the input catalogue, and all the preparatory data on the PLATO targets that are required for the processing of the Level 2 and Level 3 data products, in particular specifically acquired ground-based follow-up data. The PDC will generate the validated PLATO input catalogue and manage the preparatory and follow-up data. Computing resources will be distributed among five Data Processing Centers: PDPC-C for the exoplanet analysis system, PDPC-I for the stellar analysis system, PDPC-A for the PLATO Input Catalogue, PDPC-L for the preparatory and follow-up database management, and PDPC-M for running the data analysis support tools.

The ESA SOC will be responsible to carry out the scientific mission planning based on the delivered PLATO Input Catalogue and the approved Guest Observer targets and will send the payload telecommands to the ESA Mission Operations Centre (MOC) in Darmstadt, Germany. Once executed on board the spacecraft, the resulting science data dumped to ground will be provided via the MOC to the SOC.

The SOC will run the Level 0 pipeline to reconstruct the data as originally generated by the cameras on-board and will apply both a time correlation and a coordinate transformation to the data. The resulting Level 0 products are then fed into the Level 1 pipeline which uses calibration data provided from the CPDS pipeline. The L0 and L1 products will then be provided to the PDC for further processing to produce the L2 and L3 and Lg products. Both the SOC and the PDC will perform validation of the Level 0 and Level 1 data before releasing them to the science community via the PLATO Archive (PAX - hosted at the SOC) (see also Fig. 20).

8.2 Data Products

Here we explain which data products will be available to PLATO users for analysis and science. For each target object, the following will be accessible via the ESA archive center:

- Level-0: Depending on target, Level-0 data include unprocessed imagerettes or on-board pre-processed light curves and centroid curves. Level-0 data are downloaded for the respective targets from all cameras.
- Level-1: Calibrated light curves and centroid curves for all targets and cameras produced on-ground. Level-1 data include, e.g., corrections for instrumental effects and the light curves and centroid curves derived from imagerettes. In addition, for the normal cameras, camera-averaged Level-1 light curves and centroid curves are provided for each target star. For the fast cameras, no average light curves are produced, so that the colour information is preserved.
- Level-2: First scientific data products. Concerning exoplanets, Level-2 data include the transit candidates and their parameters, planetary ephemeris of the system, depth and duration of the transit, estimated radius, and their corresponding uncertainties. For planets with detected Transit Time Variations (TTVs), the resulting list of TTV planet parameters will be provided.

For the target stars, Level-2 data include the results of the asteroseismological analysis, and their corresponding uncertainties. When possible, the stellar rotation periods and stellar activity properties inferred from activity-related periodicities in the light curves are provided, as well as the seismically-determined stellar masses, radii and ages of stars, obtained from stellar model fits to the frequencies of oscillation.

- Level-3: The final "PLATO Catalogue", including the list of confirmed planetary systems, fully characterised by combining information from the planetary transits, analysis of the planet-hosting stars, and the results of ground-based observations. The confirmation of the planets relies on the Lg ground-based follow-up data.
- Lg, ground-based observations data: These data include the results of the PLATO ground-based campaigns, e.g., observations for filtering false planet transit detections and spectroscopy to determine planetary masses.

In addition, housekeeping and auxiliary data, like, e.g., pointing information and quality control data will be available with all data product levels.

8.3 Data Releases

The PLATO data releases have been defined as a function of the product levels described in the previous section and of four observing target groups. The following target groups have been considered: (i) Prime sample (see definition in Section 6); (ii) non-Prime sample; (iii) PMC proprietary targets; (iv) targets proposed by the Guest Observers. Figure 20 illustrates the release of PLATO data for groups (i) to (iii) as described below. The data rights and releases corresponding to the guest observer's programme will be outlined in Section 10.

The timeline for the releases of Level-0, Level-1, and Level-2 products has been specified with a cadence of three months. This is the time interval between two 90° rotations of the spacecraft, which are necessary to keep the adequate orientation with respect to the Sun. After each three months data acquisition period, three months will be required for the validation of the Level-1 products by the Science Operations Centre and by the PMC. Exceptionally, six months will be needed for Level-1 product validation of the first three months of nominal mission data. This longer validation period is justified because the data pipelines are expected to undergo the most important updates, resultant from the system calibration and characterisation with the first on-board data.

For the 20,000 prime sample targets, Level-0, Level-1 and Level-2 products for each observing quarter will be publicly released via the ESA PLATO Archive (PAX) as soon as possible after the Level-2 product scientific validation, but no later than one year after the three month Level-1 product validation period. This will allow for the consolidation of the planet candidate list and the initiation of the ground-based observations by the GOP Team(s).

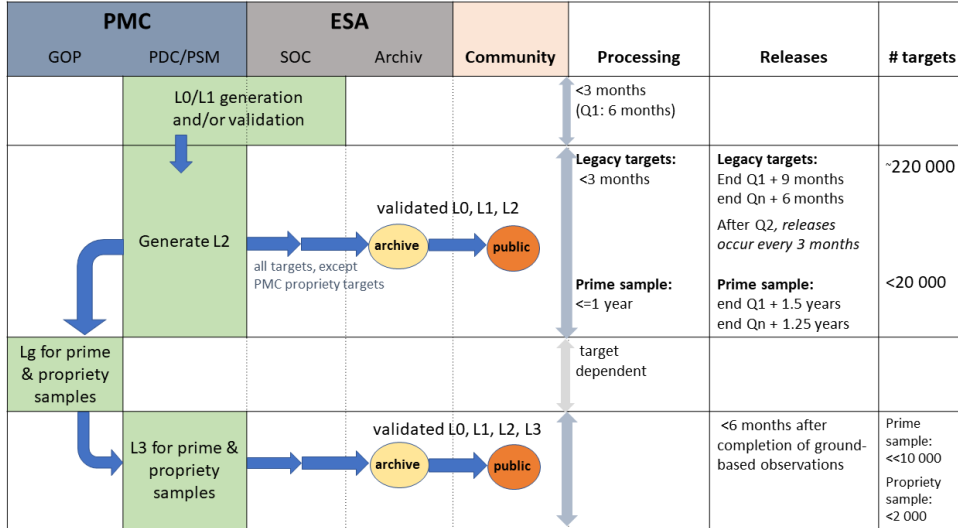


Fig. 20 Illustration of the data release strategy of PLATO. Number of targets are estimates and refer to a baseline observing strategy of 2 long field pointings.

For the $\approx 24,000$ non-prime sample targets, Level-0, Level-1 and Level-2 products for each observing quarter will be publicly released within three months of the corresponding Level-1 product validation period.

The mission Science Management Plan establishes that the Level-3 and Lg products of the prime sample targets are a deliverable to the community. In this regard, it is required that the Level-3 and Lg data of these targets be publicly released immediately after the publication of the planetary parameters, or as soon as possible, but no later than six months after the completion of the ground-based observations. Ground-based observations data for prime sample targets that are not confirmed to be planets, will also be made publicly available in the PAX as soon as possible, but no later than six months after the ground-based observations for each target have been performed.

The proprietary period for each proprietary target allocated to the PMC will end six months after the completion of the ground-based observations for the confirmation and characterisation of the associated planet. The proprietary period will finish in any case at the end of the mission post-operations phase.

9 The Ground-based Observations Programme

The Ground-based Observation Programme (GOP) within the PMC will play an important role for the PLATO mission: it will be in charge of organising the ground-based observations needed to confirm the planetary nature of PLATO transit candidates. PLATO follows a strategy first established by the CoRoT mission by setting up a coordinated approach to ground-based follow-up managed by the mission

consortium in order to secure sufficient resources and efficient planning of ground-based activities.

The PMC will establish and manage the GOP team with contributions from international partners taking part in the follow-up. The GOP Team will respond to calls issued by ground-based facilities (e.g., ESO) to grant observing time for the confirmation and characterisation of the candidates in the “prime sample” (see Section 6). Dedicated facilities taking part, e.g., in the filtering process of planet candidates will also contribute to PLATO. A key planet parameter for the confirmation and characterisation of planets is their mass, which can be determined by means of high-resolution spectroscopic observations providing precise radial velocities. But additional photometric and low-resolution facilities will as well be useful to discard false positive scenarios.

Within the GOP team tools are being created to interface to the database of PLATO candidates for the filtering of candidates to detect astrophysical mimics and the subsequent radial velocity follow-up of the planet candidates. For each object, observations will be optimised to exploit the available resources. Facilities taking part in the GOP will also have to demonstrate their performance accuracy and hence the observations that they can be most efficiently deployed to carry out. The GOP also has significant data quality control measures to ensure that only data of sufficient quality is used in the decision making process and eventually in the system modelling.

The GOP is also responsible for gathering any preparatory observations being attempted (e.g. detailed spectroscopic observations of the PLATO stellar samples). For target samples beyond the propriety and prime samples, the GOP will perform and support preparatory and follow-up observations on a best effort basis and provide, together with the PDC, an interface to data obtained on PLATO targets by the general community.

10 The Guest Observer Programme

The PLATO Guest Observer (GO) programme will allow all interested groups and individuals to submit proposals to observe targets which are not included in the PLATO prime sample (see Section 8.2) and have science goals which are not covered by the PLATO core science objectives. Examples of complementary science cases which could be addressed via the GO programme are discussed in Section 5. An average of 8% of the science data rate (excluding calibration data), averaged over the mission lifetime, will be allocated to the GO programme. This will allow for an extended complementary science programme, while preserving the resources for an optimal observation of the core science targets. The total number of GO objects that may be observed with this allocation will range from thousands to tens of thousands, depending on the sampling times and whether imagettes or light curves are requested. ESA will appoint an independent Time Allocation Committee (TAC) for the evaluation and selection of the proposals based on scientific merit.

GO targets would have to lie within the pre-defined PLATO sky fields. The first call for GO proposals will be issued by the ESA SOC nine months before launch and after the publication of the PIC and selection of the prime sample. The call will

include tools which will allow potential users to predict the signal-to-noise for a range of spectral type and class of object. More calls are expected to be issued during the mission (once per year, to be confirmed).

GO programmes can contain targets that are part of the PIC, but not of the prime sample. For targets in common with the PIC, access to the associated Level-0 and Level-1 products will be granted with the condition that the observations are exclusively used in relation with the science objectives of the proposal. Exploitation for complementary science of non-public PIC target data will only be carried out through approved GO programmes.

In addition to the science done by the successful GO applicants, a general variability classification will be performed on all PLATO data once they are released publicly. This probabilistic classification will be based on applications of supervised and unsupervised machine learning methods, resulting in an electronic public PLATO variability catalogue, which will be updated regularly as new data will be released to the worldwide community.

GO programmes can also include on a best effort basis the observation of Targets of Opportunity (ToO). These may contain objects which can be identified in advance but which undergo unpredictable changes (e.g., recurrent novae), as well as objects that can only be identified in advance as a class (e.g., novae, supernovae, tidal disruption events, gamma ray bursts). The identification of ToOs shall come from the GO programme. For ToOs that cannot be anticipated, proposals may be submitted at any time during the mission. The TAC will prioritise ToOs with respect to on-going GO programmes, to permit the interruption of lower priority targets observations if required by the ToO. ToOs can be observed with the constraint that the reaction time between triggering the ToO and the start of the observation will be in line with the ongoing mission planning cycle, with execution of ToOs being performed on a best effort basis. The baseline planning cycle during nominal mission foresees interaction once per month.

Level-0 and Level-1 products for all PLATO observed targets, including the GO programme observations, will be generated by the ESA SOC. The proprietary period of the targets selected through the GO programme call will be one year, starting at the time of the delivery to the Guest Observer of the last portion of the relative Level-1 data. During the execution of the observations, the SOC will deliver Level-0 and Level-1 products to the PI of the GO programme observer every three months. ESA will require the GOs to provide their data and results, to make them accessible through the PLATO Archive.

11 Expected Instrument Performance

The design of the PLATO mission is driven by the need to obtain a core sample which is dominated by stellar flux white noise and where instrumental effects play only a minor role. Although the nominal mission operation time is 4.25 years at this point, the payload is designed to maintain a level of performance that allows the science objectives to be achieved up to an extended mission end-of-life (EOL) of 6.5 years. The EOL scenario assumes that up to two cameras could be lost during the mission

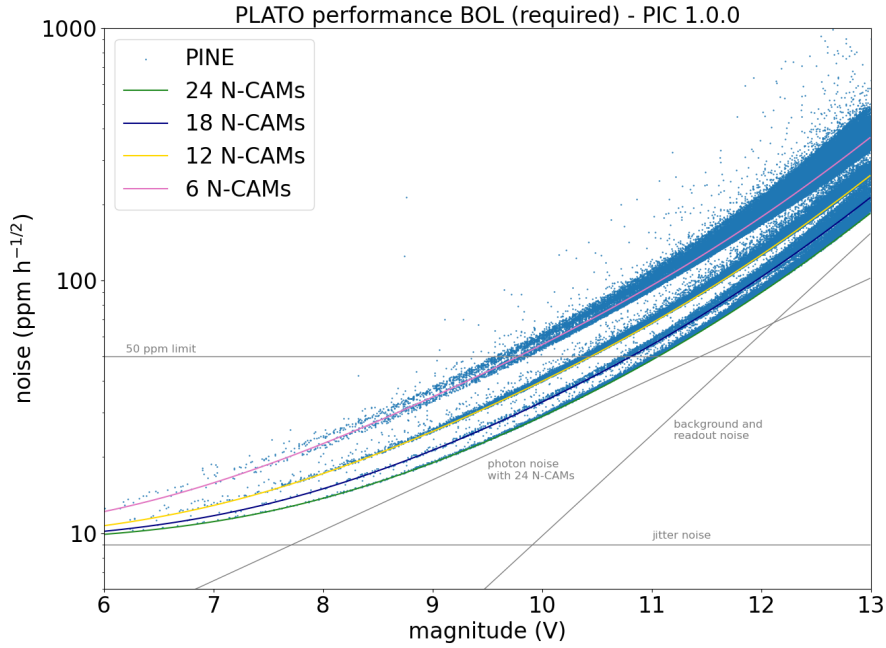


Fig. 21 Expected PLATO noise performance calculated with the PLATO Instrument Noise Estimator (PINE, Börner et al. in prep.). The values refer to beginning of life scenario (BOL). The stellar counts and properties are taken from the PIC 1.1.0. A simple noise model (including jitter, photon noise, and readout and background noise) provides a good approximation to the expected in-flight performance of the mission. The 50 ppm level is the limiting value for the P1 and P2 samples.

due to technical failures. This number results from a reliability analysis performed during the design phase.

In order to derive realistic instrument performance estimates, a full simulation of the PLATO payload and satellite behaviour has to be made. A number of simulators have been developed for this purpose each focusing on various aspects of the mission. The consortium’s primary simulator is PlatoSim (Janssen et al, 2024). It is an end-to-end camera simulator at pixel level taking into account detailed instrumental noise properties as well as realistic stellar variability, producing time series of imagerettes as well as light curves. Complementary to PlatoSim, a light curve simulator (Samadi et al, 2019) has been developed, which models the variability in the Fourier domain, and then converts it to a light curve.

At the time of writing this paper, instrument requirements for PLATO have been settled and a number of simulations of the expected instrument performance have been performed. Figure 21 illustrates the importance of different instrumental noise sources for PLATO (see Börner et al. in prep.). Throughout the main target magnitude range of PLATO (8 mag to 11 mag) photon noise dominates the signal over instrumental

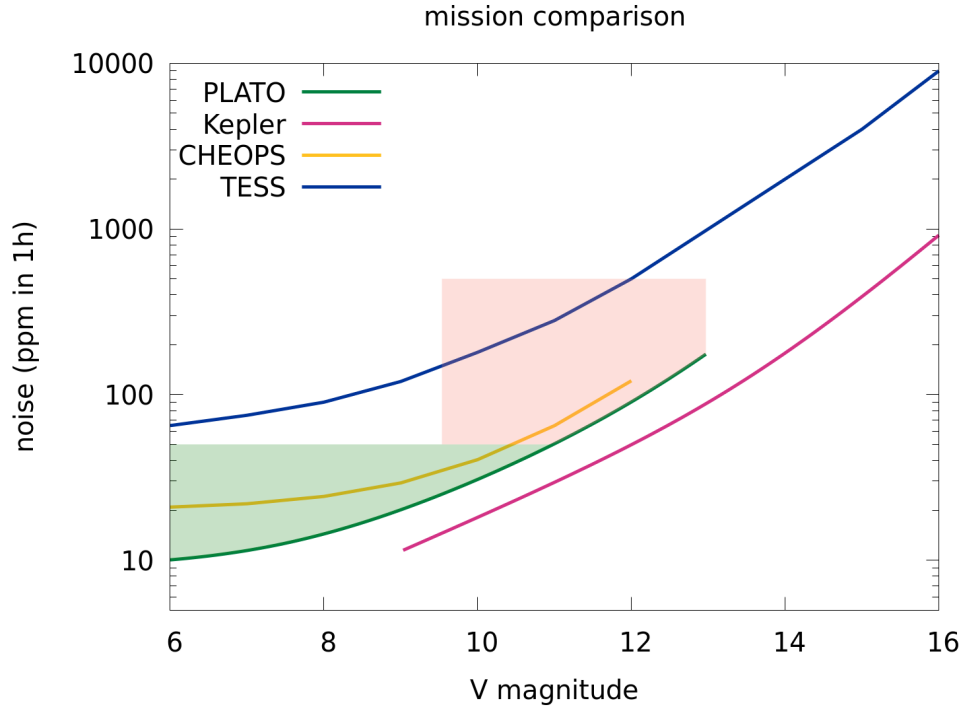


Fig. 22 Comparison of the noise levels expected for PLATO with other missions. The approximate parameter space for PLATO samples (green: P1, red: P5) is indicated for illustrative purposes. The values for *Kepler* are taken from [Van Cleve and Caldwell \(2009\)](#), the values for TESS from [Sullivan et al \(2015\)](#), the values for CHEOPS from the online exposure calculator (<https://cheops.unige.ch/pht2/exposure-time-calculator/>). They should be understood as reasonable approximations of the performance of each instrument and not used as reliable estimators for an individual target, as described in the different publications where the values are extracted from.

effects. At the very bright end, jitter noise from the satellite dominates. Below about 12.5 mag electronic read-out noise starts to dominate.

Stars brighter than magnitude 8 will saturate with the N-CAMs (brighter than 4.5 with the F-CAMs). However, it shall be possible to extract precise photometry from saturated targets. For slightly saturated stars (around magnitude 8) no extension of the nominal window of 6x6 pixels will be necessary. For moderately saturated targets (between magnitudes 4 and 8) saturated star descriptors are needed with the N-CAMs while smearing photometry will be possible with the F-CAMs. Finally, for the few highly saturated targets (expected 10 per camera) smearing photometry is technically possible, but alternatives are being considered (e.g. [White et al, 2017](#)).

The noise-to-signal simulator PINE (Börner et al. in prep) is using the current best knowledge of the instrument design. PINE values were used, e.g., for the development of the PIC. The detailed simulation of stellar noise-to-signal ratios (NSR)s across the PLATO FoV is shown in Fig. 21 versus stellar magnitude. As can be seen, the required

P1 noise performance of 50 ppm in 1 hour is met in the center of the FoV (24 cameras) for stars brighter than 11 mag. At the corners (6 cameras) the same performance is reached for stars brighter than 10 mag. Overall, when applied to real sky fields, the noise performance of PLATO is sufficient to provide the required number of stars in the respective P1 to P5 samples.

Of course, the particular design on PLATO with 24 overlapping cameras asks for a more detailed simulation taking into account the real geometry of the PLATO FoV. The PLATO stellar noise budget depends not only on the position of target stars in the field, hence the number of cameras, but also on the variations of the point-spread-function (PSF) across the FoV of each camera. These effects will be considered in future studies.

To put PLATO into perspective with other transit detection missions, Figure 22 shows the expected noise level of PLATO with respect to CHEOPS, TESS and *Kepler*/K2. For illustration purposes the main planet detection ranges for PLATO P1 and P5 samples are indicated as well as the main planet detection magnitude range of *Kepler*/K2. PLATO's sensitivity is better than TESS and CHEOPS, but below *Kepler*/K2 as expected from the respective aperture sizes of these missions. However, PLATO will sample on average brighter stars than *Kepler*/K2 and will hence detect the majority of its planets around brighter stars, thereby facilitating asteroseismology and ground-based follow-up observations.

12 PLATO spacecraft and mission configuration

The requirements that drive the design of the PLATO spacecraft and the mission configuration are the transit detection and characterisation of small exoplanets in long-period orbits (≈ 1 year) around solar like stars, and the observation of stellar oscillations in planet host stars. To achieve these science goals, PLATO will perform high-precision photometric observations for periods of 2 to 4 years, that should be as much as possible undisturbed by the space environment and the platform operations. Consequently, maintenance of the thermal and pointing stabilities, while keeping the interruptions to a minimum, are key aspects of the spacecraft design and of the mission configuration.

12.1 PLATO spacecraft

The spacecraft is a 3-axis stabilised system with a launch mass of approximately 2500 kg, including consumables, a size of about 3.5 m (x) \times 3.6 m (y) \times 3.7 m (z) in stowed configuration, and a deployed wingspan of approximately 9 m (as shown in Figure 23). The spacecraft accommodates a payload of 26 cameras and its design ensures an adequate protection from exposure to the Sun.

Based on a modular architecture design, the spacecraft consists of a Payload Module and a Service Module. The Payload Module, which accommodates the cameras, is thermally and mechanically decoupled as much as possible from the rest of the spacecraft by means of a truss structure with flex joints. The module is mostly made of carbon fibre to increase stiffness and reduce thermo-elastic deformations. The Payload Module contains the Optical Bench where the 24 Normal Cameras and the two

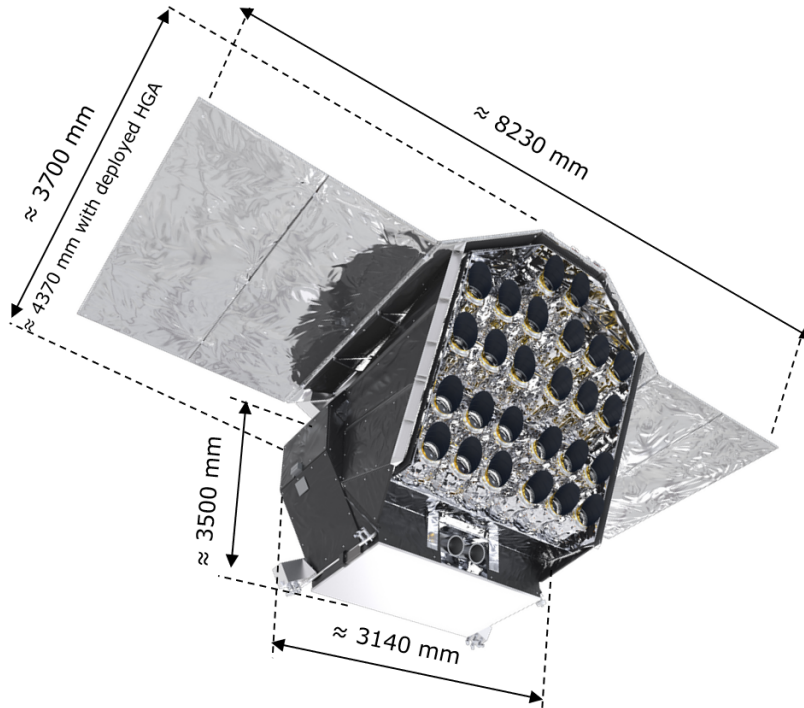


Fig. 23 Artist impression of the PLATO Spacecraft with its dimensions. Credits: ESA/ATG Medialab.

Fast Cameras are accommodated. It is integrated with the Service Module via three bipods. Additional thermal decoupling is achieved by wrapping the Optical Bench in multi-layer insulator towards the sunshield/solar array and the Service Module. This design leads to a very stable environment by clearly separating the scientific payload from housekeeping activities and other variable influences.

The Service Module (see Fig. 24) contains all the systems necessary to operate the spacecraft in the designated orbit, such as, shielding, power, propulsion, attitude control, thermal control, communication, commanding, and data management. The structure, based on a carbon fibre central tube and shear panels, provides the interface to the launcher as well as a stiff base for the payload module. The Service Module electronic units are accommodated on the bottom panels that act as radiators. A sunshield protects the cameras from the Sun, while guaranteeing an unobstructed view to space. It also carries three solar panels mounted on the spacecraft body and four deployable panels on two wings to provide the 3000 W of required power to the satellite. The satellite attitude control system is based on reaction wheels, thrusters, gyros, Sun sensors and star trackers. The thermal control system is based on heaters, radiators, and multi-layer insulation that provide the required temperatures and thermal stability to all units. This system facilitates a radiative environment to cool down the front-end-electronics units and provides the conditions to keep the low telescope

temperatures. The antenna sub-system of the spacecraft includes two fixed low gain antennas operating in X-band that guarantee hemispherical coverage when the spacecraft inertial attitude is not available from the star trackers. They are complemented with a steerable low-gain antenna (as part of the high gain antenna assembly (HGAA)) for the high X-band data rates. The downloading of the science data and the main satellite commanding is carried out via a dual X/K-band high gain antenna assembly. This enables communication for satellite control using the X-band, while the downloading to the ground of the daily 435 Gb of data uses the K-band with a data rate of up to 72 Mbps.

The PLATO spacecraft is designed and built by ESA, having as Prime contractor an industrial core team comprising OHB, ThalesAlenia and Beyond Gravity, that lead a pool of European companies.

12.2 Launch and operations

PLATO is planned to be launched with an Ariane 62 rocket by the end of 2026. Since the PLATO payload's line of sight is up-oriented towards the zenith, and blinding and illumination of the cameras by the Sun must be avoided, the strategy selected for launch and transfer includes an intermediate circular parking Low-Earth orbit. In addition, the upper stage of Ariane 62 provides a barbecue mode, such that, it can rotate around its longitudinal axis during its coasting phase, avoiding illumination of the payload. By adopting this strategy, launch is possible all year round with some exclusion windows to avoid Moon and Earth eclipses during transfer. PLATO will be injected from the parking orbit into an eclipse-free Lissajous orbit around the Earth-Sun Lagrangian point 2 (L2), located ≈ 1.5 million km from Earth. During the transfer phase, which will take about 30 days, the commissioning phase will start and will run until the check-out and calibration of the spacecraft and its payload are completed, at the latest three months after launch. At that time the routine science operations will begin with a nominal duration of 4 years. Extension of the scientific operations will be possible as the satellite is being built and verified for an in-orbit lifetime of 6.5 years and will accommodate consumables for at least 8.5 years.

The shape of the halo orbit around L2 depends on the exact date and time of launch. When PLATO is orbiting L2, the payload will be protected from the solar light by reorienting the sunshield every three months with a 90° spacecraft rotation around its line-of-sight. The orbit around L2 is maintained by regular station-keeping manoeuvres planned by the Mission Operations Centre (MOC) approximately every 28 days. During science operations, a communication session with the nominal ground station will be established several days per week. The scheduling of mission operations is strongly constrained by the required science duty cycle, which must be above 93%. This is critical to minimise the probability of missing transits of long period planets, and for the detectability of stellar oscillation modes. Furthermore, periodic observation gaps that could generate disturbing peaks in the frequencies of interest in the power spectrum of star oscillations must be avoided.

13 Payload design overview

13.1 General payload description

The PLATO payload has two major science drivers constraining its design. Compared to previous missions like *Kepler*, PLATO has been optimised to observe stars bright enough to allow radial velocity measurements on ground to complement the photometric measurements in space. Since such bright stars are relatively scarce on the sky, a very large total field of view of 2132 deg² was required. Furthermore, to be able to observe in a given target field the brightest as well as fainter stars, the instrument photon collecting area is split into 26 individual cameras. We call the 24 cameras which are used exclusively for science operation "normal" cameras and the 2 additional cameras, used also for fine-pointing on top of science operation, "fast" cameras. With this configuration PLATO will be able to obtain very stable, high precision, long-time photometric data of a large number of bright stars. Combining the information provided by the planetary transits, with the stellar data derived by asteroseismology techniques and the radial velocity measurements obtained from the ground, PLATO will provide a high-precision characterisation of the radius, mass and age of exoplanetary systems.

The data read by the CCDs of each camera are first processed by a Data Processing Unit (DPU) handling two cameras at the same time. The processed data are then transferred to the Instrument Control Unit (ICU) that finally compresses them before sending them to the spacecraft on-board mass memory for downloading to ground. The different sub-systems composing the PLATO spacecraft and payload can be seen in Fig. 24.

Table 7 summarises the main data of the instrument. Each 20 cm class camera (12 cm entrance pupil) has a total field of view (FoV) of 1037 square degrees (see [Pertemais et al, 2021b](#)). The 24 normal cameras are organised on the optical bench of the spacecraft in 4 groups of 6 co-aligned cameras each. The sky fields of the four camera groups are offset with respect to a central line of sight by 9.2 degrees, pointing towards the four corners of a square of 13.0 deg, in order to widen the total overlapping FoV of the instrument. With this approach the number of brightest stars within SNR requirements is augmented with respect to a full coalignment of the whole set of cameras. Figure 25 illustrates how many cameras observe the same part of the target field for a pointing. The total instrument field therefore is about 2132 deg² (with rounded edges). Figure 26 shows the Structural and Thermal Model (STM) of the payload during integration at OHB, ready for the qualification activities of the Payload Module.

The two fast cameras are optimised to observe the brightest stars (4 - 8.2 mag) and are part of the fine-pointing loop of the satellite. They point towards the center of the PLATO payload field of view. These two cameras provide full redundancy to secure the fine-pointing capabilities of the mission. They differ however in their entrance filter, one with a red and one with a blue spectral filter allowing for colour information on the bright targets. Thanks to a very fast readout of 2.5 s, they provide very high quality data for the Fine Guidance System (FGS) algorithm as shown in [Grießbach et al \(2021\)](#). This algorithm allows the satellite to reach the excellent pointing stability required for the different science cases detailed above:

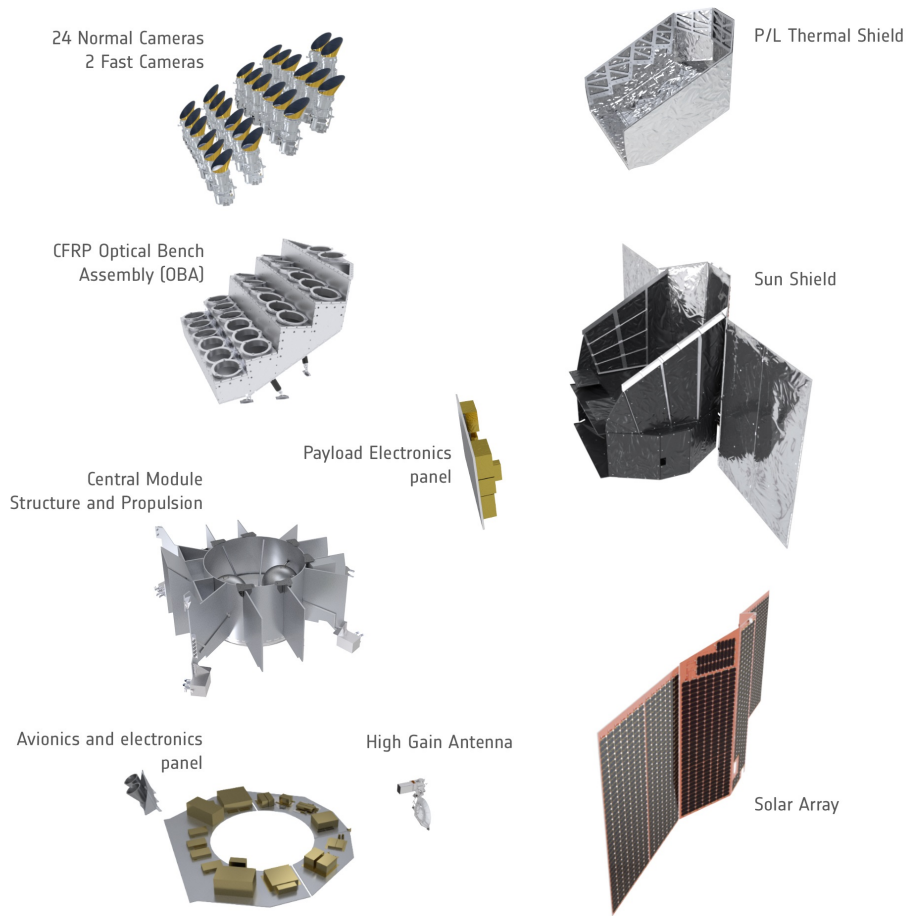


Fig. 24 Expanded artist impression of the PLATO Spacecraft showing its different modules and elements, with its 26 cameras seating on the Payload Module, and the Data Processing Units fixed below directly on the radiator. Credits: ESA/ATG Medialab

- FGS noise equivalent angle: < 0.025 arcsec around X and Y, and 0.1 arcsec around Z FGS measurement reference frame axes.
- FGS measurement bias stability: < 0.010 arcsec around X and Y, and 0.040 arcsec around Z FGS measurement reference frame axes.

13.2 PLATO Cameras

All the cameras are externally identical (except for the baffles) and their interfaces to the spacecraft optical bench are the same, with three main bipods, see Fig. 27. Mechanically, their central part is the tube of the Telescope Optical Unit (TOU), made

Table 7 PLATO Instrument parameters

PLATO Instrument	
Total Field of View	2132 deg ²
Number of cameras	26 total: 24 normal, 2 fast cameras
Normal camera groups	4, with 6 normal cameras each
Angle between camera groups	Arranged on four corners of a 13.0 degrees side square
Attitude Pointing Drift Error (PDE)	3 arcsec half cone angle over 3 months in the directional direction 6 arcsec half cone angle over 3 months in the rotational direction
Attitude Pointing Repeatability Error (PRE)	3 arcsec half cone angle in the directional direction 6 arcsec half cone angle in the rotational direction
Relative Attitude Pointing Error (RPE)	1 arcsec half cone angle over 25s in the directional direction 2 arcsec half cone angle over 25s in the rotational direction
Photometric range	4 - 16 magV
Instrument mass	< 623.15 kg
Instrument peak power consumption	< 890 W
Daily data generation	435 Gbit/day
Normal electronic chain	12 Data Processing Units (DPUs): 1 for 2 normal cameras 2 normal Ancillary Electronic Units (AEU): 1 for 12 normal cameras
Fast electronic chain	2 fast-DPUs: 1 per fast camera 1 fast AEU: 1 for both fast cameras

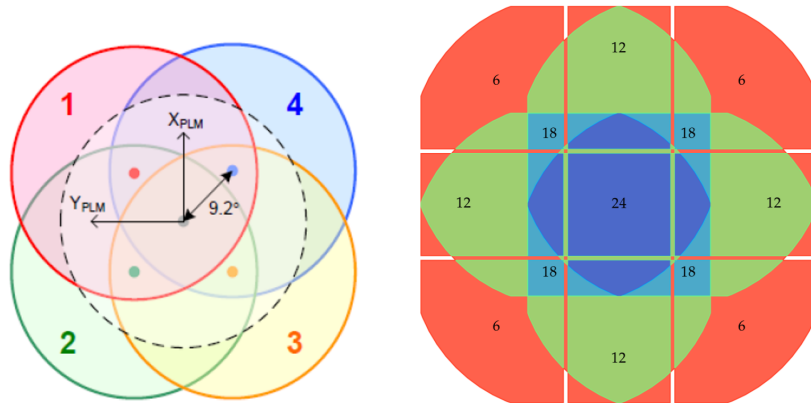


Fig. 25 Illustration of the PLATO field coverage. Left: position on the sky of the optical axis of the four groups of 6 coaligned "normal" cameras, and of the two "fast" cameras (dashed black line). Right: Number of "normal" cameras observing simultaneously the different sectors of the overall PLATO field of view. The center of the field (dark blue) is observed by all 24 cameras. At the edges (orange) only 6 cameras observe simultaneously the same field on the sky.



Fig. 26 The PLATO Payload Module Structural and Thermal Model (STM) during integration at the OHB facilities. Note the relative pointing of each of the 4 groups of 6 normal cameras, and the two fast cameras located at the top of the PLM. Credit: OHB AG.

of AlBeMet. The six lenses of the TOU are all mounted inside this tube. This tube is also the support for the baffle that acts both as straylight baffle and as a radiator for the whole camera. While the Focal Plane Assembly (FPA) with the CCDs is fixed to the TOU tube by three bipods, the Front End Electronics of the Normal Cameras (N-FEE) are mounted directly to the main interfaces of the cameras to the optical bench (the main bipods) with their own Support Structure (FSS). This allows for conductive coupling to evacuate the high-power dissipation. The Fast Front End Electronic units (F-FEE), much heavier and with a higher thermal dissipation, are however directly mounted to the optical bench of the spacecraft and have no thermo-mechanical links to the cameras (except for the CCD flexi connections).

Thermally, each camera is individually controlled by a Thermal Control System (TCS) that sets its temperature thanks to three heaters placed on the tube of the TOU. Using a Proportional-Integral (PI) controller algorithm, the temperature of each camera can be held very stable, up to $\pm 10\text{mK}$ over 14 hours using 600 s sliding window averages. Thanks to the athermal design of the camera and the AlBeMet tube properties, this temperature stability around the heaters is very well propagated to all the camera sub-systems and especially the CCDs. The other way around, the heat dissipated by the CCDs is conductively transferred directly to the baffle that can then dissipate it into cold space. This TCS is also used to fine tune the cameras focus in space and make sure that each individual camera is being used in its best possible focus position (Pertenais et al, 2021a; Clermont et al, 2018). By changing

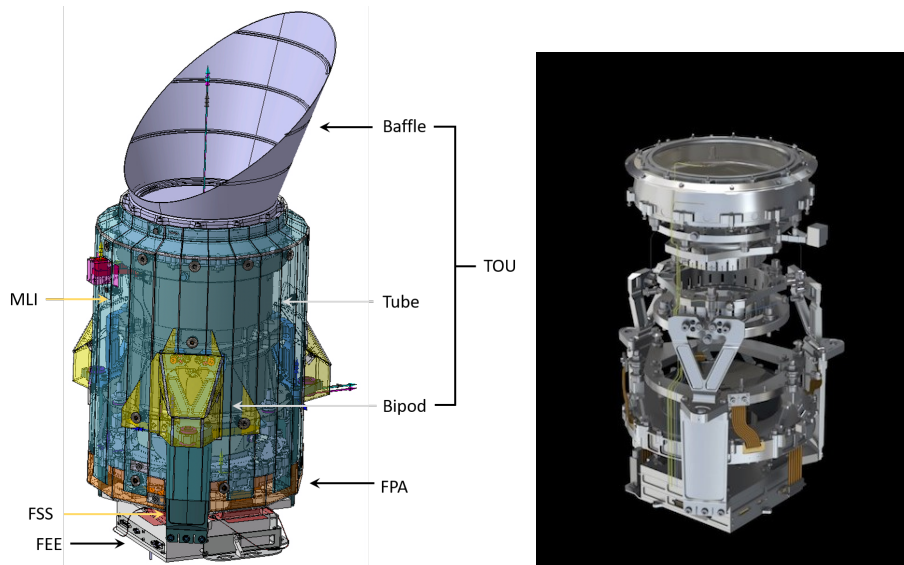


Fig. 27 CAD views of Camera with all its sub-systems. Left: Complete camera; right: Internal structure (credits: ESA/ATG Medialab).

the temperature of the camera, the characteristics of the optical system are changing leading to a slight shift of the focus. This thermal refocusing is used on-ground and then during commissioning to calibrate each camera individually to its best focus temperature. Testing under representative thermal vacuum conditions on the EM1, the first complete, flight-like camera, has shown that the best focus will be around -77°C . The precise value for each camera will be determined during the commissioning phase once in space.

The optical design of each camera (Magrin et al, 2010) consists of a six lens system with a central Calcium Fluoride lens (Bergomi et al, 2012) close to the stop, and with a first aspheric lens protected, for thermal and radiation hardness purposes, by a Suprasil window. All the optical materials have been the subject of specific radhard studies (Corso et al, 2018) and the whole design is a fine tuning balance between radiation, thermal and mass budgets (Magrin et al, 2016).

An anti-reflection coating is placed on every optical surface to maximise the optical transmission in the spectral range [500-1000] nm. Each 12 cm aperture camera has a FoV of 1037 square degrees as shown in Pertenais et al (2021b). This wide FoV is achieved thanks to a circular optical FoV of the TOU of around 18.88° radius that illuminates the 4 full-frame CCDs of $81.18 \times 81.18 \text{ mm}^2$ each on the Focal Plane Assemblies (FPA). As mentioned above, each FPA is electrically connected to a Front End Electronics (either "normal" or "fast" ones), completing the PLATO Camera. One of the FPA models used for qualification is shown in Fig. 28, with 4 full-frame (i.e. "normal" CCDs). More details on the FPA can be found in Moreno et al (2019). Table 8 summarises the the main parameters of the individual cameras.

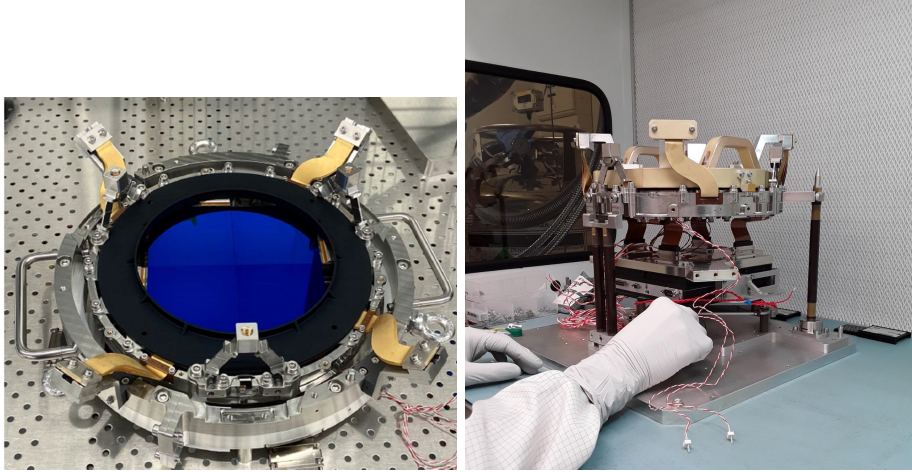


Fig. 28 Left: Engineering model of a complete Focal Plane Assembly populated with full-frame CCDs. Right: Engineering models of the FPA and the Normal Front End Electronics integrated for functional testing at MSSSL.

13.3 PLATO Data Processing System

The PLATO Data Processing System (DPS) is made up of an on-board segment and a ground segment. The on-ground data processing approach is presented in Section 8. Concerning the on-board segment, with 24 normal cameras working at the cadence of 25 seconds and two fast cameras working at the cadence of 2.5 seconds, the amount of raw data produced each day is over 100 Terabit. This volume must be compared to the hundreds of Gigabit which can be actually downloaded each day to the ground. It is clearly not possible to transmit the whole amount of raw data. The role of the on-board processing is to reduce by a factor of more than 1000 the flow rate by downlinking star intensities, centroid curves and imaggettes at the cadence required by the science applications.

The PLATO payload on-board data processing system is made up of an Instrument Control Unit (ICU), two Main Electronic Units (MEU) and a Fast Electronic Unit (FEU). Each MEU contains 6 normal Data Processing Units (N-DPUs) for processing data from the normal cameras. Each N-DPU is dealing with two normal cameras in terms of managing the N-FEE and acquiring data. The nominal processing cadence for the N-DPUs is 25 sec. There are two F-DPUs gathered in the FEU. Each F-DPU is responsible for processing the data of one fast camera. The processing cadence for F-DPUs is 2.5 sec. The F-DPUs main purpose is providing attitude data for the Fine Guidance System (FGS) directly to the Service Module (SVM) AOCS and to the ICU. Furthermore, it manages the F-FEE and handles scientific data of bright stars. There are two ICU channels which work in cold redundancy. The ICU is responsible for the management of the payload, the communication with the SVM and the compression of scientific data before transmitting them as telemetry to the SVM. Data is routed through a SpaceWire network from FEU and MEU to the ICU, and then from the ICU to the SVM. For the FGS data, dedicated SpaceWire links between FEU and

Table 8 PLATO Camera parameters.

Normal cameras	
entrance pupil diameter	120 mm (the frontal lens is 200 mm wide)
focal length	247.5 mm
camera FoV	1037 deg ²
photometric range	4-16 magV
transmission	500-1000 nm
no. CCDs/camera	4
read-out mode	full frame
read-out cadence	25 sec
number of effective pixels	4510×4510
pixel size	18×18 μm
pixel scale	15 arcsec/pixel
nominal working temperature	-80°C
Fast cameras, where different from above	
camera FoV	610 deg ²
photometric range	4 - 8.2 magV
transmission	505-700 nm
	665-1000 nm
read-out mode	frame transfer
read-out cadence	2.5 sec
number of effective pixels	4490×2245

spacecraft AOCS are used. Figure 29 gives an overview of the PLATO data processing system architecture and of the data flow rates while Fig. 30 shows the engineering models during the tests at DLR. It focuses on the sharing of the main functions and the data flows. It is a simplified view of the hardware architecture.

An on-board software is present in the ICU and both normal and fast DPUs. The ICU software is in charge of collecting all science data and housekeeping. It manages the PLATO payload sub-systems (DPS and FEE). In observation mode the N-DPU software must first assemble windows from the images-data-stream, received from the FEE. Then the software performs an initial treatment, which consists of computing the background noise and some correction parameters like smearing and offset. A part of the image data will be sent to the ICU as imaggettes without further processing. On a selection of stars, the N-DPU calculates the centroid and the received flux. Flux and centroid measurements are computed on-board using optimal binary mask as explained in Marchiori et al (2019). The N-DPU is able to stack fluxes and centroids from each camera over periods of 50 seconds and 600 seconds and send it to the ICU. Before averaging the values of fluxes and centroids, an outlier rejection algorithm is used on-board. These data are then compressed by a factor of at least 2.5 for transmission to the SVM mass memory from where they are downloaded to the ground. The star catalogue defined on-ground will be uploaded in the ICU and then forwarded to the DPUs.

The main purpose of the F-DPU is however to perform the attitude calculation of the F-CAMs based on the positions of the stars on the CCD. This Fine Guidance System (FGS) data processing using the knowledge of the camera geometrical model and the differential aberration is providing quaternions of the CAM attitude to the

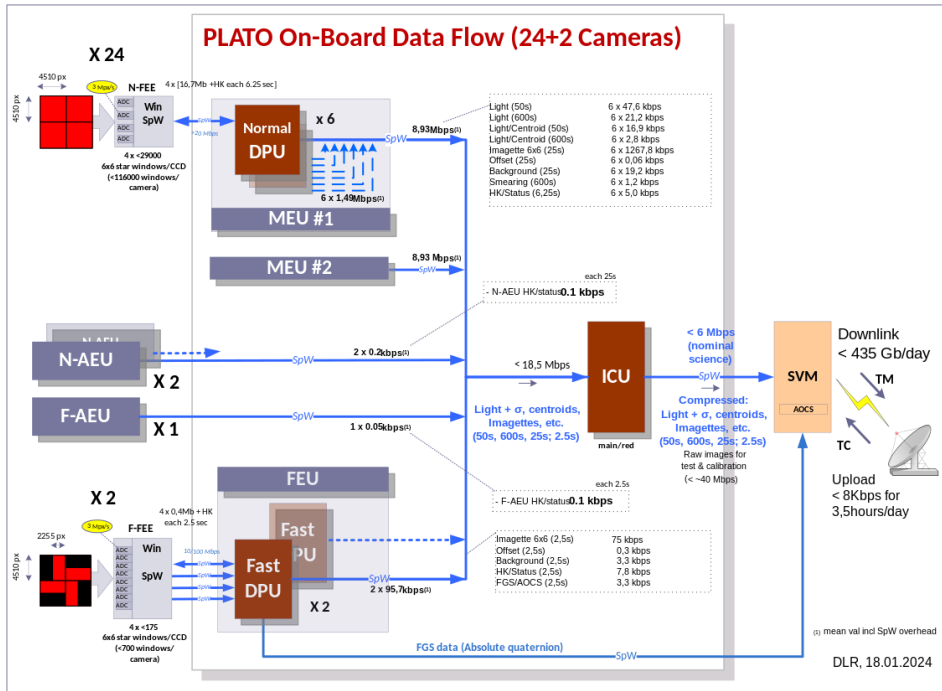


Fig. 29 Simplified overview of the PLATO on-board data flow.

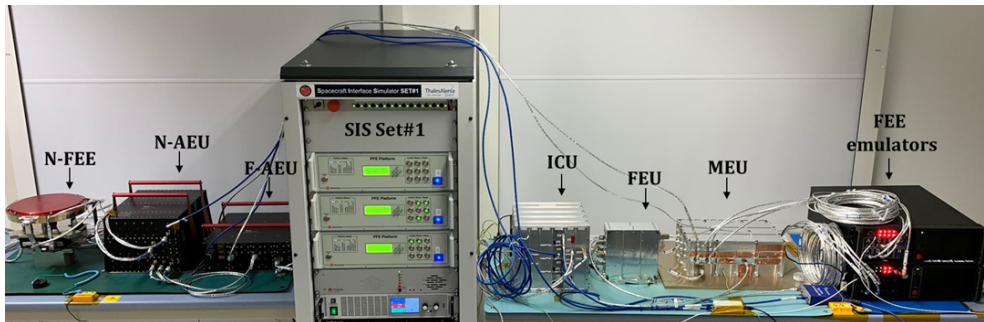


Fig. 30 DPS engineering models test bench at DLR.

AOCS system of the spacecraft. This is a key component needed to reach the pointing performance presented in Table 7.

14 Synergies with other Missions

Exoplanet missions form a significant part of ESA and NASA’s ongoing and future space science programs (Stapelfeldt et al (2021) for an overview). PLATO will start its science operations in 2027. By this time, the extended operations periods for the now ongoing missions CHEOPS and TESS will have ended, although further prolongations could extend their lifetimes until and beyond PLATO launch. Prolongation of James-Webb-Space-Telescope (JWST) operations beyond 2026 will allow it to observe PLATO targets. Two years after PLATO, the ARIEL mission will launch to spectroscopically observe transiting exoplanets. Here we outline the key aspects of synergies with PLATO for these and other missions:

TESS: A discussion of the planet yield of PLATO versus TESS (Ricker et al, 2015) can be found in Section 2. The majority of planets detected by TESS have orbital periods <10 days (Guerrero et al, 2021), while PLATO planets focuses on orbital periods >27 days, including a significant fraction on long-periods >100 days. Most of the planet detections around solar-like stars from PLATO will have $< 4R_{\text{Earth}}$, outnumbering the numbers expected from TESS for this type of stars. There is a clear complementarity of TESS and PLATO.

CHEOPS: The main goal is to search for transits on bright stars already known to host planets to determine precise radii (Benz et al, 2020). A major benefit for PLATO from the CHEOPS mission results from improved understanding and modelling activities in the community on the interpretation of precise planet radii, masses and ages in terms of, e.g, planet formation, evolution and interior atmosphere interactions. While many of the related science questions can only be fully answered when a larger sample of accurately characterised planets from PLATO becomes available, the ongoing activities within CHEOPS pave the way for PLATO data to come. Although likely only possible for very few targets, a cross-calibration of CHEOPS with PLATO will be beneficial. Furthermore, where applicable preparatory observations of PLATO targets by CHEOPS can be beneficial to maximise science return on these objects (e.g. for TTV studies).

ARIEL: will provide spectra of atmospheres of a large number of transiting planets (Tinetti et al, 2018). These planets will mostly be hot and warm Jupiters, with some Neptunes and super-earths around late-type stars. We expect that (ultra-)hot Neptunes and larger target objects on orbits <10 days suitable for ARIEL will already be known via TESS (see Section 2). Based on this, about 20-40 targets are expected in potential PLATO LOPs. Additional targets on smaller, warm planets around bright stars newly detected by PLATO will form additional exciting targets for ARIEL. PLATO will provide high-accuracy radii, prolonged TTV data and well-known ephemeris for these planets within its target fields. Information from accurate N-CAM white-light phase curves and two-colour information from PLATO’s F-CAMs for hot and nearby targets will help to select especially interesting targets for ARIEL (see Section 3.3). Input of PLATO on well-known radii, masses and stellar parameters, including the age, will be beneficial for ARIEL for targets in the PLATO fields. For example, PLATO ages will help breaking the degeneracies for warm Jupiter planets. How planet properties correlate with age (e.g. due to contraction, atmosphere loss, tidal interaction, etc.) can be studied once ages are available in sufficient numbers

and accuracy from PLATO. In addition, the pre-characterisation of stellar activity by PLATO (rotational modulation, phase of activity cycle, frequency of flares and CMEs, granulation) will be helpful. Such data will be especially useful for simultaneously observed targets.

JWST: The main synergy of PLATO and JWST (Gardner et al, 2006) concerns newly detected warm and/or small planets which can be followed up by JWST to investigate their atmospheres, phase curves and albedos. PLATO will form a target finder for JWST on these highly interesting targets in future and provide relevant complementary planet and stellar activity data (see discussion on ARIEL above).

GAIA: Through its astrometric survey of the Milky Way, Gaia (Gaia Collaboration et al, 2016) will discover a large population of massive long period planets, primarily astrometrically. Given that orbital inclinations are known for astrometrically detected planets, PLATO might be able to identify transits on some of them, where even single transit detections (mono-transits) would be very useful and could become the first transit observations of long-period planets. Furthermore, for the vetting of transiting planet candidates, GAIA will help in the identification of background eclipsing binaries as has been demonstrated for TESS candidates by Panahi et al (2022). A significant harvest of new long period (> 5 years), massive exoplanets is expected in the upcoming Gaia data releases (e.g. Gaia DR4). The combination of long-period Gaia planet detections with the smaller and intermediate orbital distance exoplanets discovered by PLATO, will enable the discovery of exoplanets systems with architectures analogous to our own, namely exoplanet systems with shorter period ‘rocky planets’ and longer period gas giants orbiting solar types stars.

Euclid and Roman Space telescope: The Nancy Grace Roman Space telescope (Spergel et al, 2015) is expected to detect exoplanets from microlensing, from transits and from coronagraphic imaging, covering a wide range of planet system parameters. ESA’s Euclid mission also has some capability to detect extrasolar planets, and studies demonstrating the joint detection capabilities of the two missions have been performed (e.g. Bachelet et al 2022; Kerins et al 2023). Correlations of planet population statistics derived from PLATO with Euclid and the Roman Telescope results will provide valuable inputs into further constraining planet formation.

Acknowledgments. This work presents results from the European Space Agency (ESA) space mission PLATO. The PLATO payload, the PLATO Ground Segment and PLATO data processing are joint developments of ESA and the PLATO Mission Consortium (PMC). Funding for the PMC is provided at national levels, in particular by countries participating in the PLATO Multilateral Agreement (Austria, Belgium, Czech Republic, Denmark, France, Germany, Italy, Netherlands, Portugal, Spain, Sweden, Switzerland, Norway, and United Kingdom) and institutions from Brazil. Members of the PLATO Consortium can be found at <https://platomission.com/>. The ESA PLATO mission website is <https://www.cosmos.esa.int/plato>. We thank the teams working for PLATO for all their work.

Specific acknowledgements:

The German PMC, PDC, DPS, and F-FEE team members are supported by the German Aerospace Agency (Deutsches Zentrum für Luft- und Raumfahrt, e.V., DLR) grant numbers 50001401, 50OP2001, 50OP2103, 50OP2104, 50OP2101,

50OP1902 and 50OP2102.

The DLR team members acknowledge the funding by the Research and Development Department of the German Aerospace Center (Deutsches Zentrum für Luft- und Raumfahrt, e.V., DLR).

The research and results presented in this paper has received funding from the Belgian federal Science Policy Office (BELSPO) through various PRODEX grants for PLATO development and from the KU Leuven Research Council (grant C16/18/005: PARADISE).

This project was supported by the KKP-137523 "SeismoLab" Élvonal grant of the Hungarian Research, Development and Innovation Office (NKFIH) and by the Lendület Program of the Hungarian Academy of Sciences under project No. LP2018-7. Project no. C1746651 has been implemented with the support provided by the Ministry of Culture and Innovation of Hungary from the National Research, Development and Innovation Fund, financed under the NVKDP-2021 funding scheme.

This work was supported by the Hungarian National Research, Development and Innovation Office grants OTKA K131508 and KH-130526, and the Élvonal grant KKP-143986. Authors acknowledge the financial support of the Austrian-Hungarian Action Foundation (101öu13, 112öu1).

This work was supported by Fundação para a Ciência e a Tecnologia (FCT) through research grants UIDB/04434/2020 and UIDP/04434/2020.

This work was supported by FCT - Fundação para a Ciência e a Tecnologia through national funds and by FEDER through COMPETE2020 - Programa Operacional Competitividade e Internacionalização by these grants: UIDB/04434/2020; UIDP/04434/2020 and co-funded by the European Union (ERC, FIERCE, 101052347). Views and opinions expressed are however those of the author(s) only and do not necessarily reflect those of the European Union or the European Research Council. Neither the European Union nor the granting authority can be held responsible for them.

This work was (partially) supported by the Spanish MICIN/AEI/10.13039/501100011033 and by "ERDF A way of making Europe" by the "European Union" through grant PID2021-122842OB-C21, and the Institute of Cosmos Sciences University of Barcelona (ICCUB, Unidad de Excelencia 'María de Maeztu') through grant CEX2019-000918-M.

This work is part of the project Advanced technologies for the exploration of the Universe and its components, of the area of Astrophysics and High Energy Physics, within the frame of the R&D&I Complementary Plans of the Spanish Government that are part component 17 of the Recovery and Resilience Mechanism. This contract is funded by the European Union - NextGenerationEU (MICIN/PRTR funds) and by Generalitat de Catalunya.

We acknowledge financial support from the Agencia Estatal de Investigación of the Ministerio de Ciencia e Innovación MCIN/AEI/10.13039/501100011033 and the ERDF "A way of making Europe" through project PID2021-125627OB-C31, from the Centre of Excellence "María de Maeztu" award to the Institut de Ciències de l'Espai (CEX2020-001058-M) and from the Generalitat de Catalunya/CERCA programme. Funding for the Stellar Astrophysics Centre was provided by The Danish National

Research Foundation (Grant DNRF106).

Support from PLATO ASI-INAF agreements n. 2022-28-HH.0.

Giampaolo Piotto, Marco Montalto, Luca Malavolta, Valerio Nascimbeni, Luca Borsato, Giacomo Mantovan, Valentina Granata: Support from PLATO ASI-INAF agreements n. 2022-28-HH.0.

This work on the PLATO space mission was supported by CNES.

This study is supported by the Research Council of Norway through its Centres of Excellence funding scheme, project number 223272 (CEED) and 332523 (PHAB).

Brazilian participation on the PLATO mission is funded by Fundação de Amparo à Pesquisa do Estado de São Paulo (FAPESP) under grant 2016/13750-6.

The team at IAC acknowledges support from the Spanish Research Agency of the Ministry of Science and Innovation (AEI-MICINN) under grant 'Contribution of the IAC to the PLATO Space Mission' with reference PID2019-107061GB-C66, DOI: 10.13039/501100011033.

U.C.Kolb and C.A. Haswell were supported by grant ST/T000295/1 from STFC.

C.A. Haswell was supported by grant ST/X001164/1 from STFC.

NW, SA, PB, GB, FDA, DWE, DF, DLH, SH, JI, NM, MR, GR, LS, MW have been fully or partly supported by grant funding from the UK Space Agency through grants ST/R004838/1 and ST/X001571/1.

The PDPC-C hardware is largely provided through the UK STFC IRIS digital research infrastructure (<https://www.iris.ac.uk>) project.

D.M.B. gratefully acknowledges a senior postdoctoral fellowship from the Research Foundation Flanders (FWO; grant number [1286521N]), the Engineering and Physical Sciences Research Council (EPSRC) of UK Research and Innovation (UKRI) in the form of a Frontier Research grant under the UK government's ERC Horizon Europe funding guarantee (SYMPHONY; grant number [EP/Y031059/1]), and a Royal Society University Research Fellowship (grant number: URF\R1\231631)

PK and MK would like to acknowledge the funding of the CZ contribution to PLATO mission from ESA PRODEX under PEA-4000127913 contract.

MS and RK would like to acknowledge the funding from the LTT-20015 grant of the MEYS.

UH, OK, TO acknowledge support from the Swedish National Space Agency (SNSA/Rymdstyrelsen).

I.L. and A.B. extend their gratitude to the Fundação para a Ciência e Tecnologia (FCT, Portugal) for the financial support provided to the Center for Astrophysics and Gravitation (CENTRA/IST/ULisboa) under Grant Project No. UIDB/00099/2020.

The work of the Porto team was supported by FCT - Fundação para a Ciência e a Tecnologia through national funds by grants: UIDB/04434/2020; UIDP/04434/2020.

The Portuguese team thanks the Portuguese Space Agency for the provision of financial support in the framework of the PRODEX Programme of the European Space Agency (ESA) under contracts number 4000133026, 4000140773, and 4000124770.

CAB and INTA authors are funded by Spanish MCIN/AEI/10.13039/501100011033 grants PID2019-107061GB -C61 and -C62.

JPG, MLM, JRR, ARB and RGH acknowledge financial support from project PID2019-107061GB-C63 from the 'Programas Estatales de Generación de

Conocimiento y Fortalecimiento Científico y Tecnológico del Sistema de I+D+i y de I+D+i Orientada a los Retos de la Sociedad.

E.A.'s work has been carried out within the framework of the NCCR PlanetS supported by the Swiss National Science Foundation under grants 51NF40_182901 and 51NF40_205606.

RA acknowledges funding from the Science & Technology Facilities Council (STFC) through Consolidated Grant ST/W000857/1.

Paul Beck acknowledges support by the Spanish Ministry of Science and Innovation with the *Ramón y Cajal* fellowship number RYC-2021-033137-I and the number MRR4032204.

S.M. acknowledges support from the Spanish Ministry of Science and Innovation (MICINN) with the Ramón y Cajal fellowship no. RYC-2015-17697, the grant no. PID2019-107187GB-I00, and through AEI under the Severo Ochoa Centres of Excellence Programme 2020–2023 (CEX2019-000920-S).

JMMH is funded by Spanish MCIN/AEI/10.13039/501100011033 grant PID2019-107061GB-C61.

M.L.M. acknowledge financial support from the Severo Ochoa grant CEX2021-001131-S funded by MCIN/AEI/10.13039/50110001103.

J.P.G. acknowledge financial support from the Severo Ochoa grant CEX2021-001131-S funded by MCIN/AEI/10.13039/50110001103.

C.P.M. acknowledge financial support from the Severo Ochoa grant CEX2021-001131-S funded by MCIN/AEI/10.13039/50110001103.

F.J.P. acknowledge financial support from the Severo Ochoa grant CEX2021-001131-S funded by MCIN/AEI/10.13039/50110001103.

J.R.G. acknowledge financial support from the Severo Ochoa grant CEX2021-001131-S funded by MCIN/AEI/10.13039/50110001103.

M.A.S.C. acknowledge financial support from the Severo Ochoa grant CEX2021-001131-S funded by MCIN/AEI/10.13039/50110001103.

R.S.M. acknowledge financial support from the Severo Ochoa grant CEX2021-001131-S funded by MCIN/AEI/10.13039/50110001103.

M.V.A. acknowledge financial support from the Severo Ochoa grant CEX2021-001131-S funded by MCIN/AEI/10.13039/50110001103.

B.A.M. acknowledge financial support from the Severo Ochoa grant CEX2021-001131-S funded by MCIN/AEI/10.13039/50110001103.

A.C. acknowledge financial support from the Severo Ochoa grant CEX2021-001131-S funded by MCIN/AEI/10.13039/50110001103.

J.M.G.L. acknowledge financial support from the Severo Ochoa grant CEX2021-001131-S funded by MCIN/AEI/10.13039/50110001103.

Juan Carlos Morales acknowledge financial support from the Agencia Estatal de Investigación of the Ministerio de Ciencia e Innovación MCIN/AEI/10.13039/501100011033 and the ERDF “A way of making Europe” through project PID2021-125627OB-C31, from the Centre of Excellence “María de Maeztu” award to the Institut de Ciències de l’Espai (CEX2020-001058-M) and from the Generalitat de Catalunya/CERCA programme.

Ignasi Ribas acknowledge financial support from the Agencia Estatal de Investigación

of the Ministerio de Ciencia e Innovación MCIN/AEI/10.13039/501100011033 and the ERDF “A way of making Europe” through project PID2021-125627OB-C31, from the Centre of Excellence “María de Maeztu” award to the Institut de Ciències de l’Espai (CEX2020-001058-M) and from the Generalitat de Catalunya/CERCA programme.

Aldo Serenelli acknowledge financial support from the Agencia Estatal de Investigación of the Ministerio de Ciencia e Innovación MCIN/AEI/10.13039/501100011033 and the ERDF “A way of making Europe” through project PID2021-125627OB-C31, from the Centre of Excellence “María de Maeztu” award to the Institut de Ciències de l’Espai (CEX2020-001058-M) and from the Generalitat de Catalunya/CERCA programme.

DJA is supported by UKRI through the STFC (ST/R00384X/1) and EPSRC (EP/X027562/1).

SLC acknowledges funding from the Science & Technology Facilities Council (STFC) through an Ernest Rutherford Research Fellowship ST/R003726/1.

PPA acknowledges the support of Fundação para a Ciência e Tecnologia FCT/MCTES, Portugal, through national funds by the following grants UIDB/04434/2020, UIDP/04434/2020.FCT, 2022.03993.PTDC.

Tiago Campante is supported by FCT in the form of a work contract (CEECIND/00476/2018).

MC acknowledges the support of Fundação para a Ciência e Tecnologia FCT/MCTES, Portugal, through national funds by these grants UIDB/04434/2020, UIDP/04434/2020.FCT, 2022.06962.PTDC.FCT, 2022.03993.PTDC and CEECIND/02619/2017. ZsB acknowledges the support by the János Bolyai Research Scholarship of the Hungarian Academy of Sciences.

Gy. M. Szabó acknowledges support from the PRODEX Experiment Agreement No. 4000137122.

Róbert Szabó: Lendület Program of the Hungarian Academy of Sciences, project No. LP2018-7/2022.

Róbert Szabó: KKP-137523 "SeismoLab" Élvonal grant of the Hungarian Research, Development and Innovation Office (NKFIH).

Róbert Szabó: MW-Gaia COST Action (CA18104).

KV was supported by the Bolyai János Research Scholarship of the Hungarian Academy of Sciences, and by the Bolyai+ grant ÚNKP-22-5-ELTE-1093.

D.M.B. gratefully acknowledges funding from the Research Foundation Flanders (FWO) by means of a senior postdoctoral fellowship (grant agreement No. 1286521N).

Thibault Merle is granted by the BELSPO Belgian federal research program FED-tWIN under the research profile Prf-2020-033_BISTRO.

Thierry Morel acknowledges financial support from Belspo for contract PRODEX PLATO mission development.

S.N.B acknowledges support from PLATO ASI-INAF agreement n. 2015-019-R.1-2018.

DLB acknowledges support from NASA through the Astrophysics Science Smallsat Studies program (80NSSC20K1246) and the TESS GI Program (80NSSC21K0334).

DBdeF acknowledges financial support from the Brazilian agency CNPq-PQ2 (Grant No. 305566/2021-0). Research activities of STELLAR TEAM of Federal University

of Ceara are supported by continuous grants from the Brazilian agency CNPq. J. K. gratefully acknowledges the support of the Swedish National Space Agency (SNSA; DNR 2020-00104) and of the Swedish Research Council (VR: Etableringsbidrag 2017-04945).

AJM acknowledges support from the Swedish Research Council (grant 2017-04945) and the Swedish National Space Agency (grant 120/19C).

Support for MC is provided by ANID grants ICN12_009 (Millennium Institute of Astrophysics, FB10003 (Basal-CATA2), and 1231637 (FONDECYT).

CD acknowledges SNSF under grant TMSGI2_211313.

MK acknowledges the support from ESA-PRODEX PEA4000127913.

TL was supported by a grant from the Branco Weiss Foundation.

PM acknowledges support from STFC research grant number ST/M001040/1.

F.J.P. acknowledges financial support from the grant CEX2021-001131-S funded by MCIN/AEI/ 10.13039/501100011033.

BR-A acknowledges funding support from FONDECYT Iniciacion grant 11181295 and ANID Basal project FB210003.

A.R.G.S. acknowledges the support by FCT through national funds and by FEDER through COMPETE2020 by these grants: UIDB/04434/2020 & UIDP/04434/2020. A.R.G.S. is supported by FCT through the work contract No. 2020.02480.CEECIND/CP1631/CT0001.

15 Appendix A

We outline briefly the simple analytic model of the estimation of planet radius accuracy. All calculations below are valid for beginning of life (BOL). We start from the following form of the conversion of V magnitudes to fluxes measurable by PLATO

$$f = 180000e^{-/s} \cdot 10^{-0.4(V-11)} \quad (1)$$

The noise level at flux f can be estimated (Cabrera et al., in prep.) as:

$$N = \sqrt{(9 \cdot 10^{-6})^2 + \frac{1/f + (150/f)^2}{N_{\text{camera}} \cdot T/t_{\text{exp}}}} \quad (2)$$

Here N is the noise level for $T = 1$ hour time-scale and $N_{\text{camera}} = 24$ was assumed. $t_{\text{exp}} = 25\text{s}$ is the exposure cadence. The first constant term is the jitter-noise, the last term is the readout noise. It is assumed that the magnitude zero-point is the same for all cameras and the readout-noise is also independent on which camera we consider.

The radius ratio precision can be derived from the equation

$$\delta = \left(\frac{R_{\text{planet}}}{R_{\text{star}}} \right)^2 L_D \quad (3)$$

where L_D describes the effect of limb darkening. The current knowledge of limb darkening for low magnetic field, quiet, solar-type stars is known sufficiently well that the contribution to the uncertainty in the radius ratio is negligible (c.f. Section 4.4. of [Maxted 2023](#) as well as [Ludwig et al 2023](#)). However, numerical simulations show that about over 800 Gauss surface magnetic field the theory predicts higher limb darkening than that was observed. In the same way, some simulations result in limb brightening effects difficult to understand at this point (see [Ludwig et al 2023](#)). So, the very active stars can have different properties and more work is needed to calibrate properly their limb darkening behaviour (c.f. [Csizmadia et al 2013](#); [Espinoza and Jordán 2015](#); [Agol et al 2020](#); [Patel and Espinoza 2022](#)). The results are not changing if we consider different limb darkening laws; therefore, for sake of simplicity, we used linear limb darkening with a constant linear limb darkening coefficient $u = 0.6$ which is a solar-like value ($L_D = 1/(1 - u/3)$). Then we have by differentiation that

$$\frac{\Delta k}{k} = \frac{\sqrt{2}}{2} \frac{N(V)}{\delta} \frac{1}{\sqrt{N_{\text{transit}} D}} \quad (4)$$

abbreviating the planet-to-star radius ratio $k = R_{\text{planet}}/R_{\text{star}}$. The factor $\sqrt{2}$ is valid if the baseline is determined by observing only one full transit duration length before and after the transit. However, the factor will decrease to 1 if the baseline length is much longer than the transit duration (in the limit to infinity). Since the noise level is calculated for 1 hour in [Cabrera et al. \(in prep\)](#), the transit duration D plays a role here. Despite the simplicity of this analytic model, the results are in quite good agreement with [Barros et al \(2020\)](#); [Morris et al \(2020\)](#); and [Csizmadia et al \(2023\)](#).

References

- Acuña L, Deleuil M, Mousis O, et al (2021) Characterisation of the hydrospheres of TRAPPIST-1 planets. *A&A*647:A53. <https://doi.org/10.1051/0004-6361/202039885>, [arXiv:2101.08172](https://arxiv.org/abs/2101.08172) [astro-ph.EP]
- Acuña L, Deleuil M, Mousis O (2023) Interior-atmosphere modelling to assess the observability of rocky planets with JWST. *A&A*677:A14. <https://doi.org/10.1051/0004-6361/202245736>, [arXiv:2305.01250](https://arxiv.org/abs/2305.01250) [astro-ph.EP]
- Adams ER, Seager S, Elkins-Tanton L (2008) Ocean Planet or Thick Atmosphere: On the Mass-Radius Relationship for Solid Exoplanets with Massive Atmospheres. *ApJ*673(2):1160–1164. <https://doi.org/10.1086/524925>, [arXiv:0710.4941](https://arxiv.org/abs/0710.4941) [astro-ph]
- Adibekyan V, Dorn C, Sousa SG, et al (2021) A compositional link between rocky exoplanets and their host stars. *Science* 374(6565):330–332. <https://doi.org/10.1126/science.abg8794>, [arXiv:2102.12444](https://arxiv.org/abs/2102.12444) [astro-ph.EP]
- Aerts C (2021) Probing the interior physics of stars through asteroseismology. *Reviews of Modern Physics* 93(1):015001. <https://doi.org/10.1103/RevModPhys.93.015001>, [arXiv:1912.12300](https://arxiv.org/abs/1912.12300) [astro-ph.SR]

- Agol E, Luger R, Foreman-Mackey D (2020) Analytic Planetary Transit Light Curves and Derivatives for Stars with Polynomial Limb Darkening. *AJ*159(3):123. <https://doi.org/10.3847/1538-3881/ab4fee>, [arXiv:1908.03222](https://arxiv.org/abs/1908.03222) [astro-ph.EP]
- Aguirre Børsen-Koch V, Rørsted JL, Justesen AB, et al (2022) The BAYesian STellar algorithm (BASTA): a fitting tool for stellar studies, asteroseismology, exoplanets, and Galactic archaeology. *MNRAS*509(3):4344–4364. <https://doi.org/10.1093/mnras/stab2911>, [arXiv:2109.14622](https://arxiv.org/abs/2109.14622) [astro-ph.SR]
- Ahuir J, Strugarek A, Brun AS, et al (2021) Magnetic and tidal migration of close-in planets. Influence of secular evolution on their population. *A&A*650:A126. <https://doi.org/10.1051/0004-6361/202040173>, [arXiv:2104.01004](https://arxiv.org/abs/2104.01004) [astro-ph.EP]
- Aigrain S, Llama J, Ceillier T, et al (2015) Testing the recovery of stellar rotation signals from Kepler light curves using a blind hare-and-hounds exercise. *MNRAS*450(3):3211–3226. <https://doi.org/10.1093/mnras/stv853>, [arXiv:1504.04029](https://arxiv.org/abs/1504.04029) [astro-ph.SR]
- Akinsanmi B, Barros SCC, Santos NC, et al (2019) Detectability of shape deformation in short-period exoplanets. *A&A*621:A117. <https://doi.org/10.1051/0004-6361/201834215>, [arXiv:1812.04538](https://arxiv.org/abs/1812.04538) [astro-ph.EP]
- Amazo-Gómez EM, Shapiro AI, Solanki SK, et al (2020) Inflection point in the power spectrum of stellar brightness variations. III. Facular versus spot dominance on stars with known rotation periods. *A&A*642:A225. <https://doi.org/10.1051/0004-6361/202038926>, [arXiv:2008.11492](https://arxiv.org/abs/2008.11492) [astro-ph.SR]
- Angus R, Aigrain S, Foreman-Mackey D, et al (2015) Calibrating gyrochronology using Kepler asteroseismic targets. *MNRAS*450(2):1787–1798. <https://doi.org/10.1093/mnras/stv423>, [arXiv:1502.06965](https://arxiv.org/abs/1502.06965) [astro-ph.EP]
- Appourchaux T (2003) Peak Bagging for Solar-like Stars. *Ap&SS*284(1):109–119
- Appourchaux T, Chaplin WJ, García RA, et al (2012) Oscillation mode frequencies of 61 main-sequence and subgiant stars observed by Kepler. *A&A*543:A54. <https://doi.org/10.1051/0004-6361/201218948>, [arXiv:1204.3147](https://arxiv.org/abs/1204.3147) [astro-ph.SR]
- Appourchaux T, Antia HM, Benomar O, et al (2016) Oscillation mode linewidths and heights of 23 main-sequence stars observed by Kepler (Corrigendum). *A&A*595:C2. <https://doi.org/10.1051/0004-6361/201323317e>
- Audenaert J, Kuszlewicz JS, Tkachenko A, et al (2021) TESS Data for Asteroseismology (T'DA) Stellar Variability Classification Pipeline. In: *ApJS*, submitted
- Audenaert J, Tkachenko A, Aerts C (2022) An all-sky stellar variability machine learning classification framework for TESS and PLATO. In: *SciOps 2022: Artificial Intelligence for Science and Operations in Astronomy (SCIOPS)*. Proceedings of

- the ESA/ESO SCOPS Workshop held 16-20 May, p 31, <https://doi.org/10.5281/zenodo.6577169>
- Auvergne M, Bodin P, Boissard L, et al (2009) The CoRoT satellite in flight: description and performance. *A&A*506:411–424. <https://doi.org/10.1051/0004-6361/200810860>, [arXiv:0901.2206](https://arxiv.org/abs/0901.2206) [astro-ph.SR]
- Bachelet E, Specht D, Penny M, et al (2022) Euclid-Roman joint microlensing survey: Early mass measurement, free floating planets, and exomoons. *A&A*664:A136. <https://doi.org/10.1051/0004-6361/202140351>, [arXiv:2202.09475](https://arxiv.org/abs/2202.09475) [astro-ph.EP]
- Baglin A (2016) The corot legacy book: The adventure of the ultra high precision photometry from space, by the corot team
- Baglin A, Auvergne M, Boissard L, et al (2006) CoRoT: a high precision photometer for stellar evolution and exoplanet finding. In: 36th COSPAR Scientific Assembly, p 3749
- Bakos G, Noyes RW, Kovács G, et al (2004) Wide-Field Millimagnitude Photometry with the HAT: A Tool for Extrasolar Planet Detection. *PASP*116:266–277. <https://doi.org/10.1086/382735>, [arXiv:astro-ph/0401219](https://arxiv.org/abs/astro-ph/0401219)
- Ball WH, Chaplin WJ, Nielsen MB, et al (2020) Robust asteroseismic properties of the bright planet host HD 38529. *MNRAS*499(4):6084–6093. <https://doi.org/10.1093/mnras/staa3190>, [arXiv:2010.07323](https://arxiv.org/abs/2010.07323) [astro-ph.SR]
- Balona LA, Ozuyar D (2020) TESS observations of Be stars: a new interpretation. *MNRAS*493(2):2528–2544. <https://doi.org/10.1093/mnras/staa389>, [arXiv:1911.03068](https://arxiv.org/abs/1911.03068) [astro-ph.SR]
- Barnes SA (2003) On the Rotational Evolution of Solar- and Late-Type Stars, Its Magnetic Origins, and the Possibility of Stellar Gyrochronology. *ApJ*586(1):464–479. <https://doi.org/10.1086/367639>, [arXiv:astro-ph/0303631](https://arxiv.org/abs/astro-ph/0303631) [astro-ph]
- Barnes SA (2007) Ages for Illustrative Field Stars Using Gyrochronology: Viability, Limitations, and Errors. *ApJ*669:1167–1189. <https://doi.org/10.1086/519295>, [arXiv:0704.3068](https://arxiv.org/abs/0704.3068)
- Barros SCC, Demangeon O, Díaz RF, et al (2020) Improving transit characterisation with Gaussian process modelling of stellar variability. *A&A*634:A75. <https://doi.org/10.1051/0004-6361/201936086>, [arXiv:2001.07975](https://arxiv.org/abs/2001.07975) [astro-ph.EP]
- Batalha NM (2014) Exploring exoplanet populations with NASA’s Kepler Mission. *Proceedings of the National Academy of Science* 111(35):12647–12654. <https://doi.org/10.1073/pnas.1304196111>, [arXiv:1409.1904](https://arxiv.org/abs/1409.1904) [astro-ph.EP]

- Batygin K, Petit AC (2023) Dissipative Capture of Planets into First-order Mean-motion Resonances. *ApJ*946(1):L11. <https://doi.org/10.3847/2041-8213/acc015>, [arXiv:2303.02766](https://arxiv.org/abs/2303.02766) [astro-ph.EP]
- Baumeister P, Tosi N (2023) ExoMDN: Rapid characterization of exoplanet interior structures with mixture density networks. *A&A*676:A106. <https://doi.org/10.1051/0004-6361/202346216>, [arXiv:2306.09002](https://arxiv.org/abs/2306.09002) [astro-ph.EP]
- Bazot M (2020) Uncertainties and biases in modelling 16 Cygni A and B. *A&A*635:A26. <https://doi.org/10.1051/0004-6361/201935565>, [arXiv:2002.11070](https://arxiv.org/abs/2002.11070) [astro-ph.SR]
- Beck PG, Montalbán J, Kallinger T, et al (2012) Fast core rotation in red-giant stars as revealed by gravity-dominated mixed modes. *Nature*481(7379):55–57. <https://doi.org/10.1038/nature10612>, [arXiv:1112.2825](https://arxiv.org/abs/1112.2825) [astro-ph.SR]
- Bellinger EP (2020) A seismic scaling relation for stellar age II: the red giant branch. *MNRAS*492(1):L50–L55. <https://doi.org/10.1093/mnras/slz178>, [arXiv:1911.11804](https://arxiv.org/abs/1911.11804) [astro-ph.SR]
- Bellinger EP, Angelou GC, Hekker S, et al (2016) Fundamental Parameters of Main-Sequence Stars in an Instant with Machine Learning. *ApJ*830(1):31. <https://doi.org/10.3847/0004-637X/830/1/31>, [arXiv:1607.02137](https://arxiv.org/abs/1607.02137) [astro-ph.SR]
- Bellinger EP, Basu S, Hekker S, et al (2017) Model-independent Measurement of Internal Stellar Structure in 16 Cygni A and B. *ApJ*851(2):80. <https://doi.org/10.3847/1538-4357/aa9848>, [arXiv:1710.11487](https://arxiv.org/abs/1710.11487) [astro-ph.SR]
- Bellinger EP, Basu S, Hekker S, et al (2019) Testing Stellar Evolution with Asteroseismic Inversions of a Main-sequence Star Harboring a Small Convective Core. *ApJ*885(2):143. <https://doi.org/10.3847/1538-4357/ab4a0d>, [arXiv:1910.00603](https://arxiv.org/abs/1910.00603) [astro-ph.SR]
- Bellinger EP, Basu S, Hekker S, et al (2021) Asteroseismic Inference of the Central Structure in a Subgiant Star. *ApJ*915(2):100. <https://doi.org/10.3847/1538-4357/ac0051>, [arXiv:2105.04564](https://arxiv.org/abs/2105.04564) [astro-ph.SR]
- Benz W, Ida S, Alibert Y, et al (2014) Planet Population Synthesis. In: Beuther H, Klessen RS, Dullemond CP, et al (eds) *Protostars and Planets VI*, pp 691–713, https://doi.org/10.2458/azu_uapress_9780816531240-ch030, 1402.7086
- Benz W, Broeg C, Fortier A, et al (2020) The CHEOPS mission. *Experimental Astronomy* <https://doi.org/10.1007/s10686-020-09679-4>, [arXiv:2009.11633](https://arxiv.org/abs/2009.11633) [astro-ph.IM]
- Berger TA, Huber D, Gaidos E, et al (2020) The Gaia-Kepler Stellar Properties Catalog. II. Planet Radius Demographics as a Function of Stellar Mass and Age. *AJ*160(3):108. <https://doi.org/10.3847/1538-3881/aba18a>, [arXiv:2005.14671](https://arxiv.org/abs/2005.14671) [astro-ph.EP]

- Bergomi M, Magrin D, Farinato J, et al (2012) To PLANetary Transit or not? An extremely large field of view camera with a CaF₂ component tested in thermovacuum. In: Clampin MC, Fazio GG, MacEwen HA, et al (eds) Space Telescopes and Instrumentation 2012: Optical, Infrared, and Millimeter Wave
- Bergsten GJ, Pascucci I, Mulders GD, et al (2022) The Demographics of Kepler's Earths and Super-Earths into the Habitable Zone. *AJ*164(5):190. <https://doi.org/10.3847/1538-3881/ac8fea>, [arXiv:2209.04047](https://arxiv.org/abs/2209.04047) [astro-ph.EP]
- Bétrisey J, Pezzotti C, Buldgen G, et al (2022) Kepler-93: A testbed for detailed seismic modelling and orbital evolution of super-Earths around solar-like stars. *A&A*659:A56. <https://doi.org/10.1051/0004-6361/202141083>, [arXiv:2111.13686](https://arxiv.org/abs/2111.13686) [astro-ph.EP]
- Bitsch B, Izidoro A, Johansen A, et al (2019) Formation of planetary systems by pebble accretion and migration: growth of gas giants. *A&A*623:A88. <https://doi.org/10.1051/0004-6361/201834489>, [arXiv:1902.08771](https://arxiv.org/abs/1902.08771) [astro-ph.EP]
- Bonati I, Lasbleis M, Noack L (2021) Structure and Thermal Evolution of Exoplanetary Cores. *Journal of Geophysical Research (Planets)* 126(5):e06724. <https://doi.org/10.1029/2020JE006724>
- Bonfils X, Delfosse X, Udry S, et al (2013) The HARPS search for southern extra-solar planets. XXXI. The M-dwarf sample. *A&A*549:A109. <https://doi.org/10.1051/0004-6361/201014704>
- Borucki WJ, Koch D, Basri G, et al (2010) Kepler Planet-Detection Mission: Introduction and First Results. *Science* 327:977. <https://doi.org/10.1126/science.1185402>
- Borucki WJ, Koch DG, Basri G, et al (2011) Characteristics of Planetary Candidates Observed by Kepler. II. Analysis of the First Four Months of Data. *ApJ*736(1):19. <https://doi.org/10.1088/0004-637X/736/1/19>, [arXiv:1102.0541](https://arxiv.org/abs/1102.0541) [astro-ph.EP]
- Boukrouche R, Lichtenberg T, Pierrehumbert RT (2021) Beyond Runaway: Initiation of the Post-runaway Greenhouse State on Rocky Exoplanets. *ApJ*919(2):130. <https://doi.org/10.3847/1538-4357/ac1345>, [arXiv:2107.14150](https://arxiv.org/abs/2107.14150) [astro-ph.EP]
- Bray JC, Kolb U, Rowden P, et al (2023) Population study of astrophysical false positive detections in the southern PLATO field. *MNRAS*518(3):3637–3652. <https://doi.org/10.1093/mnras/stac3262>, [arXiv:2211.04574](https://arxiv.org/abs/2211.04574) [astro-ph.EP]
- Breton SN, Santos ARG, Bugnet L, et al (2021) ROOSTER: a machine-learning analysis tool for Kepler stellar rotation periods. *A&A*647:A125. <https://doi.org/10.1051/0004-6361/202039947>, [arXiv:2101.10152](https://arxiv.org/abs/2101.10152) [astro-ph.SR]
- Brugger B, Mousis O, Deleuil M, et al (2017) Constraints on Super-Earth Interiors from Stellar Abundances. *ApJ*850(1):93. <https://doi.org/10.3847/1538-4357/>

- aa965a, arXiv:1710.09776 [astro-ph.EP]
- Bryson S, Kunimoto M, Kopparapu RK, et al (2021) The Occurrence of Rocky Habitable-zone Planets around Solar-like Stars from Kepler Data. *AJ*161(1):36. <https://doi.org/10.3847/1538-3881/abc418>, arXiv:2010.14812 [astro-ph.EP]
- Bugnet L, García RA, Davies GR, et al (2018) FliPer: A global measure of power density to estimate surface gravities of main-sequence solar-like stars and red giants. *A&A*620:A38. <https://doi.org/10.1051/0004-6361/201833106>, arXiv:1809.05105 [astro-ph.SR]
- Buldgen G, Salmon SJAJ, Reese DR, et al (2016) In-depth study of 16CygB using inversion techniques. *A&A*596:A73. <https://doi.org/10.1051/0004-6361/201628773>, arXiv:1608.05546 [astro-ph.SR]
- Buldgen G, Salmon SJAJ, Noels A, et al (2017) Seismic inversion of the solar entropy. A case for improving the standard solar model. *A&A*607:A58. <https://doi.org/10.1051/0004-6361/201731354>, arXiv:1707.05138 [astro-ph.SR]
- Buldgen G, Reese DR, Dupret MA (2018) Constraining convective regions with asteroseismic linear structural inversions. *A&A*609:A95. <https://doi.org/10.1051/0004-6361/201730693>, arXiv:1711.05031 [astro-ph.SR]
- Buldgen G, Rendle B, Sonoi T, et al (2019) Mean density inversions for red giants and red clump stars. *MNRAS*482(2):2305–2319. <https://doi.org/10.1093/mnras/sty2346>, arXiv:1808.08391 [astro-ph.SR]
- Buzasi DL, Bruntt H, Bedding TR, et al (2005) Altair: The Brightest δ Scuti Star. *ApJ*619(2):1072–1076. <https://doi.org/10.1086/426704>, arXiv:astro-ph/0405127 [astro-ph]
- Campante TL, Lund MN, Kuszlewicz JS, et al (2016) Spin-Orbit Alignment of Exoplanet Systems: Ensemble Analysis Using Asteroseismology. *ApJ*819(1):85. <https://doi.org/10.3847/0004-637X/819/1/85>, arXiv:1601.06052 [astro-ph.EP]
- Campante TL, Corsaro E, Lund MN, et al (2019) TESS Asteroseismology of the Known Red-giant Host Stars HD 212771 and HD 203949. *ApJ*885(1):31. <https://doi.org/10.3847/1538-4357/ab44a8>, arXiv:1909.05961 [astro-ph.SR]
- Cannizzo JK, Smale AP, Wood MA, et al (2012) The Kepler Light Curves of V1504 Cygni and V344 Lyrae: A Study of the Outburst Properties. *ApJ*747(2):117. <https://doi.org/10.1088/0004-637X/747/2/117>, arXiv:1112.4506 [astro-ph.SR]
- Carrión-González Ó, García Muñoz A, Cabrera J, et al (2020) Directly imaged exoplanets in reflected starlight: the importance of knowing the planet radius. *A&A*640:A136. <https://doi.org/10.1051/0004-6361/202038101>, arXiv:2006.08784 [astro-ph.EP]

- Carrión-González Ó, García Muñoz A, Santos NC, et al (2021) Constraining the radius and atmospheric properties of directly imaged exoplanets through multi-phase observations. *A&A*655:A92. <https://doi.org/10.1051/0004-6361/202141469>, [arXiv:2108.10918](https://arxiv.org/abs/2108.10918) [astro-ph.EP]
- Catanzarite J, Shao M (2011) The Occurrence Rate of Earth Analog Planets Orbiting Sun-like Stars. *ApJ*738:151. <https://doi.org/10.1088/0004-637X/738/2/151>, [arXiv:1103.1443](https://arxiv.org/abs/1103.1443) [astro-ph.EP]
- Ceillier T, van Saders J, García RA, et al (2016) Rotation periods and seismic ages of KOIs - comparison with stars without detected planets from Kepler observations. *MNRAS*456(1):119–125. <https://doi.org/10.1093/mnras/stv2622>, [arXiv:1510.09023](https://arxiv.org/abs/1510.09023) [astro-ph.SR]
- Ceillier T, Tayar J, Mathur S, et al (2017) Surface rotation of Kepler red giant stars. *A&A*605:A111. <https://doi.org/10.1051/0004-6361/201629884>, [arXiv:1707.05989](https://arxiv.org/abs/1707.05989) [astro-ph.SR]
- Chaplin WJ, Kjeldsen H, Bedding TR, et al (2011a) Predicting the Detectability of Oscillations in Solar-type Stars Observed by Kepler. *ApJ*732(1):54. <https://doi.org/10.1088/0004-637X/732/1/54>, [arXiv:1103.0702](https://arxiv.org/abs/1103.0702) [astro-ph.SR]
- Chaplin WJ, Kjeldsen H, Christensen-Dalsgaard J, et al (2011b) Ensemble Asteroseismology of Solar-Type Stars with the NASA Kepler Mission. *Science* 332:213. <https://doi.org/10.1126/science.1201827>, [arXiv:1109.4723](https://arxiv.org/abs/1109.4723) [astro-ph.SR]
- Chaplin WJ, Sanchis-Ojeda R, Campante TL, et al (2013) Asteroseismic Determination of Obliquities of the Exoplanet Systems Kepler-50 and Kepler-65. *ApJ*766:101. <https://doi.org/10.1088/0004-637X/766/2/101>, [arXiv:1302.3728](https://arxiv.org/abs/1302.3728) [astro-ph.EP]
- Chaplin WJ, Basu S, Huber D, et al (2014) Asteroseismic Fundamental Properties of Solar-type Stars Observed by the NASA Kepler Mission. *ApJS*210(1):1. <https://doi.org/10.1088/0067-0049/210/1/1>, [arXiv:1310.4001](https://arxiv.org/abs/1310.4001) [astro-ph.SR]
- Chaplin WJ, Serenelli AM, Miglio A, et al (2020) Age dating of an early Milky Way merger via asteroseismology of the naked-eye star ν Indi. *Nature Astronomy* 4:382–389. <https://doi.org/10.1038/s41550-019-0975-9>, [arXiv:2001.04653](https://arxiv.org/abs/2001.04653) [astro-ph.GA]
- Chontos A, Huber D, Berger TA, et al (2021) TESS Asteroseismology of α Mensae: Benchmark Ages for a G7 Dwarf and Its M Dwarf Companion. *ApJ*922(2):229. <https://doi.org/10.3847/1538-4357/ac1269>, [arXiv:2012.10797](https://arxiv.org/abs/2012.10797) [astro-ph.SR]
- Christensen-Dalsgaard J (2018) Asteroseismology with solar-like oscillations. In: Rozelot JP, Babayev ES (eds) *Variability of the Sun and Sun-Like Stars: from Asteroseismology to Space Weather*. p 125

- Christensen-Dalsgaard J (2021) Solar structure and evolution. Living Reviews in Solar Physics 18(1):2. <https://doi.org/10.1007/s41116-020-00028-3>, arXiv:2007.06488 [astro-ph.SR]
- Christensen-Dalsgaard J, Silva Aguirre V (2018) Ages for Exoplanet Host Stars. In: Deeg HJ, Belmonte JA (eds) Handbook of Exoplanets. p 184, https://doi.org/10.1007/978-3-319-55333-7_184
- Christiansen JL, Clarke BD, Burke CJ, et al (2015) Measuring Transit Signal Recovery in the Kepler Pipeline II: Detection Efficiency as Calculated in One Year of Data. ApJ810(2):95. <https://doi.org/10.1088/0004-637X/810/2/95>, arXiv:1507.05097 [astro-ph.EP]
- Christiansen JL, Clarke BD, Burke CJ, et al (2016) Measuring Transit Signal Recovery in the Kepler Pipeline. III. Completeness of the Q1-Q17 DR24 Planet Candidate Catalogue with Important Caveats for Occurrence Rate Calculations. The Astrophysical Journal 828(2):99. <https://doi.org/10.3847/0004-637X/828/2/99>, arXiv:1605.05729 [astro-ph.EP]
- Christiansen JL, Clarke BD, Burke CJ, et al (2020) Measuring Transit Signal Recovery in the Kepler Pipeline. IV. Completeness of the DR25 Planet Candidate Catalog. AJ160(4):159. <https://doi.org/10.3847/1538-3881/abab0b>, arXiv:2010.04796 [astro-ph.EP]
- Cifuentes C, Caballero JA, Cortés-Contreras M, et al (2020) CARMENES input catalogue of M dwarfs. V. Luminosities, colours, and spectral energy distributions. A&A642:A115. <https://doi.org/10.1051/0004-6361/202038295>, arXiv:2007.15077 [astro-ph.SR]
- Cimerman NP, Kuiper R, Ormel CW (2017) Hydrodynamics of embedded planets' first atmospheres - III. The role of radiation transport for super-Earth planets. MNRAS471(4):4662–4676. <https://doi.org/10.1093/mnras/stx1924>, arXiv:1707.08079 [astro-ph.EP]
- Clermont L, Jacobs J, Blain P, et al (2018) Automatized alignment of the focal plane assemblies on the PLATO cameras . In: Space Telescopes and Instrumentation 2018: Optical, Infrared, and Millimeter Wave, vol 10698. SPIE, pp 1902 – 1913, <https://doi.org/10.1117/12.2314167>, URL <https://doi.org/10.1117/12.2314167>
- Coelho HR, Chaplin WJ, Basu S, et al (2015) A test of the asteroseismic ν_{max} scaling relation for solar-like oscillations in main-sequence and subgiant stars. MNRAS451(3):3011–3020. <https://doi.org/10.1093/mnras/stv1175>, arXiv:1505.06087 [astro-ph.SR]
- Coleman GAL, Nelson RP (2016) On the formation of compact planetary systems via concurrent core accretion and migration. MNRAS457(3):2480–2500. <https://doi.org/10.1093/mnras/stw149>, arXiv:1601.03608 [astro-ph.EP]

- Coleman GAL, Nelson RP, Triaud AHMJ (2023) Global N-body simulations of circumbinary planet formation around Kepler-16 and -34 analogues I: Exploring the pebble accretion scenario. *MNRAS*522(3):4352–4373. <https://doi.org/10.1093/mnras/stad833>, [arXiv:2303.09899](https://arxiv.org/abs/2303.09899) [astro-ph.EP]
- Compton DL, Bedding TR, Stello D (2019) Asteroseismology of main-sequence F stars with Kepler: overcoming short mode lifetimes. *MNRAS*485(1):560–569. <https://doi.org/10.1093/mnras/stz432>, [arXiv:1902.05561](https://arxiv.org/abs/1902.05561) [astro-ph.SR]
- Correia ACM (2014) Transit light curve and inner structure of close-in planets. *A&A*570:L5. <https://doi.org/10.1051/0004-6361/201424733>, [arXiv:1410.5495](https://arxiv.org/abs/1410.5495) [astro-ph.EP]
- Corsaro E, De Ridder J (2014) DIAMONDS: A new Bayesian nested sampling tool. Application to peak bagging of solar-like oscillations. *A&A*571:A71. <https://doi.org/10.1051/0004-6361/201424181>, [arXiv:1408.2515](https://arxiv.org/abs/1408.2515) [astro-ph.IM]
- Corso AJ, Tassarolo E, Baccaro S, et al (2018) Rad-hard properties of the optical glass adopted for the PLATO space telescope refractive components. *Optics Express* 26(26):33841. <https://doi.org/10.1364/OE.26.033841>
- Creevey OL, Metcalfe TS, Schultheis M, et al (2017) Characterizing solar-type stars from full-length Kepler data sets using the Asteroseismic Modeling Portal. *A&A*601:A67. <https://doi.org/10.1051/0004-6361/201629496>, [arXiv:1612.08990](https://arxiv.org/abs/1612.08990) [astro-ph.SR]
- Csizmadia S, Pasternacki T, Dreyer C, et al (2013) The effect of stellar limb darkening values on the accuracy of the planet radii derived from photometric transit observations. *A&A*549:A9. <https://doi.org/10.1051/0004-6361/201219888>, [arXiv:1212.2372](https://arxiv.org/abs/1212.2372) [astro-ph.EP]
- Csizmadia S, Hellard H, Smith AMS (2019) An estimate of the k_2 Love number of WASP-18Ab from its radial velocity measurements. *A&A*623:A45. <https://doi.org/10.1051/0004-6361/201834376>, [arXiv:1812.04463](https://arxiv.org/abs/1812.04463) [astro-ph.EP]
- Csizmadia S, Smith AMS, Kálmán S, et al (2023) Power of wavelets in analyses of transit and phase curves in the presence of stellar variability and instrumental noise. I. Method and validation. *A&A*675:A106. <https://doi.org/10.1051/0004-6361/202141302>, [arXiv:2108.11822](https://arxiv.org/abs/2108.11822) [astro-ph.EP]
- Cunha MS, Roxburgh IW, Aguirre Børsen-Koch V, et al (2021) PLATO hare-and-hounds exercise: asteroseismic model fitting of main-sequence solar-like pulsators. *MNRAS*508(4):5864–5885. <https://doi.org/10.1093/mnras/stab2886>, [arXiv:2110.03332](https://arxiv.org/abs/2110.03332) [astro-ph.SR]
- Damiani C, Mathis S (2018) Influence of stellar structure, evolution, and rotation on the tidal damping of exoplanetary spin-orbit angles. *A&A*618:A90. <https://doi.org/>

[10.1051/0004-6361/201732538](https://doi.org/10.1051/0004-6361/201732538), [arXiv:1803.09661](https://arxiv.org/abs/1803.09661) [astro-ph.EP]

- Davies GR, Silva Aguirre V, Bedding TR, et al (2016) Oscillation frequencies for 35 Kepler solar-type planet-hosting stars using Bayesian techniques and machine learning. *MNRAS*456(2):2183–2195. <https://doi.org/10.1093/mnras/stv2593>, [arXiv:1511.02105](https://arxiv.org/abs/1511.02105) [astro-ph.SR]
- de Ridder J, Barban C, Baudin F, et al (2009) Non-radial oscillation modes with long lifetimes in giant stars. *Nature*459:398–400. <https://doi.org/10.1038/nature08022>
- Degroote P, Briquet M, Auvergne M, et al (2010) Detection of frequency spacings in the young O-type binary HD 46149 from CoRoT photometry. *A&A*519:A38. <https://doi.org/10.1051/0004-6361/201014543>, [arXiv:1006.3139](https://arxiv.org/abs/1006.3139) [astro-ph.SR]
- Deleuil M, Aigrain S, Moutou C, et al (2018) Planets, candidates, and binaries from the CoRoT/Exoplanet programme: the CoRoT transit catalogue. *ArXiv e-prints* [arXiv:1805.07164](https://arxiv.org/abs/1805.07164) [astro-ph.EP]
- Dorn C, Lichtenberg T (2021) Hidden Water in Magma Ocean Exoplanets. *ApJ*922(1):L4. <https://doi.org/10.3847/2041-8213/ac33af>, [arXiv:2110.15069](https://arxiv.org/abs/2110.15069) [astro-ph.EP]
- Dorn C, Khan A, Heng K, et al (2015) Can we constrain the interior structure of rocky exoplanets from mass and radius measurements? *A&A*577:A83. <https://doi.org/10.1051/0004-6361/201424915>, [arXiv:1502.03605](https://arxiv.org/abs/1502.03605) [astro-ph.EP]
- Dorn C, Hinkel NR, Venturini J (2017) Bayesian analysis of interiors of HD 219134b, Kepler-10b, Kepler-93b, CoRoT-7b, 55 Cnc e, and HD 97658b using stellar abundance proxies. *A&A*597:A38. <https://doi.org/10.1051/0004-6361/201628749>, [arXiv:1609.03909](https://arxiv.org/abs/1609.03909) [astro-ph.EP]
- Dorn C, Noack L, Rozel AB (2018) Outgassing on stagnant-lid super-Earths. *A&A*614:A18. <https://doi.org/10.1051/0004-6361/201731513>, [arXiv:1802.09264](https://arxiv.org/abs/1802.09264) [astro-ph.EP]
- Dressing CD, Charbonneau D (2013) The Occurrence Rate of Small Planets around Small Stars. *ApJ*767:95. <https://doi.org/10.1088/0004-637X/767/1/95>, [arXiv:1302.1647](https://arxiv.org/abs/1302.1647) [astro-ph.EP]
- Drażkowska J, Bitsch B, Lambrechts M, et al (2023) Planet Formation Theory in the Era of ALMA and Kepler: from Pebbles to Exoplanets. In: Inutsuka S, Aikawa Y, Muto T, et al (eds) *Astronomical Society of the Pacific Conference Series*, p 717, <https://doi.org/10.48550/arXiv.2203.09759>, [2203.09759](https://arxiv.org/abs/2203.09759)
- Elkins-Tanton LT, Seager S (2008) Coreless Terrestrial Exoplanets. *ApJ*688(1):628–635. <https://doi.org/10.1086/592316>, [arXiv:0808.1908](https://arxiv.org/abs/0808.1908) [astro-ph]

- Emsenhuber A, Cambioni S, Asphaug E, et al (2020) Realistic On-the-fly Outcomes of Planetary Collisions. II. Bringing Machine Learning to N-body Simulations. *ApJ*891(1):6. <https://doi.org/10.3847/1538-4357/ab6de5>, [arXiv:2001.00951](https://arxiv.org/abs/2001.00951) [astro-ph.EP]
- Emsenhuber A, Mordasini C, Burn R, et al (2021) The New Generation Planetary Population Synthesis (NGPPS). I. Bern global model of planet formation and evolution, model tests, and emerging planetary systems. *A&A*656:A69. <https://doi.org/10.1051/0004-6361/202038553>, [arXiv:2007.05561](https://arxiv.org/abs/2007.05561) [astro-ph.EP]
- ESA-SCI (2017) PLATO Definition Study Report (Red Book). ESA, URL <https://sci.esa.int/s/8rPyPew>
- Espinoza N, Jordán A (2015) Limb darkening and exoplanets: testing stellar model atmospheres and identifying biases in transit parameters. *MNRAS*450(2):1879–1899. <https://doi.org/10.1093/mnras/stv744>, [arXiv:1503.07020](https://arxiv.org/abs/1503.07020) [astro-ph.EP]
- Farnir M, Dupret MA, Buldgen G, et al (2020) Thorough characterisation of the 16 Cygni system. I. Forward seismic modelling with WhoSGLAd. *A&A*644:A37. <https://doi.org/10.1051/0004-6361/202038522>, [arXiv:2010.06495](https://arxiv.org/abs/2010.06495) [astro-ph.SR]
- Farnir M, Pinçon C, Dupret MA, et al (2021) Asteroseismology of evolved stars with EGGMiMoSA. I. Theoretical mixed-mode patterns from the subgiant to the RGB phase. *A&A*653:A126. <https://doi.org/10.1051/0004-6361/202141317>, [arXiv:2107.08021](https://arxiv.org/abs/2107.08021) [astro-ph.SR]
- Foreman-Mackey D, Hogg DW, Morton TD (2014) Exoplanet Population Inference and the Abundance of Earth Analogs from Noisy, Incomplete Catalogs. *ApJ*795(1):64. <https://doi.org/10.1088/0004-637X/795/1/64>, [arXiv:1406.3020](https://arxiv.org/abs/1406.3020) [astro-ph.EP]
- Fressin F, Torres G, Charbonneau D, et al (2013) The False Positive Rate of Kepler and the Occurrence of Planets. *ApJ*766:81. <https://doi.org/10.1088/0004-637X/766/2/81>, [arXiv:1301.0842](https://arxiv.org/abs/1301.0842) [astro-ph.EP]
- Fulton BJ, Petigura EA (2018) The California-Kepler Survey. VII. Precise Planet Radii Leveraging Gaia DR2 Reveal the Stellar Mass Dependence of the Planet Radius Gap. *AJ*156(6):264. <https://doi.org/10.3847/1538-3881/aae828>, [arXiv:1805.01453](https://arxiv.org/abs/1805.01453) [astro-ph.EP]
- Fulton BJ, Petigura EA, Howard AW, et al (2017) The California-Kepler Survey. III. A Gap in the Radius Distribution of Small Planets. *AJ*154(3):109. <https://doi.org/10.3847/1538-3881/aa80eb>, [arXiv:1703.10375](https://arxiv.org/abs/1703.10375) [astro-ph.EP]
- Gaia Collaboration, Prusti T, de Bruijne JHJ, et al (2016) The Gaia mission. *A&A*595:A1. <https://doi.org/10.1051/0004-6361/201629272>, [arXiv:1609.04153](https://arxiv.org/abs/1609.04153) [astro-ph.IM]

- Gaidos E (2013) Candidate Planets in the Habitable Zones of Kepler Stars. *ApJ*770:90. <https://doi.org/10.1088/0004-637X/770/2/90>, [arXiv:1301.2384](https://arxiv.org/abs/1301.2384) [astro-ph.EP]
- García RA, Ballot J (2019) Asteroseismology of solar-type stars. *Living Reviews in Solar Physics* 16(1):4. <https://doi.org/10.1007/s41116-019-0020-1>, [arXiv:1906.12262](https://arxiv.org/abs/1906.12262) [astro-ph.SR]
- García RA, Mathur S, Salabert D, et al (2010) CoRoT Reveals a Magnetic Activity Cycle in a Sun-Like Star. *Science* 329:1032–. <https://doi.org/10.1126/science.1191064>, [arXiv:1008.4399](https://arxiv.org/abs/1008.4399) [astro-ph.SR]
- García RA, Hekker S, Stello D, et al (2011) Preparation of Kepler light curves for asteroseismic analyses. *MNRAS*414(1):L6–L10. <https://doi.org/10.1111/j.1745-3933.2011.01042.x>, [arXiv:1103.0382](https://arxiv.org/abs/1103.0382) [astro-ph.SR]
- Garcia RA, Ceillier T, Salabert D, et al (2014) Towards asteroseismically calibrated age-rotation-activity relations for Kepler solar-like stars. *ArXiv e-prints* [arXiv:1403.7155](https://arxiv.org/abs/1403.7155) [astro-ph.SR]
- Garcia S, Van Reeth T, De Ridder J, et al (2022) Internal rotation and buoyancy travel time of 60 γ Doradus stars from uninterrupted TESS light curves spanning 352 days. *A&A*668:A137. <https://doi.org/10.1051/0004-6361/202244365>, [arXiv:2210.09526](https://arxiv.org/abs/2210.09526) [astro-ph.SR]
- Gardner JP, Mather JC, Clampin M, et al (2006) The James Webb Space Telescope. *Space Sci. Rev.*123:485–606. <https://doi.org/10.1007/s11214-006-8315-7>, [arXiv:astro-ph/0606175](https://arxiv.org/abs/astro-ph/0606175)
- Gent MR, Bergemann M, Serenelli A, et al (2022) The SAPP pipeline for the determination of stellar abundances and atmospheric parameters of stars in the core program of the PLATO mission. *A&A*658:A147. <https://doi.org/10.1051/0004-6361/202140863>, [arXiv:2111.06666](https://arxiv.org/abs/2111.06666) [astro-ph.SR]
- Gilliland RL, Brown TM, Christensen-Dalsgaard J, et al (2010) Kepler Asteroseismology Program: Introduction and First Results. *PASP*122(888):131. <https://doi.org/10.1086/650399>, [arXiv:1001.0139](https://arxiv.org/abs/1001.0139) [astro-ph.SR]
- Gillon M, Triaud AHMJ, Demory BO, et al (2017) Seven temperate terrestrial planets around the nearby ultracool dwarf star TRAPPIST-1. *Nature*542:456–460. <https://doi.org/10.1038/nature21360>, [arXiv:1703.01424](https://arxiv.org/abs/1703.01424) [astro-ph.EP]
- Godolt M, Tosi N, Stracke B, et al (2019) The habitability of stagnant-lid Earths around dwarf stars. *A&A*625:A12. <https://doi.org/10.1051/0004-6361/201834658>, [arXiv:1903.07298](https://arxiv.org/abs/1903.07298) [astro-ph.EP]
- Goodwin AJ, Russell DM, Galloway DK, et al (2020) Enhanced optical activity 12 d before X-ray activity, and a 4 d X-ray delay during outburst rise, in a low-mass

- X-ray binary. MNRAS498(3):3429–3439. <https://doi.org/10.1093/mnras/staa2588>, [arXiv:2006.02872](https://arxiv.org/abs/2006.02872) [astro-ph.HE]
- Goupil M (2017) Expected asteroseismic performances with the space project PLATO. In: European Physical Journal Web of Conferences, p 01003, <https://doi.org/10.1051/epjconf/201716001003>
- Greene TP, Bell TJ, Ducrot E, et al (2023) Thermal emission from the Earth-sized exoplanet TRAPPIST-1 b using JWST. Nature618(7963):39–42. <https://doi.org/10.1038/s41586-023-05951-7>, [arXiv:2303.14849](https://arxiv.org/abs/2303.14849) [astro-ph.EP]
- Grenfell JL, Godolt M, Cabrera J, et al (2020) Atmospheric Characterization via Broadband Color Filters on the PLANetary Transits and Oscillations of stars (PLATO) Mission. Experimental Astronomy 50(1):1–49. <https://doi.org/10.1007/s10686-020-09660-1>, [arXiv:2004.06396](https://arxiv.org/abs/2004.06396) [astro-ph.EP]
- Grießbach D, Witteck U, Paproth C (2021) The fine guidance system of the PLATO mission. In: ICSO 2020, vol 11852. SPIE, pp 1496 – 1506, URL <https://doi.org/10.1117/12.2599604>
- Gronoff G, Airapetian V, Hegyi B, et al (2020) Stellar Energetic Particle-driven Production of Biologically Relevant Molecules in Atmospheres of Young Earth-like Exoplanets Around Active G-K Stars. In: AGU Fall Meeting Abstracts, pp P007–0013
- Guerrero NM, Seager S, Huang CX, et al (2021) The TESS Objects of Interest Catalog from the TESS Prime Mission. ApJS254(2):39. <https://doi.org/10.3847/1538-4365/abefe1>, [arXiv:2103.12538](https://arxiv.org/abs/2103.12538) [astro-ph.EP]
- Gurgenashvili E, Zaqarashvili TV, Kukhianidze V, et al (2021) Rieger-type periodicity in the total irradiance of the Sun as a star during solar cycles 23–24. A&A653:A146. <https://doi.org/10.1051/0004-6361/202141370>
- Hall OJ, Davies GR, van Saders J, et al (2021) Weakened magnetic braking supported by asteroseismic rotation rates of Kepler dwarfs. Nature Astronomy 5:707–714. <https://doi.org/10.1038/s41550-021-01335-x>, [arXiv:2104.10919](https://arxiv.org/abs/2104.10919) [astro-ph.SR]
- Hamano K, Abe Y, Genda H (2013) Emergence of two types of terrestrial planet on solidification of magma ocean. Nature497(7451):607–610. <https://doi.org/10.1038/nature12163>
- Handberg R, Campante TL (2011) Bayesian peak-bagging of solar-like oscillators using MCMC: a comprehensive guide. A&A527:A56. <https://doi.org/10.1051/0004-6361/201015451>, [arXiv:1101.0084](https://arxiv.org/abs/1101.0084) [astro-ph.SR]
- Handberg R, Lund MN (2014) Automated preparation of Kepler time series of planet hosts for asteroseismic analysis. MNRAS445(3):2698–2709. <https://doi.org/>

[10.1093/mnras/stu1823](https://doi.org/10.1093/mnras/stu1823), [arXiv:1409.1366](https://arxiv.org/abs/1409.1366) [astro-ph.IM]

- Hatt E, Nielsen MB, Chaplin WJ, et al (2023) Catalogue of solar-like oscillators observed by TESS in 120-s and 20-s cadence. *A&A*669:A67. <https://doi.org/10.1051/0004-6361/202244579>, [arXiv:2210.09109](https://arxiv.org/abs/2210.09109) [astro-ph.SR]
- Hatzes AP, Rauer H (2015) A Definition for Giant Planets Based on the Mass-Density Relationship. *ApJ*810(2):L25. <https://doi.org/10.1088/2041-8205/810/2/L25>, [arXiv:1506.05097](https://arxiv.org/abs/1506.05097) [astro-ph.EP]
- Hekker S (2020) Scaling relations for solar-like oscillations: a review. *Frontiers in Astronomy and Space Sciences* 7:3. <https://doi.org/10.3389/fspas.2020.00003>, [arXiv:1907.10457](https://arxiv.org/abs/1907.10457) [astro-ph.SR]
- Hellard H, Csizmadia S, Padovan S, et al (2019) Retrieval of the Fluid Love Number k_2 in Exoplanetary Transit Curves. *ApJ*878(2):119. <https://doi.org/10.3847/1538-4357/ab2048>, [arXiv:1905.03171](https://arxiv.org/abs/1905.03171) [astro-ph.EP]
- Hellard H, Csizmadia S, Padovan S, et al (2020) HST/STIS Capability for Love Number Measurement of WASP-121b. *ApJ*889(1):66. <https://doi.org/10.3847/1538-4357/ab616e>, [arXiv:1912.05889](https://arxiv.org/abs/1912.05889) [astro-ph.EP]
- Heller R (2019) Analytic solutions to the maximum and average exoplanet transit depth for common stellar limb darkening laws. *A&A*623:A137. <https://doi.org/10.1051/0004-6361/201834620>, [arXiv:1901.01730](https://arxiv.org/abs/1901.01730) [astro-ph.EP]
- Heller R, Harre JV, Samadi R (2022) Transit least-squares survey. IV. Earth-like transiting planets expected from the PLATO mission. *A&A*665:A11. <https://doi.org/10.1051/0004-6361/202141640>, [arXiv:2206.02071](https://arxiv.org/abs/2206.02071) [astro-ph.EP]
- Hippke M, Heller R (2019) Optimized transit detection algorithm to search for periodic transits of small planets. *A&A*623:A39. <https://doi.org/10.1051/0004-6361/201834672>, [arXiv:1901.02015](https://arxiv.org/abs/1901.02015) [astro-ph.EP]
- Ho CSK, Van Eylen V (2023) A deep radius valley revealed by Kepler short cadence observations. *MNRAS*519(3):4056–4073. <https://doi.org/10.1093/mnras/stac3802>, [arXiv:2301.04062](https://arxiv.org/abs/2301.04062) [astro-ph.EP]
- Holcomb RJ, Robertson P, Hartigan P, et al (2022) SpinSpotter : An Automated Algorithm for Identifying Stellar Rotation Periods with Autocorrelation Analysis. *ApJ*936(2):138. <https://doi.org/10.3847/1538-4357/ac8990>, [arXiv:2206.10629](https://arxiv.org/abs/2206.10629) [astro-ph.SR]
- Howard AW, Marcy GW, Bryson ST, et al (2012) Planet Occurrence within 0.25 AU of Solar-type Stars from Kepler. *ApJS*201:15. <https://doi.org/10.1088/0067-0049/201/2/15>, [arXiv:1103.2541](https://arxiv.org/abs/1103.2541) [astro-ph.EP]

- Howell SB, Sobeck C, Haas M, et al (2014) The K2 Mission: Characterization and Early Results. *PASP*126(938):398. <https://doi.org/10.1086/676406>, [arXiv:1402.5163](https://arxiv.org/abs/1402.5163) [astro-ph.IM]
- Huang S, Ormel CW (2023) When, where, and how many planets end up in first-order resonances? *MNRAS*522(1):828–846. <https://doi.org/10.1093/mnras/stad1032>, [arXiv:2302.03070](https://arxiv.org/abs/2302.03070) [astro-ph.EP]
- Huber D, Zwintz K (2020) Solar-Like Oscillations: Lessons Learned & First Results from TESS. In: Neiner C, Weiss WW, Baade D, et al (eds) *Stars and their Variability Observed from Space*, pp 457–463, <https://doi.org/10.48550/arXiv.2007.02170>, [2007.02170](https://arxiv.org/abs/2007.02170)
- Huber D, Bedding TR, Stello D, et al (2011) Testing Scaling Relations for Solar-like Oscillations from the Main Sequence to Red Giants Using Kepler Data. *ApJ*743(2):143. <https://doi.org/10.1088/0004-637X/743/2/143>, [arXiv:1109.3460](https://arxiv.org/abs/1109.3460) [astro-ph.SR]
- Huber D, Chaplin WJ, Christensen-Dalsgaard J, et al (2013) Fundamental Properties of Kepler Planet-candidate Host Stars using Asteroseismology. *ApJ*767:127. <https://doi.org/10.1088/0004-637X/767/2/127>, [arXiv:1302.2624](https://arxiv.org/abs/1302.2624) [astro-ph.SR]
- Huber D, Silva Aguirre V, Matthews JM, et al (2014) Revised Stellar Properties of Kepler Targets for the Quarter 1-16 Transit Detection Run. *ApJS*211(1):2. <https://doi.org/10.1088/0067-0049/211/1/2>, [arXiv:1312.0662](https://arxiv.org/abs/1312.0662) [astro-ph.EP]
- Huber D, Zinn J, Bojsen-Hansen M, et al (2017) Asteroseismology and Gaia: Testing Scaling Relations Using 2200 Kepler Stars with TGAS Parallaxes. *ApJ*844(2):102. <https://doi.org/10.3847/1538-4357/aa75ca>, [arXiv:1705.04697](https://arxiv.org/abs/1705.04697) [astro-ph.SR]
- Huber D, White TR, Metcalfe TS, et al (2022) A 20 Second Cadence View of Solar-type Stars and Their Planets with TESS: Asteroseismology of Solar Analogs and a Recharacterization of π Men c. *AJ*163(2):79. <https://doi.org/10.3847/1538-3881/ac3000>, [arXiv:2108.09109](https://arxiv.org/abs/2108.09109) [astro-ph.SR]
- Izidoro A, Bitsch B, Raymond SN, et al (2021) Formation of planetary systems by pebble accretion and migration. Hot super-Earth systems from breaking compact resonant chains. *A&A*650:A152. <https://doi.org/10.1051/0004-6361/201935336>, [arXiv:1902.08772](https://arxiv.org/abs/1902.08772) [astro-ph.EP]
- Izidoro A, Schlichting HE, Isella A, et al (2022) The Exoplanet Radius Valley from Gas-driven Planet Migration and Breaking of Resonant Chains. *ApJ*939(2):L19. <https://doi.org/10.3847/2041-8213/ac990d>, [arXiv:2210.05595](https://arxiv.org/abs/2210.05595) [astro-ph.EP]
- Janssen N, De Ridder J, Seynaeve D, et al (2023) PlatoSim: An end-to-end PLATO camera simulator for modelling high-precision space-based photometry. *arXiv e-prints* [arXiv:2310.06985](https://arxiv.org/abs/2310.06985). <https://doi.org/10.48550/arXiv.2310.06985>,

[arXiv:2310.06985](https://arxiv.org/abs/2310.06985) [astro-ph.IM]

- Jannsen N, De Ridder J, Seynaeve D, et al (2024) PlatoSim: an end-to-end PLATO camera simulator for modelling high-precision space-based photometry. *A&A*681:A18. <https://doi.org/10.1051/0004-6361/202346701>, [arXiv:2310.06985](https://arxiv.org/abs/2310.06985) [astro-ph.IM]
- Jenkins JM, Doyle LR, Cullers DK (1996) A Matched Filter Method for Ground-Based Sub-Noise Detection of Terrestrial Extrasolar Planets in Eclipsing Binaries: Application to CM Draconis. *Icarus*119:244–260. <https://doi.org/10.1006/icar.1996.0018>
- Johansen A, Lambrechts M (2017) Forming Planets via Pebble Accretion. *Annual Review of Earth and Planetary Sciences* 45(1):359–387. <https://doi.org/10.1146/annurev-earth-063016-020226>
- Johansen A, Ronnet T, Bizzarro M, et al (2021) A pebble accretion model for the formation of the terrestrial planets in the Solar System. *Science Advances* 7(8):eabc0444. <https://doi.org/10.1126/sciadv.abc0444>, [arXiv:2102.08611](https://arxiv.org/abs/2102.08611) [astro-ph.EP]
- Jørgensen ACS, Montalbán J, Miglio A, et al (2020) Investigating surface correction relations for RGB stars. *MNRAS*495(4):4965–4980. <https://doi.org/10.1093/mnras/staa1480>, [arXiv:2004.13666](https://arxiv.org/abs/2004.13666) [astro-ph.SR]
- Kabath P, Eig Müller P, Erikson A, et al (2007) Characterization of COROT Target Fields with BEST: Identification of Periodic Variable Stars in the IR01 Field. *AJ*134:1560–1569. <https://doi.org/10.1086/521554>, [arXiv:0907.4883](https://arxiv.org/abs/0907.4883)
- Kajtazi K, Petit AC, Johansen A (2023) Mean motion resonance capture in the context of type I migration. *A&A*669:A44. <https://doi.org/10.1051/0004-6361/202244460>, [arXiv:2211.06181](https://arxiv.org/abs/2211.06181) [astro-ph.EP]
- Karoff C, Metcalfe TS, Santos ÂRG, et al (2018) The Influence of Metallicity on Stellar Differential Rotation and Magnetic Activity. *ApJ*852(1):46. <https://doi.org/10.3847/1538-4357/aaa026>, [arXiv:1711.07716](https://arxiv.org/abs/1711.07716) [astro-ph.SR]
- Kasting JF, Harman CE (2013) Extrasolar planets: Inner edge of the habitable zone. *Nature*504(7479):221–223. <https://doi.org/10.1038/504221a>
- Kellermann C, Becker A, Redmer R (2018) Interior structure models and fluid Love numbers of exoplanets in the super-Earth regime. *A&A*615:A39. <https://doi.org/10.1051/0004-6361/201731775>
- Kerins E, Bachelet E, Beaulieu JP, et al (2023) Magnifying nasa roman gbtds exoplanet science with coordinated observations by esa euclid. [2306.10210](https://arxiv.org/abs/2306.10210)

- Kiefer R, Schad A, Davies G, et al (2017) Stellar magnetic activity and variability of oscillation parameters: An investigation of 24 solar-like stars observed by Kepler. *A&A*598:A77. <https://doi.org/10.1051/0004-6361/201628469>, [arXiv:1611.02029](https://arxiv.org/abs/1611.02029) [astro-ph.SR]
- Kimura M, Osaki Y, Kato T (2020) KIC 9406652: A laboratory for tilted disks in cataclysmic variable stars. *PASJ*72(6):94. <https://doi.org/10.1093/pasj/psaa088>, [arXiv:2008.11328](https://arxiv.org/abs/2008.11328) [astro-ph.SR]
- Kislyakova K, Noack L (2020) Electromagnetic induction heating as a driver of volcanic activity on massive rocky planets. *A&A*636:L10. <https://doi.org/10.1051/0004-6361/202037924>, [arXiv:2004.14041](https://arxiv.org/abs/2004.14041) [astro-ph.EP]
- Kite ES, Manga M, Gaidos E (2009) Geodynamics and Rate of Volcanism on Massive Earth-like Planets. *ApJ*700(2):1732–1749. <https://doi.org/10.1088/0004-637X/700/2/1732>, [arXiv:0809.2305](https://arxiv.org/abs/0809.2305) [astro-ph]
- Kley W, Nelson RP (2012) Planet-Disk Interaction and Orbital Evolution. *ARA&A*50:211–249. <https://doi.org/10.1146/annurev-astro-081811-125523>, [arXiv:1203.1184](https://arxiv.org/abs/1203.1184) [astro-ph.EP]
- Koch DG, Borucki WJ, Basri G, et al (2010) Kepler Mission Design, Realized Photometric Performance, and Early Science. *ApJ*713:L79. <https://doi.org/10.1088/2041-8205/713/2/L79>, [arXiv:1001.0268](https://arxiv.org/abs/1001.0268) [astro-ph.EP]
- Kopparapu RK, Ramirez R, Kasting JF, et al (2013) Habitable Zones around Main-sequence Stars: New Estimates. *ApJ*765:131. <https://doi.org/10.1088/0004-637X/765/2/131>, [arXiv:1301.6674](https://arxiv.org/abs/1301.6674) [astro-ph.EP]
- Kopparapu RK, Hébrard E, Belikov R, et al (2018) Exoplanet Classification and Yield Estimates for Direct Imaging Missions. *ApJ*856(2):122. <https://doi.org/10.3847/1538-4357/aab205>, [arXiv:1802.09602](https://arxiv.org/abs/1802.09602) [astro-ph.EP]
- Kunimoto M, Matthews JM (2020) Searching the Entirety of Kepler Data. II. Occurrence Rate Estimates for FGK Stars. *AJ*159(6):248. <https://doi.org/10.3847/1538-3881/ab88b0>, [arXiv:2004.05296](https://arxiv.org/abs/2004.05296) [astro-ph.EP]
- Kunimoto M, Winn J, Ricker GR, et al (2022) Predicting the Exoplanet Yield of the TESS Prime and Extended Missions through Years 1-7. *AJ*163(6):290. <https://doi.org/10.3847/1538-3881/ac68e3>, [arXiv:2202.03656](https://arxiv.org/abs/2202.03656) [astro-ph.EP]
- Lai D (2012) Tidal dissipation in planet-hosting stars: damping of spin-orbit misalignment and survival of hot Jupiters. *MNRAS*423(1):486–492. <https://doi.org/10.1111/j.1365-2966.2012.20893.x>, [arXiv:1109.4703](https://arxiv.org/abs/1109.4703) [astro-ph.EP]
- Lambrechts M, Lega E, Nelson RP, et al (2019a) Quasi-static contraction during runaway gas accretion onto giant planets. *A&A*630:A82. <https://doi.org/10.1051/>

0004-6361/201834413, arXiv:1907.06362 [astro-ph.EP]

- Lambrechts M, Morbidelli A, Jacobson SA, et al (2019b) Formation of planetary systems by pebble accretion and migration. How the radial pebble flux determines a terrestrial-planet or super-Earth growth mode. *A&A*627:A83. <https://doi.org/10.1051/0004-6361/201834229>, arXiv:1902.08694 [astro-ph.EP]
- Lebreton Y, Reese DR (2020) SPInS, a pipeline for massive stellar parameter inference. A public Python tool to age-date, weigh, size up stars, and more. *A&A*642:A88. <https://doi.org/10.1051/0004-6361/202038602>, arXiv:2009.00037 [astro-ph.SR]
- Lesur G, Flock M, Ercolano B, et al (2023) Hydro-, Magnetohydro-, and Dust-Gas Dynamics of Protoplanetary Disks. In: Inutsuka S, Aikawa Y, Muto T, et al (eds) *Astronomical Society of the Pacific Conference Series*, p 465
- Li D, Mustill AJ, Davies MB, et al (2023) Making hot Jupiters in stellar clusters: The importance of binary exchange. *MNRAS*518(3):4265–4277. <https://doi.org/10.1093/mnras/stac3387>, arXiv:2211.16015 [astro-ph.EP]
- Li T, Bedding TR, Christensen-Dalsgaard J, et al (2020) Asteroseismology of 36 Kepler subgiants - II. Determining ages from detailed modelling. *MNRAS*495(3):3431–3462. <https://doi.org/10.1093/mnras/staa1350>, arXiv:2006.00901 [astro-ph.SR]
- Libbrecht KG (1992) On the Ultimate Accuracy of Solar Oscillation Frequency Measurements. *ApJ*387:712. <https://doi.org/10.1086/171119>
- Lichtenberg T (2021) Redox Hysteresis of Super-Earth Exoplanets from Magma Ocean Circulation. *ApJ*914(1):L4. <https://doi.org/10.3847/2041-8213/ac0146>, arXiv:2105.11208 [astro-ph.EP]
- Lichtenberg T, Clement MS (2022) Reduced Late Bombardment on Rocky Exoplanets around M Dwarfs. *ApJ*938(1):L3. <https://doi.org/10.3847/2041-8213/ac9521>, arXiv:2209.14037 [astro-ph.EP]
- Lichtenberg T, Golabek GJ, Burn R, et al (2019) A water budget dichotomy of rocky protoplanets from ^{26}Al -heating. *Nature Astronomy* 3:307–313. <https://doi.org/10.1038/s41550-018-0688-5>, arXiv:1902.04026 [astro-ph.EP]
- Lissauer JJ, Fabrycky DC, Ford EB, et al (2011) A closely packed system of low-mass, low-density planets transiting Kepler-11. *Nature*470:53–58. <https://doi.org/10.1038/nature09760>, arXiv:1102.0291 [astro-ph.EP]
- Liu B, Lambrechts M, Johansen A, et al (2019) Super-Earth masses sculpted by pebble isolation around stars of different masses. *A&A*632:A7. <https://doi.org/10.1051/0004-6361/201936309>, arXiv:1909.00759 [astro-ph.EP]

- Ludwig HG, Steffen M, Freytag B (2023) Effects of magnetic fields on the center-to-limb variation in solar-type stars. *A&A*679:A65. <https://doi.org/10.1051/0004-6361/202346783>
- Lund MN, Silva Aguirre V, Davies GR, et al (2017) Standing on the Shoulders of Dwarfs: the Kepler Asteroseismic LEGACY Sample. I. Oscillation Mode Parameters. *ApJ*835(2):172. <https://doi.org/10.3847/1538-4357/835/2/172>, [arXiv:1612.00436](https://arxiv.org/abs/1612.00436) [astro-ph.SR]
- Lundkvist MS, Kjeldsen H, Albrecht S, et al (2016) Hot super-Earths stripped by their host stars. *Nature Communications* 7:11201. <https://doi.org/10.1038/ncomms11201>, [arXiv:1604.05220](https://arxiv.org/abs/1604.05220) [astro-ph.EP]
- Magrin D, Munari M, Pagano I, et al (2010) PLATO: detailed design of the telescope optical units. In: *Proc. SPIE*, p 773124, <https://doi.org/10.1117/12.857237>
- Magrin D, Ragazzoni R, Bruno G, et al (2016) Radiation, Thermal Gradient and Weight: a threefold dilemma for PLATO. In: MacEwen HA, Fazio GG, Lystrup M, et al (eds) *Space Telescopes and Instrumentation 2016: Optical, Infrared, and Millimeter Wave*, p 990430, <https://doi.org/10.1117/12.2232579>
- Marchiori V, Samadi R, Fialho F, et al (2019) In-flight photometry extraction of PLATO targets. Optimal apertures for detecting extrasolar planets. *A&A*627:A71. <https://doi.org/10.1051/0004-6361/201935269>, [arXiv:1906.00892](https://arxiv.org/abs/1906.00892) [astro-ph.IM]
- Mathis S, Prat V, Amard L, et al (2018) Anisotropic turbulent transport in stably stratified rotating stellar radiation zones. *A&A*620:A22. <https://doi.org/10.1051/0004-6361/201629187>, [arXiv:1808.01814](https://arxiv.org/abs/1808.01814) [astro-ph.SR]
- Mathur S, Huber D, Batalha NM, et al (2017) Revised Stellar Properties of Kepler Targets for the Q1-17 (DR25) Transit Detection Run. *ApJS*229(2):30. <https://doi.org/10.3847/1538-4365/229/2/30>, [arXiv:1609.04128](https://arxiv.org/abs/1609.04128) [astro-ph.SR]
- Mathur S, García RA, Bugnet L, et al (2019) Revisiting the impact of stellar magnetic activity on the detection of solar-like oscillations by Kepler. *Frontiers in Astronomy and Space Sciences* 6:46. <https://doi.org/10.3389/fspas.2019.00046>, [arXiv:1907.01415](https://arxiv.org/abs/1907.01415) [astro-ph.SR]
- Mathur S, García RA, Breton S, et al (2022) Detections of solar-like oscillations in dwarfs and subgiants with Kepler DR25 short-cadence data. *A&A*657:A31. <https://doi.org/10.1051/0004-6361/202141168>, [arXiv:2109.14058](https://arxiv.org/abs/2109.14058) [astro-ph.SR]
- Matuszewski F, Nettelmann N, Cabrera J, et al (2023) Estimating the number of planets that PLATO can detect. *A&A*677:A133. <https://doi.org/10.1051/0004-6361/202245287>, [arXiv:2307.12163](https://arxiv.org/abs/2307.12163) [astro-ph.EP]

- Maxted PFL (2023) Limb darkening measurements from TESS and Kepler light curves of transiting exoplanets. *MNRAS*519(3):3723–3735. <https://doi.org/10.1093/mnras/stac3741>, [arXiv:2212.09117](https://arxiv.org/abs/2212.09117) [astro-ph.EP]
- McQuillan A, Aigrain S, Mazeh T (2013) Measuring the rotation period distribution of field M dwarfs with Kepler. *MNRAS*432:1203–1216. <https://doi.org/10.1093/mnras/stt536>, [arXiv:1303.6787](https://arxiv.org/abs/1303.6787) [astro-ph.SR]
- McQuillan A, Mazeh T, Aigrain S (2014a) Rotation Periods of 34,030 Kepler Main-sequence Stars: The Full Autocorrelation Sample. *ApJS*211:24. <https://doi.org/10.1088/0067-0049/211/2/24>, [arXiv:1402.5694](https://arxiv.org/abs/1402.5694) [astro-ph.SR]
- McQuillan A, Mazeh T, Aigrain S (2014b) Rotation Periods of 34,030 Kepler Main-sequence Stars: The Full Autocorrelation Sample. *ApJS*211(2):24. <https://doi.org/10.1088/0067-0049/211/2/24>, [arXiv:1402.5694](https://arxiv.org/abs/1402.5694) [astro-ph.SR]
- Metcalf TS, van Saders JL, Basu S, et al (2021) Magnetic and Rotational Evolution of ρ CrB from Asteroseismology with TESS. *ApJ*921(2):122. <https://doi.org/10.3847/1538-4357/ac1f19>, [arXiv:2108.01088](https://arxiv.org/abs/2108.01088) [astro-ph.SR]
- Michel E, Baglin A, Weiss WW, et al (2008) First asteroseismic results from CoRoT. *Communications in Asteroseismology* 157:69
- Miglio A, Chiappini C, Morel T, et al (2013) Galactic archaeology: mapping and dating stellar populations with asteroseismology of red-giant stars. *MNRAS*429(1):423–428. <https://doi.org/10.1093/mnras/sts345>, [arXiv:1211.0146](https://arxiv.org/abs/1211.0146) [astro-ph.GA]
- Miglio A, Chiappini C, Mosser B, et al (2017) PLATO as it is : A legacy mission for Galactic archaeology. *Astronomische Nachrichten* 338(6):644–661. <https://doi.org/10.1002/asna.201713385>, [arXiv:1706.03778](https://arxiv.org/abs/1706.03778) [astro-ph.SR]
- Millholland S, Wang S, Laughlin G (2017) Kepler Multi-planet Systems Exhibit Unexpected Intra-system Uniformity in Mass and Radius. *ApJ*849(2):L33. <https://doi.org/10.3847/2041-8213/aa9714>, [arXiv:1710.11152](https://arxiv.org/abs/1710.11152) [astro-ph.EP]
- Mishra L, Alibert Y, Leleu A, et al (2021) The New Generation Planetary Population Synthesis (NGPPS) VI. Introducing KOBE: Kepler Observes Bern Exoplanets. Theoretical perspectives on the architecture of planetary systems: Peas in a pod. *A&A*656:A74. <https://doi.org/10.1051/0004-6361/202140761>, [arXiv:2105.12745](https://arxiv.org/abs/2105.12745) [astro-ph.EP]
- Mombarg JSG, Van Reeth T, Aerts C (2021) Constraining stellar evolution theory with asteroseismology of γ Doradus stars using deep learning. *A&A*, in press [arXiv:2103.13394](https://arxiv.org/abs/2103.13394). [arXiv:2103.13394](https://arxiv.org/abs/2103.13394) [astro-ph.SR]
- Montalbán J, Miglio A, Noels A, et al (2013) Testing Convective-core Overshooting Using Period Spacings of Dipole Modes in Red Giants. *ApJ*766(2):118. <https://doi.org/10.1088/0004-6361/125713>

- [org/10.1088/0004-637X/766/2/118](https://doi.org/10.1088/0004-637X/766/2/118), [arXiv:1302.3173](https://arxiv.org/abs/1302.3173) [astro-ph.SR]
- Montalto M, Piotto G, Marrese PM, et al (2021) The all-sky PLATO input catalogue. *A&A*653:A98. <https://doi.org/10.1051/0004-6361/202140717>, [arXiv:2108.13712](https://arxiv.org/abs/2108.13712) [astro-ph.EP]
- Moore K, Cowan NB (2020) Keeping M-Earths habitable in the face of atmospheric loss by sequestering water in the mantle. *MNRAS*496(3):3786–3795. <https://doi.org/10.1093/mnras/staa1796>, [arXiv:2006.08514](https://arxiv.org/abs/2006.08514) [astro-ph.EP]
- Morbidelli A, Lunine JJ, O’Brien DP, et al (2012) Building Terrestrial Planets. *Annual Review of Earth and Planetary Sciences* 40(1):251–275. <https://doi.org/10.1146/annurev-earth-042711-105319>, [arXiv:1208.4694](https://arxiv.org/abs/1208.4694) [astro-ph.EP]
- Morel T, Creevey OL, Montalbán J, et al (2021) Testing abundance-age relations beyond solar analogues with Kepler LEGACY stars. *A&A*646:A78. <https://doi.org/10.1051/0004-6361/202039212>, [arXiv:2011.04481](https://arxiv.org/abs/2011.04481) [astro-ph.SR]
- Moreno J, Vielba E, Manjón A, et al (2019) PLATO FPA. focal plane assembly of PLATO instrument. In: *ICSO 2018*, <https://doi.org/10.1117/12.2536050>
- Morris BM, Bobra MG, Agol E, et al (2020) The stellar variability noise floor for transiting exoplanet photometry with PLATO. *MNRAS*493(4):5489–5498. <https://doi.org/10.1093/mnras/staa618>, [arXiv:2002.08072](https://arxiv.org/abs/2002.08072) [astro-ph.EP]
- Mosser B, Goupil MJ, Belkacem K, et al (2012) Spin down of the core rotation in red giants. *A&A*548:A10. <https://doi.org/10.1051/0004-6361/201220106>, [arXiv:1209.3336](https://arxiv.org/abs/1209.3336) [astro-ph.SR]
- Müller S, Helled R (2023) Warm giant exoplanet characterisation: current state, challenges and outlook. *arXiv e-prints* [arXiv:2304.12782](https://arxiv.org/abs/2304.12782). <https://doi.org/10.48550/arXiv.2304.12782>, [arXiv:2304.12782](https://arxiv.org/abs/2304.12782) [astro-ph.EP]
- Namekata K, Sakaue T, Watanabe K, et al (2017) Statistical Studies of Solar White-light Flares and Comparisons with Superflares on Solar-type Stars. *ApJ*851(2):91. <https://doi.org/10.3847/1538-4357/aa9b34>, [arXiv:1710.11325](https://arxiv.org/abs/1710.11325) [astro-ph.SR]
- Nascimbeni V, Piotto G, Börner A, et al (2022) The PLATO field selection process. I. Identification and content of the long-pointing fields. *A&A*658:A31. <https://doi.org/10.1051/0004-6361/202142256>, [arXiv:2110.13924](https://arxiv.org/abs/2110.13924) [astro-ph.EP]
- Nelson RP, Lega E, Morbidelli A (2023) Gas accretion onto Jupiter mass planets in discs with laminar accretion flows. *A&A*670:A113. <https://doi.org/10.1051/0004-6361/202244885>, [arXiv:2212.08012](https://arxiv.org/abs/2212.08012) [astro-ph.EP]
- Nielsen EL, Liu MC, Wahhaj Z, et al (2013) The Gemini NICI Planet-Finding Campaign: The Frequency of Giant Planets around Young B and A Stars. *ApJ*776:4.

- <https://doi.org/10.1088/0004-637X/776/1/4>, [arXiv:1306.1233](https://arxiv.org/abs/1306.1233) [astro-ph.EP]
- Nielsen MB, Ball WH, Standing MR, et al (2020) TESS asteroseismology of the known planet host star λ^2 Fornacis. *A&A*641:A25. <https://doi.org/10.1051/0004-6361/202037461>, [arXiv:2007.00497](https://arxiv.org/abs/2007.00497) [astro-ph.SR]
- Nissen PE, Silva Aguirre V, Christensen-Dalsgaard J, et al (2017) High-precision abundances of elements in Kepler LEGACY stars. Verification of trends with stellar age. *A&A*608:A112. <https://doi.org/10.1051/0004-6361/201731845>, [arXiv:1710.03544](https://arxiv.org/abs/1710.03544) [astro-ph.SR]
- Nissen PE, Christensen-Dalsgaard J, Mosumgaard JR, et al (2020) High-precision abundances of elements in solar-type stars. Evidence of two distinct sequences in abundance-age relations. *A&A*640:A81. <https://doi.org/10.1051/0004-6361/202038300>, [arXiv:2006.06013](https://arxiv.org/abs/2006.06013) [astro-ph.SR]
- Noll A, Deheuvels S, Ballot J (2021) Probing core overshooting using subgiant asteroseismology: the case of KIC10273246. *arXiv e-prints* [arXiv:2101.11025](https://arxiv.org/abs/2101.11025) [astro-ph.SR]
- Nsamba B, Campante TL, Monteiro MJPF, et al (2018a) Asteroseismic modelling of solar-type stars: internal systematics from input physics and surface correction methods. *MNRAS*477(4):5052–5063. <https://doi.org/10.1093/mnras/sty948>, [arXiv:1804.04935](https://arxiv.org/abs/1804.04935) [astro-ph.SR]
- Nsamba B, Monteiro MJPF, Campante TL, et al (2018b) α Centauri A as a potential stellar model calibrator: establishing the nature of its core. *MNRAS*479(1):L55–L59. <https://doi.org/10.1093/mnrasl/sly092>, [arXiv:1805.09103](https://arxiv.org/abs/1805.09103) [astro-ph.SR]
- Nsamba B, Moedas N, Campante TL, et al (2021) Asteroseismic modelling of solar-type stars: a deeper look at the treatment of initial helium abundance. *MNRAS*500(1):54–65. <https://doi.org/10.1093/mnras/staa3228>, [arXiv:2010.07593](https://arxiv.org/abs/2010.07593) [astro-ph.SR]
- Ortenzi G, Noack L, Sohl F, et al (2020) Mantle redox state drives outgassing chemistry and atmospheric composition of rocky planets. *Scientific Reports* 10:10907. <https://doi.org/10.1038/s41598-020-67751-7>
- Osaki Y, Kato T (2013) Study of Superoutbursts and Superhumps in SU UMa Stars by the Kepler Light Curves of V344 Lyrae and V1504 Cygni. *PASJ*65:95. <https://doi.org/10.1093/pasj/65.5.95>, [arXiv:1305.5877](https://arxiv.org/abs/1305.5877) [astro-ph.SR]
- Otegi JF, Dorn C, Helled R, et al (2020) Impact of the measured parameters of exoplanets on the inferred internal structure. *A&A*640:A135. <https://doi.org/10.1051/0004-6361/202038006>, [arXiv:2006.12353](https://arxiv.org/abs/2006.12353) [astro-ph.EP]

- Padovan S, Spohn T, Baumeister P, et al (2018) Matrix-propagator approach to compute fluid Love numbers and applicability to extrasolar planets. *A&A*620:A178. <https://doi.org/10.1051/0004-6361/201834181>, [arXiv:1810.10064](https://arxiv.org/abs/1810.10064) [astro-ph.EP]
- Panahi A, Mazeh T, Zucker S, et al (2022) Gaia-TESS synergy: improving the identification of transit candidates. *A&A*667:A14. <https://doi.org/10.1051/0004-6361/202244207>, [arXiv:2209.05845](https://arxiv.org/abs/2209.05845) [astro-ph.EP]
- Papaloizou JCB (2011) Tidal interactions in multi-planet systems. *Celestial Mechanics and Dynamical Astronomy* 111(1-2):83–103. <https://doi.org/10.1007/s10569-011-9344-4>, [arXiv:1107.4488](https://arxiv.org/abs/1107.4488) [astro-ph.EP]
- Passegger VM, Schweitzer A, Shulyak D, et al (2019) The CARMENES search for exoplanets around M dwarfs. Photospheric parameters of target stars from high-resolution spectroscopy. II. Simultaneous multiwavelength range modeling of activity insensitive lines. *A&A*627:A161. <https://doi.org/10.1051/0004-6361/201935679>, [arXiv:1907.00807](https://arxiv.org/abs/1907.00807) [astro-ph.SR]
- Patel JA, Espinoza N (2022) Empirical Limb-darkening Coefficients and Transit Parameters of Known Exoplanets from TESS. *AJ*163(5):228. <https://doi.org/10.3847/1538-3881/ac5f55>, [arXiv:2203.05661](https://arxiv.org/abs/2203.05661) [astro-ph.EP]
- Pertenais M, Cabrera J, Griessbach D, et al (2021a) Overview of PLATO’s cameras on-ground and in-orbit calibration and characterisation. In: *ICSO 2020*, vol 11852. SPIE, pp 97 – 109, URL <https://doi.org/10.1117/12.2599149>
- Pertenais M, Cabrera J, Paproth C, et al (2021b) The unique field-of-view and focusing budgets of PLATO. In: *ICSO 2020*, vol 11852. SPIE, pp 2043 – 2054, URL <https://doi.org/10.1117/12.2599820>
- Petigura EA, Howard AW, Marcy GW (2013) Prevalence of Earth-size planets orbiting Sun-like stars. *Proceedings of the National Academy of Science* 110(48):19273–19278. <https://doi.org/10.1073/pnas.1319909110>, [arXiv:1311.6806](https://arxiv.org/abs/1311.6806) [astro-ph.EP]
- Pierens A, Nelson RP, McNally CP (2021) Vertical settling of pebbles in turbulent circumbinary discs and the in situ formation of circumbinary planets. *MNRAS*508(4):4806–4815. <https://doi.org/10.1093/mnras/stab2853>, [arXiv:2109.14466](https://arxiv.org/abs/2109.14466) [astro-ph.EP]
- Plotnykov M, Valencia D (2020) Chemical fingerprints of formation in rocky super-Earths’ data. *MNRAS*499(1):932–947. <https://doi.org/10.1093/mnras/staa2615>, [arXiv:2010.06480](https://arxiv.org/abs/2010.06480) [astro-ph.EP]
- Pollacco D, Skillen I, Cameron A, et al (2006) The WASP Project and SuperWASP Camera. *Ap&SS*304:253–255. <https://doi.org/10.1007/s10509-006-9124-x>

- Qiao L, Coleman GAL, Haworth TJ (2023) Planet formation via pebble accretion in externally photoevaporating discs. *MNRAS*522(2):1939–1950. <https://doi.org/10.1093/mnras/stad944>, [arXiv:2303.15177](https://arxiv.org/abs/2303.15177) [astro-ph.EP]
- Rauer H, Catala C, Aerts C, et al (2014) The PLATO 2.0 mission. *Experimental Astronomy* 38:249–330. <https://doi.org/10.1007/s10686-014-9383-4>, [arXiv:1310.0696](https://arxiv.org/abs/1310.0696) [astro-ph.EP]
- Reese DR, Chaplin WJ, Davies GR, et al (2016) SpaceInn hare-and-hounds exercise: Estimation of stellar properties using space-based asteroseismic data. *A&A*592:A14. <https://doi.org/10.1051/0004-6361/201527987>, [arXiv:1604.08404](https://arxiv.org/abs/1604.08404) [astro-ph.SR]
- Reinhold T, Shapiro AI, Witzke V, et al (2021) Where Have All the Solar-like Stars Gone? Rotation Period Detectability at Various Inclinations and Metallicities. *ApJ*908(2):L21. <https://doi.org/10.3847/2041-8213/abde46>, [arXiv:2101.11426](https://arxiv.org/abs/2101.11426) [astro-ph.SR]
- Reinhold T, Shapiro AI, Solanki SK, et al (2022) Measuring Periods in Aperiodic Light Curves—Applying the GPS Method to Infer the Rotation Periods of Solar-like Stars. *ApJ*938(1):L1. <https://doi.org/10.3847/2041-8213/ac937a>, [arXiv:2209.12593](https://arxiv.org/abs/2209.12593) [astro-ph.SR]
- Rendle BM, Buldgen G, Miglio A, et al (2019) AIMS - a new tool for stellar parameter determinations using asteroseismic constraints. *MNRAS*484(1):771–786. <https://doi.org/10.1093/mnras/stz031>, [arXiv:1901.02663](https://arxiv.org/abs/1901.02663) [astro-ph.SR]
- Ricker GR, Winn JN, Vanderspek R, et al (2015) Transiting Exoplanet Survey Satellite (TESS). *Journal of Astronomical Telescopes, Instruments, and Systems* 1(1):014003. <https://doi.org/10.1117/1.JATIS.1.1.014003>
- Rieder S, Kenworthy MA (2016) Constraints on the size and dynamics of the J1407b ring system. *A&A*596:A9. <https://doi.org/10.1051/0004-6361/201629567>, [arXiv:1609.08485](https://arxiv.org/abs/1609.08485) [astro-ph.EP]
- Rodrigues TS, Bossini D, Miglio A, et al (2017) Determining stellar parameters of asteroseismic targets: going beyond the use of scaling relations. *MNRAS*467(2):1433–1448. <https://doi.org/10.1093/mnras/stx120>, [arXiv:1701.04791](https://arxiv.org/abs/1701.04791) [astro-ph.SR]
- Rodríguez-López C (2019) The quest for pulsating M dwarf stars. *Frontiers in Astronomy and Space Sciences* 6:76
- Rodríguez-López C, Gizis JE, MacDonald J, et al (2015) M dwarf search for pulsations within Kepler Guest Observer programme. *MNRAS*446(3):2613–2620
- Rogers JG, Gupta A, Owen JE, et al (2021) Photoevaporation versus core-powered mass-loss: model comparison with the 3D radius gap. *MNRAS*508(4):5886–5902.

- <https://doi.org/10.1093/mnras/stab2897>, [arXiv:2105.03443](https://arxiv.org/abs/2105.03443) [astro-ph.EP]
- Rogers LA, Seager S (2010) A Framework for Quantifying the Degeneracies of Exoplanet Interior Compositions. *ApJ*712(2):974–991. <https://doi.org/10.1088/0004-637X/712/2/974>, [arXiv:0912.3288](https://arxiv.org/abs/0912.3288) [astro-ph.EP]
- Russell DM, Bramich DM, Lewis F, et al (2019) Optical precursors to X-ray binary outbursts. *Astronomische Nachrichten* 340(4):278–283. <https://doi.org/10.1002/asna.201913610>, [arXiv:1903.04519](https://arxiv.org/abs/1903.04519) [astro-ph.HE]
- Samadi R, Ludwig H, Belkacem K, et al (2010) The CoRoT target HD 49933 . II. Comparison of theoretical mode amplitudes with observations. *A&A*509:A16. <https://doi.org/10.1051/0004-6361/200911868>, [arXiv:0910.4037](https://arxiv.org/abs/0910.4037) [astro-ph.SR]
- Samadi R, Deru A, Reese D, et al (2019) The PLATO Solar-like Light-curve Simulator. A tool to generate realistic stellar light-curves with instrumental effects representative of the PLATO mission. *Astronomy and Astrophysics* 624:A117. <https://doi.org/10.1051/0004-6361/201834822>, [arXiv:1903.02747](https://arxiv.org/abs/1903.02747) [astro-ph.IM]
- Santerne A, Fressin F, Díaz RF, et al (2013) The contribution of secondary eclipses as astrophysical false positives to exoplanet transit surveys. *A&A*557:A139. <https://doi.org/10.1051/0004-6361/201321475>, [arXiv:1307.2003](https://arxiv.org/abs/1307.2003) [astro-ph.EP]
- Santos ARG, García RA, Mathur S, et al (2019) Surface Rotation and Photometric Activity for Kepler Targets. I. M and K Main-sequence Stars. *ApJS*244(1):21. <https://doi.org/10.3847/1538-4365/ab3b56>, [arXiv:1908.05222](https://arxiv.org/abs/1908.05222) [astro-ph.SR]
- Santos ARG, Breton SN, Mathur S, et al (2021) Surface Rotation and Photometric Activity for Kepler Targets. II. G and F Main-sequence Stars and Cool Subgiant Stars. *ApJS*255(1):17. <https://doi.org/10.3847/1538-4365/ac033f>, [arXiv:2107.02217](https://arxiv.org/abs/2107.02217) [astro-ph.SR]
- Scaringi S, de Martino D, Buckley DAH, et al (2022a) An accreting white dwarf displaying fast transitional mode switching. *Nature Astronomy* 6:98–102. <https://doi.org/10.1038/s41550-021-01494-x>, [arXiv:2110.09124](https://arxiv.org/abs/2110.09124) [astro-ph.SR]
- Scaringi S, Groot PJ, Knigge C, et al (2022b) Localized thermonuclear bursts from accreting magnetic white dwarfs. *Nature*604(7906):447–450. <https://doi.org/10.1038/s41586-022-04495-6>, [arXiv:2204.09070](https://arxiv.org/abs/2204.09070) [astro-ph.HE]
- Schlecker M, Apai D, Lichtenberg T, et al (2023) The imprint of global magma oceans on exoplanet demographics. In: *American Astronomical Society Meeting Abstracts*, p 145.05
- Schneider AD, Bitsch B (2021) How drifting and evaporating pebbles shape giant planets. I. Heavy element content and atmospheric C/O. *A&A*654:A71. <https://doi.org/10.1051/0004-6361/202039640>, [arXiv:2105.13267](https://arxiv.org/abs/2105.13267) [astro-ph.EP]

- Schulze JG, Wang J, Johnson JA, et al (2021) On the Probability That a Rocky Planet’s Composition Reflects Its Host Star. *Planetary Sciences Journal*2(3):113. <https://doi.org/10.3847/PSJ/abcaa8>, [arXiv:2011.08893](https://arxiv.org/abs/2011.08893) [astro-ph.EP]
- Seager S, Kuchner M, Hier-Majumder CA, et al (2007) Mass-Radius Relationships for Solid Exoplanets. *ApJ*669(2):1279–1297. <https://doi.org/10.1086/521346>, [arXiv:0707.2895](https://arxiv.org/abs/0707.2895) [astro-ph]
- Serenelli A, Johnson J, Huber D, et al (2017) The First APOKASC Catalog of Kepler Dwarf and Subgiant Stars. *ApJS*233(2):23. <https://doi.org/10.3847/1538-4365/aa97df>, [arXiv:1710.06858](https://arxiv.org/abs/1710.06858) [astro-ph.SR]
- Serenelli A, Weiss A, Aerts C, et al (2021) Weighing stars from birth to death: mass determination methods across the HRD. *A&A Rev.*29(1):4. <https://doi.org/10.1007/s00159-021-00132-9>, [arXiv:2006.10868](https://arxiv.org/abs/2006.10868) [astro-ph.SR]
- Shkolnik E, Walker GAH, Bohlender DA (2003) Evidence for Planet-induced Chromospheric Activity on HD 179949. *ApJ*597(2):1092–1096. <https://doi.org/10.1086/378583>
- Silburt A, Gaidos E, Wu Y (2015) A Statistical Reconstruction of the Planet Population around Kepler Solar-type Stars. *ApJ*799(2):180. <https://doi.org/10.1088/0004-637X/799/2/180>, [arXiv:1406.6048](https://arxiv.org/abs/1406.6048) [astro-ph.EP]
- Silva Aguirre V, Davies GR, Basu S, et al (2015) Ages and fundamental properties of Kepler exoplanet host stars from asteroseismology. *MNRAS*452(2):2127–2148. <https://doi.org/10.1093/mnras/stv1388>, [arXiv:1504.07992](https://arxiv.org/abs/1504.07992) [astro-ph.SR]
- Silva Aguirre V, Lund MN, Antia HM, et al (2017) Standing on the Shoulders of Dwarfs: the Kepler Asteroseismic LEGACY Sample. II. Radii, Masses, and Ages. *ApJ*835(2):173. <https://doi.org/10.3847/1538-4357/835/2/173>, [arXiv:1611.08776](https://arxiv.org/abs/1611.08776) [astro-ph.SR]
- Skumanich A (1972) Time Scales for Ca II Emission Decay, Rotational Braking, and Lithium Depletion. *ApJ*171:565. <https://doi.org/10.1086/151310>
- Spergel D, Gehrels N, Baltay C, et al (2015) Wide-Field Infrared Survey Telescope—Astrophysics Focused Telescope Assets WFIRST-AFTA 2015 Report. *arXiv e-prints* [arXiv:1503.03757](https://arxiv.org/abs/1503.03757). <https://doi.org/10.48550/arXiv.1503.03757>, [arXiv:1503.03757](https://arxiv.org/abs/1503.03757) [astro-ph.IM]
- Stapelfeldt K, Rauer H, Roberge A, et al (2021) Space Missions for Exoplanet Science. In: Madhusudhan N (ed) *ExoFrontiers; Big Questions in Exoplanetary Science*. p 9–1, <https://doi.org/10.1088/2514-3433/abfa8fch9>
- Stello D, Chaplin WJ, Basu S, et al (2009) The relation between $\Delta\nu$ and ν_{max} for solar-like oscillations. *MNRAS*400(1):L80–L84. <https://doi.org/10.1111/j.>

- 1745-3933.2009.00767.x, [arXiv:0909.5193](https://arxiv.org/abs/0909.5193) [astro-ph.SR]
- Still M, Howell SB, Wood MA, et al (2010) Quiescent Superhumps Detected in the Dwarf Nova V344 Lyrae by Kepler. *ApJ*717(2):L113–L117. <https://doi.org/10.1088/2041-8205/717/2/L113>, [arXiv:1006.1796](https://arxiv.org/abs/1006.1796) [astro-ph.SR]
- Strugarek A, Beaudoin P, Charbonneau P, et al (2018) On the Sensitivity of Magnetic Cycles in Global Simulations of Solar-like Stars. *ApJ*863(1):35. <https://doi.org/10.3847/1538-4357/aacf9e>, [arXiv:1806.09484](https://arxiv.org/abs/1806.09484) [astro-ph.SR]
- Strugarek A, Brun AS, Donati JF, et al (2019) Chasing Star-Planet Magnetic Interactions: The Case of Kepler-78. *ApJ*881(2):136. <https://doi.org/10.3847/1538-4357/ab2ed5>, [arXiv:1907.01020](https://arxiv.org/abs/1907.01020) [astro-ph.EP]
- Sullivan PW, Winn JN, Berta-Thompson ZK, et al (2015) The Transiting Exoplanet Survey Satellite: Simulations of Planet Detections and Astrophysical False Positives. *ApJ*809:77. <https://doi.org/10.1088/0004-637X/809/1/77>, [arXiv:1506.03845](https://arxiv.org/abs/1506.03845) [astro-ph.EP]
- Thomas DM, Wood MA (2015) The Emergence of Negative Superhumps in Cataclysmic Variables: Smoothed Particle Hydrodynamics Simulations. *ApJ*803(2):55. <https://doi.org/10.1088/0004-637X/803/2/55>, [arXiv:1602.06314](https://arxiv.org/abs/1602.06314) [astro-ph.SR]
- Tilley MA, Segura A, Meadows V, et al (2019) Modeling Repeated M Dwarf Flaring at an Earth-like Planet in the Habitable Zone: Atmospheric Effects for an Unmagnetized Planet. *Astrobiology* 19(1):64–86. <https://doi.org/10.1089/ast.2017.1794>, [arXiv:1711.08484](https://arxiv.org/abs/1711.08484) [astro-ph.EP]
- Tinetti G, Drossart P, Eccleston P, et al (2018) A chemical survey of exoplanets with ARIEL. *Experimental Astronomy* 46(1):135–209. <https://doi.org/10.1007/s10686-018-9598-x>
- Tkachenko A, Aerts C, Yakushechkin A, et al (2013) Detection of a large sample of γ Doradus stars from Kepler space photometry and high-resolution ground-based spectroscopy. *A&A*556:A52. <https://doi.org/10.1051/0004-6361/201220978>, [arXiv:1305.6722](https://arxiv.org/abs/1305.6722) [astro-ph.SR]
- Traub WA (2012) Terrestrial, Habitable-zone Exoplanet Frequency from Kepler. *ApJ*745:20. <https://doi.org/10.1088/0004-637X/745/1/20>, [arXiv:1109.4682](https://arxiv.org/abs/1109.4682) [astro-ph.EP]
- Turbet M, Ehrenreich D, Lovis C, et al (2019) The runaway greenhouse radius inflation effect. An observational diagnostic to probe water on Earth-sized planets and test the habitable zone concept. *A&A*628:A12. <https://doi.org/10.1051/0004-6361/201935585>, [arXiv:1906.03527](https://arxiv.org/abs/1906.03527) [astro-ph.EP]

- Valencia D, Sasselov DD, O’Connell RJ (2007) Detailed Models of Super-Earths: How Well Can We Infer Bulk Properties? *ApJ*665(2):1413–1420. <https://doi.org/10.1086/519554>, [arXiv:0704.3454](https://arxiv.org/abs/0704.3454) [astro-ph]
- van Amerongen S, Bovenschen H, van Paradijs J (1987) Wavelength dependence of superhumps in VW Hyi. *MNRAS*229:245–251. <https://doi.org/10.1093/mnras/229.2.245>
- Van Cleve JE, Caldwell DA (2009) Kepler Instrument Handbook (KSCI-19033). NASA
- Van Eylen V, Albrecht S (2015) Eccentricity from Transit Photometry: Small Planets in Kepler Multi-planet Systems Have Low Eccentricities. *ApJ*808(2):126. <https://doi.org/10.1088/0004-637X/808/2/126>, [arXiv:1505.02814](https://arxiv.org/abs/1505.02814) [astro-ph.EP]
- Van Eylen V, Agentoft C, Lundkvist MS, et al (2018) An asteroseismic view of the radius valley: stripped cores, not born rocky. *MNRAS*479(4):4786–4795. <https://doi.org/10.1093/mnras/sty1783>, [arXiv:1710.05398](https://arxiv.org/abs/1710.05398) [astro-ph.EP]
- Van Eylen V, Albrecht S, Huang X, et al (2019) The Orbital Eccentricity of Small Planet Systems. *AJ*157(2):61. <https://doi.org/10.3847/1538-3881/aaf22f>, [arXiv:1807.00549](https://arxiv.org/abs/1807.00549) [astro-ph.EP]
- Van Reeth T, Tkachenko A, Aerts C, et al (2015) Gravity-mode Period Spacings as a Seismic Diagnostic for a Sample of γ Doradus Stars from Kepler Space Photometry and High-resolution Ground-based Spectroscopy. *ApJS*218(2):27. <https://doi.org/10.1088/0067-0049/218/2/27>, [arXiv:1504.02119](https://arxiv.org/abs/1504.02119) [astro-ph.SR]
- Van Reeth T, Tkachenko A, Aerts C (2016) Interior rotation of a sample of γ Doradus stars from ensemble modelling of their gravity-mode period spacings. *A&A*593:A120. <https://doi.org/10.1051/0004-6361/201628616>, [arXiv:1607.00820](https://arxiv.org/abs/1607.00820) [astro-ph.SR]
- van Saders JL, Ceillier T, Metcalfe TS, et al (2016) Weakened magnetic braking as the origin of anomalously rapid rotation in old field stars. *Nature*529(7585):181–184. <https://doi.org/10.1038/nature16168>, [arXiv:1601.02631](https://arxiv.org/abs/1601.02631) [astro-ph.SR]
- Venturini J, Guilera OM, Haldemann J, et al (2020) The nature of the radius valley. Hints from formation and evolution models. *A&A*643:L1. <https://doi.org/10.1051/0004-6361/202039141>, [arXiv:2008.05513](https://arxiv.org/abs/2008.05513) [astro-ph.EP]
- Veras D, Brown DJA, Mustill AJ, et al (2015) Prospects for detecting decreasing exoplanet frequency with main-sequence age using PLATO. *MNRAS*453(1):67–72. <https://doi.org/10.1093/mnras/stv1615>, [arXiv:1507.04272](https://arxiv.org/abs/1507.04272) [astro-ph.EP]
- Verma K, Hanasoge S, Bhattacharya J, et al (2016) Asteroseismic determination of fundamental parameters of Sun-like stars using multilayered neural networks. *MNRAS*461(4):4206–4214. <https://doi.org/10.1093/mnras/stw1621>, [arXiv:1602.00902](https://arxiv.org/abs/1602.00902) [astro-ph.SR]

- Verner GA, Chaplin WJ, Basu S, et al (2011) Verification of the Kepler Input Catalog from Asteroseismology of Solar-type Stars. *ApJ*738:L28+. <https://doi.org/10.1088/2041-8205/738/2/L28>
- Wagner FW, Sohl F, Hussmann H, et al (2011) Interior structure models of solid exoplanets using material laws in the infinite pressure limit. *Icarus*214:366–376. <https://doi.org/10.1016/j.icarus.2011.05.027>
- Wagner FW, Tosi N, Sohl F, et al (2012) Rocky super-Earth interiors. Structure and internal dynamics of CoRoT-7b and Kepler-10b. *A&A*541:A103. <https://doi.org/10.1051/0004-6361/201118441>
- Walker G, Matthews J, Kuschnig R, et al (2003) The MOST Asteroseismology Mission: Ultraprecise Photometry from Space. *PASP*115:1023–1035. <https://doi.org/10.1086/377358>
- Wang HS, Liu F, Ireland TR, et al (2019) Enhanced constraints on the interior composition and structure of terrestrial exoplanets. *MNRAS*482(2):2222–2233. <https://doi.org/10.1093/mnras/sty2749>, [arXiv:1810.04615](https://arxiv.org/abs/1810.04615) [astro-ph.EP]
- Wang S, Ji J (2017) Near Mean-motion Resonances in the System Observed by Kepler: Affected by Mass Accretion and Type I Migration. *AJ*154(6):236. <https://doi.org/10.3847/1538-3881/aa9216>, [arXiv:1710.02638](https://arxiv.org/abs/1710.02638) [astro-ph.EP]
- Weiss LM, Isaacson HT, Marcy GW, et al (2018) The California-Kepler Survey. VI. Kepler Multis and Singles Have Similar Planet and Stellar Properties Indicating a Common Origin. *AJ*156(6):254. <https://doi.org/10.3847/1538-3881/aae70a>, [arXiv:1808.03010](https://arxiv.org/abs/1808.03010) [astro-ph.EP]
- White TR, Pope BJS, Antoci V, et al (2017) Beyond the Kepler/K2 bright limit: variability in the seven brightest members of the Pleiades. *MNRAS*471(3):2882–2901. <https://doi.org/10.1093/mnras/stx1050>, [arXiv:1708.07462](https://arxiv.org/abs/1708.07462) [astro-ph.SR]
- Wood MA, Still MD, Howell SB, et al (2011) V344 Lyrae: A Touchstone SU UMa Cataclysmic Variable in the Kepler Field. *ApJ*741(2):105. <https://doi.org/10.1088/0004-637X/741/2/105>, [arXiv:1108.3083](https://arxiv.org/abs/1108.3083) [astro-ph.SR]
- Wu Y, Murray NW, Ramsahai JM (2007) Hot Jupiters in Binary Star Systems. *ApJ*670(1):820–825. <https://doi.org/10.1086/521996>, [arXiv:0706.0732](https://arxiv.org/abs/0706.0732) [astro-ph]
- Zieba S, Kreidberg L, Ducrot E, et al (2023) No thick carbon dioxide atmosphere on the rocky exoplanet TRAPPIST-1 c. *Nature*620(7975):746–749. <https://doi.org/10.1038/s41586-023-06232-z>, [arXiv:2306.10150](https://arxiv.org/abs/2306.10150) [astro-ph.EP]
- Zinn JC, Pinsonneault MH, Huber D, et al (2019) Testing the Radius Scaling Relation with Gaia DR2 in the Kepler Field. *ApJ*885(2):166. <https://doi.org/10.3847/1538-4357/ab44a9>, [arXiv:1910.00719](https://arxiv.org/abs/1910.00719) [astro-ph.SR]